AN EXAMINATION OF CONFIGURATIONS FOR USING INFRARED TO MEASURE BOUNDARY LAYER TRANSITION

A Thesis

by

JUSTIN REED FREELS

Submitted to the Office of Graduate Studies of
Texas A&M University
in partial fulfillment of the requirements for the degree of

MASTER OF SCIENCE

August 2012

Major Subject: Aerospace Engineering

An Examination of Configurations for Using Infrared to Measure Boundary Layer Transition

AN EXAMINATION OF CONFIGURATIONS FOR USING INFRARED TO MEASURE BOUNDARY LAYER TRANSITION

A Thesis

by

JUSTIN REED FREELS

Submitted to the Office of Graduate Studies of
Texas A&M University
in partial fulfillment of the requirements for the degree of

MASTER OF SCIENCE

Approved by:

Chair of Committee,	Edward White
Committee Members,	Thomas Strganac
	Michael Pate
Head of Department,	Dimitris Lagoudas

August 2012

Major Subject: Aerospace Engineering

ABSTRACT

An Examination of Configurations for Using Infrared to Measure Boundary Layer Transition. (August 2012)

Justin Reed Freels, B.S., Texas A&M University

Chair of Advisory Committee: Dr. Edward White

Infrared transition location estimates can be fast and useful measurements in wind tunnel and flight tests. Because turbulent boundary layers have a much higher rate of convective heat transfer than laminar boundary layers, a difference in surface temperature can be observed between turbulent and laminar regions of an airfoil at a different temperature than the free stream air temperature. Various implementations of this technique are examined in a wind tunnel. These include using a heat lamp as an external source and circulating fluid inside of the airfoil. Furthermore, ABS plastic and aluminum airfoils are tested with and without coatings such as black paint and surface wraps. The results show that thermal conduction within the model and surface reflections are the driving issues in designing an IR system for detecting transition. Aluminum has a high thermal diffusivity so is a poor choice for this method. However, its performance can be improved using an insulating layer. Internal fluid circulation was far more successful than the heat lamp because it eliminates the reflected IR due to the heat lamp. However, using smooth surface wraps can mitigate reflection issues caused by the heat lamps by reducing the scatter within the reflection, producing an IR image with fewer contaminating reflections.

ACKNOWLEDGEMENTS

I would like to thank my committee chair, Dr. White, for encouraging me in my education and shepherding me through my academic years. It's been a privilege to learn from him and to work under his leadership.

Thanks also go to the department faculty and staff for their effort to create a great engineering program, to the staff at the Oran Nicks Low Speed Wind Tunnel for their support, to Dr. Saric and the people at the Flight Research Lab for lending the IR camera used in this experiment, and to Vestas for their funding and technical support. Thanks also to my family and friends for the love they have shown me.

Above all, thanks to my God and savior, Jesus Christ, through whom I am able to enjoy the learning of this world I live in, if only temporary. Without him I can do nothing.

NOMENCLATURE

AoA	Angle of attack
α	Absorptivity coefficient
Bi	Biot number
c_f	Friction coefficient
E_b	Blackbody radiation rate
$E_{b\lambda}$	Emissive Power
Fo	Fourier number
G	Irradiation
h	Heat transfer coefficient
IR	Infrared
J	Radiostiy
k	Thermal conductivity
λ	Wavelength
LSWT	Oran W. Nicks Low Speed Wind Tunnel
Nu_x	Nusselt number based on length x
ρ	Reflectivity coefficient
P	Absolute pixel value
Pr	Prandtl number
q_w	Heat transfer rate at wall
Re_c	Reynolds number based on chord length
RP	Rapid-prototyped

σ	Stefan-Boltzmann constant
T	Temperature
VG	Vortex Generator

TABLE OF CONTENTS

1. INTRODUCTION AND MOTIVATION

1.1 Airfoil Design and Testing

Wind tunnels are testing facilities used to examine many flow phenomena in a controlled and understood flow environment. Airfoils in particular have benefitted from these facilities, and different airfoil parameters have been tested ever since the first wind tunnel was constructed in 1871 (Rumerman 2003). Every new airfoil or new application of an airfoil brings new questions of its performance. With the development of computational fluid dynamic (CFD) simulations, many flow phenomena can be simulated and the performance of airfoils predicted. However, there is a need to validate CFD results against experimental data. Thus, the combination of data from CFD models with empirical data is crucial for airfoil design.

Airfoils are often tested for both global and local phenomena. The global phenomena include lift, drag and moment. These are what determine the general performance of the airfoil. The global phenomena are determined by what occurs locally, primarily the pressure distribution and shear forces. Because turbulent boundary layer flow produces substantially higher wall shear stresses than laminar flow, the location at which the boundary layer becomes turbulent, called the transition location, is a critical factor that affects the airfoil drag (Green 2008). Maintaining laminar flow was determined by Green to be the single most important factor in improving aircraft efficiency. However, predicting transition location is difficult for CFD simulations and is therefore of particular concern in validating their accuracy. If a simulation can accurately

---

This thesis follows the style of Experiments in Fluids.

predict the lift, drag, and moment as well as the correct pressure and shear stress distributions, including transition location, at the matching flow conditions, then the simulation is generally considered validated.

1.2 Current Methods of Measuring Transition Location at the LSWT

This thesis concerns transition measurement capabilities for wind tunnel tests and is motivated by previous work at the Oran W. Nicks Low Speed Wind Tunnel (LSWT) located at Texas A&M University. While this research is intended to aid the design of an IR system at the LSWT, the results are applicable to most testing facilities. The current method of measuring transition on an airfoil at the LSWT is to use an array of surface-mounted hotfilms. This requires adhering the sensors to the surface of the airfoil and routing wires to the anemometer on the outside of the tunnel as shown in Figure 1. These hotfilm sensors are made of nickel that has been deposited by an electron beam on a thin polyimide substrate with ½ mil thick copper leads extending from the sensor to the substrate edge. The hotfilm sensor is heated and maintained at a constant temperature while convection removes heat. The instantaneous voltage required to maintain the sensor at a constant temperature depends on the instantaneous shear stress and can thus reveal the laminar or turbulent shear stress across the hotfilm. Laminar and turbulent boundary layers have distinct frequency signatures that reveal the boundary layer state as shown Figure 2. Additionally, the mean voltages give relative shear stress values as shown in Figure 3, which also reveal areas of laminar and turbulent boundary layers.

This method of using surface-mounted hotfilms has several disadvantages. Hotfilm anemometry is an intrusive measurement technique. Though very thin, the hotfilms do not mount completely flush to the airfoil surface. This creates concerns that the boundary layer is influenced by the forward facing step of the hotfilm substrate and that the measured data from the sensors are therefore not completely accurate. Furthermore, the sensors require wiring to be routed along the airfoil surface to the tunnel wall, severely disrupting the flow downstream of the sensors. This prevents other data, such as wake profiles and surface pressures, from being accurately measured at the same time. To solve this, multiple tunnel runs have to be made for each configuration. The hotfilms also take about a day to install, setup and remove. The time intensive setup combined with the necessity to repeat runs result in an overall inefficient testing method.

1.3 Motivation and Objective

Measuring transition locations using IR has several advantages. Using IR allows transition location to be measured simultaneously with most other measurements. By consolidating tests into fewer runs, significant improvement in testing efficiency can be realized. IR also eliminates concerns of interference from intrusive instrumentation by remotely imaging the temperature profile of the surface. Furthermore, IR captures the global transition picture so any premature transition caused by contaminants or imperfections on the surface of the airfoil can be addressed while tests are in progress. Therefore, an IR system has the potential to improve both the data quality and the efficiency of wind tunnel tests. The main disadvantage of forgoing hotfilms is the loss of frequency data for the velocity fluctuations of the airflow at the surface. While there is valuable information in the frequency content, it is often a secondary concern to locating transition and is not necessary for validating CFD simulations that focuses on overall airfoil performance.

Some facilities have IR systems in place to measure transition, such as the wind tunnel facility at LM Glasfiber. Bæk (2008) examines several techniques for measuring transition on airfoils in the LM Glasfiber wind tunnel, including three heating methods for using an IR system: heat lamps, varying the tunnel air temperature, and internal heating cables. Similarly, an IR system is used to measure transition location during flight tests at Texas A&M Flight Research Lab (Carpenter 2009). The Texas A&M "SWIFT" airfoil model is constructed from aluminum, and the temperature difference is obtained by cold soaking the wing at 10,500 feet altitude and then diving down through warmer air. Transition location can be seen in the IR image as the wing warms. A third facility, located at Marche Polytechnic University in Italy, has also used IR to measure transition location. In this particular setup the airfoil surface is heated by an electric current running through a thin aluminum foil that coats the airfoil surface (Ricci, Montelpare, Artipoli, and Renzi 2008).

The objective of this thesis is to provide a database of responses from which to aid the design of future experiments that intend to measure transition using IR. The research presented here is far from exhaustive and there are many additional techniques that offer promising results. However, most all configurations are fundamentally represented by the configurations examined here. Both external and internal heating methods are tested with both thermally conductive and non-conductive models. Furthermore, various surface coatings examined. The configurations are evaluated based on the visibility of a laminar-to-turbulent temperature step in the IR image and the response to a change in transition location. A clear step decreases the uncertainty of the measurement and fast response times allow for quicker tests, particularly with runs involving a sweep through several of angles of attack.

2. THEORY OF MEASURING TRANSITION USING INFRARED THERMOGRAPHY

2.1 Convective Heat Transfer

Convection is the mechanism responsible for creating a measureable transition location and predominantly occurs within a thin boundary layer near the surface. The rate of convection is related to the skin friction generated by the velocity boundary layer as described by Reynolds analogy (White 1984). There are two primary classifications for velocity boundary layers, laminar and turbulent, and each has different flow characteristics and different rates of convection. Laminar boundary layers are characterized by smooth streamlines and lower shear stresses at the surface whereas turbulent boundary layers are characterized by chaotic fluid mixing and higher shear stresses at the wall. Laminar boundary layers, therefore, have a lower rate of convection than turbulent boundary layers.

Airflow over an airfoil typically begins laminar and transitions to turbulence at some point downstream. A diagram of transition is shown in Figure 4. By maintaining the surface of the airfoil at a different temperature than the air flowing over it, convective heat transfer will occur and the rate of convection will increase locally as the boundary layer becomes turbulent. This creates a temperature difference between the laminar and turbulent regions. If, for example, the airfoil is kept at a warmer temperature than the air flow and both laminar and turbulent boundary layers are present on the airfoil, the turbulent regions will cool faster than the laminar regions, producing regions of cooler surface temperatures. The boundary between the warmer and cooler regions represents the location of transition.

This theory can be described mathematically using a Blasius flow over a flat plate with a uniform wall heat flux. In this case the heat transfer is described using the Nusselt number as follows:

Nusselt number: $Nu_x = \frac{h\,x}{k}$

Laminar: $Nu_x = 0.453\ Re_x^{1/2} Pr^{1/3}$

Turbulent: $Nu_x = \frac{\left(c_f/2\right)^{1/2}\ Re_x Pr}{2.16 \ln\left[Re_x\left(c_f/2\right)^{1/2}\right] + 12.7 Pr^{2/3} - 13.8}$ where $c_f = \frac{0.455}{\ln(0.06\ Re_x)^2}$

In the above equations, h is the heat transfer coefficient, k is the thermal conductivity of the air, x is the distance along the surface, Pr is the Prandtl number, Re_x is the Reynolds number based on the length scale of x, and c_f is the friction coefficient. The equations are derived from the momentum integral equation and the energy integral equation using various approximations for the velocity and thermal boundary layer profiles (White 1984). A temperature distribution at the wall is found for both the laminar and turbulent cases using these Nusselt numbers and the equation below.

$$T_w(x) = T_\infty + \frac{q_w\,x}{kNu_x}$$

A comparison between the two temperature distributions shows that at a Reynolds number of 3×10^5 and a uniform 200 W/m^2 heat flux radiating into the surface, a temperature difference of 6.6°C exists at 30% chord. The results of this comparison are shown in Figure 5, and the method is used as a guide in estimating the magnitude of the laminar-to-turbulent temperature step expected to be seen during testing.

2.2 Infrared Thermography

All matter emits thermal radiation across a range of wavelengths. The range of wavelengths and the intensity of the radiation vary with temperature (White 1984). The total blackbody radiation across all emitted wavelengths is related to temperature as

$$E_b = \sigma T^4$$

where σ is the Stafan-Boltzmann constant. The emissive power is related to wavelength and temperature as

$$E_{b\lambda} = dE_b/d\lambda = \frac{C_1}{\lambda^5[\exp(C_2/\lambda T) - 1]}$$

where C_1 and C_2 are blackbody constants given in White (1984). As temperature is increased, the range of emitted wavelengths and the emissive power at each wavelength increases. IR cameras are designed to detect this radiation at particular wavelengths and produce a visible image that corresponds to the measured levels of infrared radiation.

While all objects radiate, they have different coefficients of absorptivity, reflectivity and transmissivity to infrared radiation. These three coefficients describe the response of a surface to irradiation and equal unity when summed together (White 1984). Assuming the object to be opaque, and therefore zero transmissivity, the relation reduces to $\alpha + \rho = 1$, where α and ρ are the absorptivity and reflectivity coefficients respectively. The less reflective an object is the more energy the object absorbs and therefore the warmer the object will be at thermal equilibrium. The total energy radiating from the surface is a combination of the emitted and reflected radiation.

$$J = \varepsilon E_b + \rho G$$

In the above equation, J is the radiosity, ε is the emissivity coefficient and G is the irradiation. In order to collect information about an object's temperature using an IR camera, the measured IR radiation should be emitted from the object and not reflected from another source. Therefore the object's IR reflectivity should be minimized in order to both maximize its absorptivity and increase the meaningful content of the IR image.

It is also important to realize that the emissivity, absorptivity and reflectivity of an object vary with direction. Therefore the behavior of the irradiation on the surface, how much is reflected or absorbed, depend on the angle that it strikes the surface with and the directional characteristics of the surface. Because the emissivity, in addition to the reflectivity, varies with direction, the IR intensity, J, measured by the IR camera will also depend on the direction.

3. DESIGN CONSIDERATIONS

3.1 Reynolds Number & Heat Flux

For an IR system to successfully measure transition, a temperature step must be visible within the IR image. According to the theoretical flat plate example presented in the previous chapter, the only factors affecting the temperature step are Reynolds number, heat flux, and the location where the boundary layer transitions. While this neglects many other factors, it shows that increasing the Reynolds number causes an increase in the Nusselt numbers for both laminar and turbulent boundary layers. However, the laminar Nusselt number increases at a different rate than the turbulent, causing a decrease in the magnitude of the temperature step. Therefore, at higher Reynolds numbers, a larger heat flux into the surface is required to maintain the same temperature difference between laminar and turbulent regions.

3.2 Reflectivity

In order for the airfoil to have a discernible temperature step associated with transition, it must have a low reflectivity factor. The IR image of a reflective model contains a high percentage of stray IR radiation from the surrounding objects. However, there is no completely non-reflective surface and intense IR sources, particularly the heat lamps, can still significantly distort the IR image. Therefore it is important to design for the reflections and position the heat sources so that the expected reflections leave the IR image minimally distorted.

Using external heat sources such as heat lamps to heat the airfoil require that the radiating heat be absorbed by the airfoil. The more reflective an object is, the less energy it will absorb. It would therefore be difficult to warm a reflective object using radiating heat. For heat lamps to work, the airfoil must have a low reflectivity in order to absorb the energy required to create a warm body necessary for convection.

In most cases surface roughness reduces the reflectivity of the surface. Surface roughness is also a major concern in wind tunnel testing as rough surfaces often cause premature transition. For model quality, it is usually desirable to have an airfoil as smooth as possible. When fabricating airfoils from aluminum, this means that a polished metallic surface is often specified. This, however, is highly reflective to IR and a poor choice for using IR. Coating the surface in some material could drastically change the reflectivity of the airfoil at a potential increase in surface roughness. It is important to consider the roughness of the model surface when evaluating configurations for using an IR system.

3.3 Thermal Diffusivity

As a temperature step begins to develop on the airfoil surface, heat will flow from the warm to the cool regions across the temperature step and diminish the magnitude and gradient of the temperature step. Conductive materials will reduce the temperature step more than insulating materials and therefore have a higher uncertainty of the measured transition location. ABS plastic has a thermal conductivity that is two orders of magnitude less than aluminum, making it preferable to aluminum in terms of maintaining a temperature step.

The ability of an object to maintain a temperature step can also be described by the non-dimensional Biot number. This number is defined as the ratio of the convection heat transfer coefficient, h, to the object's conduction coefficient, k, times a characteristic length (White 1984).

$$Bi = \frac{h}{k} L$$

A low Biot number signifies a high conduction rate within the body as compared to the convection rate such that the temperature within the body is nearly uniform. A high Biot number signifies a high convection rate compared to the internal conduction rates, creating internal temperature gradients. A high Biot number is necessary for creating the temperature step required to measure transition using IR.

A conductive material will, however, spread heat well, creating a more uniform temperature distribution. This is particularly important for heating or cooling the model from the inside where the heat must travel between the center of the model and the surface. Ideally, the inside will be a very conductive material to create a uniform heating or cooling of the model, and the surface would be a non-conductive material to maintain the temperature profile created by the local convection rates.

Coating the aluminum with an insulator will improve the sharpness of the temperature step. The effect on the temperature step from changing insulation thicknesses on an aluminum model was numerically investigated by Bæk (2008). Generally, the thicker the insulation, the sharper the temperature gradient is at the step. This work was done for a hollow aluminum model whereas the model used for this research is solid. The test models are discussed in detail in a later section.

Even with an insulation layer coating the aluminum, conductive heat transfer into the aluminum can be detrimental to the temperature profile of the surface. This is especially true if the heat source is external and the aluminum model is nominally cold. Any heat entering the surface of the airfoil would tend to conduct throughout the cold airfoil preventing enough heat from remaining at the surface to create a measurable temperature step. This would require that the entire airfoil model be brought up to some nominally warm temperature to reduce the rate at which heat is conducted away from the insulating surface. However, as the entire airfoil warms it is continually cooled by means of convection on all surfaces of the airfoil, including those not being directly warmed by the heat lamps. The heat lamps need to provide enough energy to the airfoil to overcome all heat losses while maintaining a high enough level of convective heat loss on the surface of interest to create a measurable temperature step where the boundary layer transitions.

3.4 Response Time

In order for an IR system to be a worthwhile improvement, it must operate in conjunction with other devices as part of a standard test run. This often includes a sweep through several angles of attack, in which data is collected at each angle. Consequently, an IR system must be able to measure the transition location for any reasonable angle and quickly respond to a new transition location as the angle of attack changes. This requires that the temperature profile of the surface respond rapidly to the changes in convection as the boundary layer transition location changes. If the response time is too slow, the run time for a typical angle of attack sweep, which includes about 50 angles, would be so long as to make the IR system undesirable. The LSWT currently spends only a few seconds at each angle for a typical angle of attack sweep. Ideally the IR system would respond within this time, though minor increases in this time are acceptable for the sake of the added data.

A primary factor affecting response times is the energy available to change the temperature to the new equilibrium state. This energy is dependent upon the energy supplied at the source and the percentage that reaches the surface of concern. For external heating, this accounts for the wattage of the heat lamp, the fraction of that wattage that radiates towards the model surface, the amount absorbed by the surface and the percentage of the heat in the surface that is convectively transferred to the airflow. For internal water circulation, the factors are the flow rate, the temperature of the water, and the percentage of heat that conducts through the model to the surface of interest.

The response of the system can be understood using the non-dimensional Fourier number along with the previously discussed Biot number. The Fourier number is a non-dimensional representation of time in transient heat transfer problems and relates the rate of heat conduction to the rate of thermal energy storage. Fourier number is defined below.

$$Fo = \frac{kt}{\rho c_p L^2}$$

In this equation, k is the thermal conductivity of the object, t is the characteristic time, ρ is the density of the material, c_p is the specific heat capacity, and L is the characteristic length. Multiplying the Fourier number with the Biot number gives a ratio of the heat convection rate to the thermal inertia. For a quick response, this number should be small.

The external source of heating has an advantage in that heat ideally enters at the surface by radiation absorption and then exits on the same surface by convection. There is little mass that must change temperature, resulting in a quick response time. In reality, there is conduction away from the surface, and this mass must also change temperature to achieve equilibrium.

Internally heating the model has an advantage in that there are no losses due to heat conducting away from the surface. Rather, heat conducts through the model from the warm center toward the cool surface, and virtually all of the heat that reaches the surface must be convectively transferred to the airflow. However, this requires a large mass to respond and therefore reduces the response time. Because this mass must be thermally conductive and therefore dissipate heat quickly, response times may nevertheless be adequate.

3.5 Application to Facility

The IR system is intended as an improvement to wind tunnel testing capabilities and is motivated by recent airfoil testing at the LSWT. While there are expressed interests for an IR system at the LSWT, this research is applicable to any wind tunnel facility. In fact, the research was performed using a different wind tunnel. In any case, the IR system must be designed specific to the facility to account for the accessibility, size, and testing conditions.

There are two airfoil models that have been recently tested at the LSWT and are used as guides in designing models for this research. One is constructed of three pieces of solid, machined aluminum bolted together and finished with Bondo® body filler along the seams. The other is constructed with aluminum leading edge and trailing edge pieces and a main body made of several ABS plastic parts, which were built using a rapid prototyping machine. These parts were all bolted to an internal frame and, with the exception of the leading edge piece, were sanded and painted, using Bondo® body filler along the seams. Future airfoil models at the LSWT are expected to resemble these in both material and machining complexity.

4. TEST MODELS

4.1 Airfoil Selection

A NACA 0018 airfoil was selected for this study as it most closely represents typical airfoils tested at the LSWT. The two most recent airfoils tested at the LSWT were both 18 percent thick, and it is expected that many of the future airfoils will be a similar thickness. A symmetric airfoil was chosen because it is simpler to design and manufacture than cambered airfoils.

The chord length for both test models is 12 inches. The span for the aluminum model is 24 inches, while the span for the RP model is 32 inches. The span for the RP model is larger because it uses a previously designed and manufactured plastic surface.

4.2 Solid Aluminum Test Model

The solid aluminum test model was manufactured using a CNC mill. The model was manufactured in two halves and secured together with eight bolts and four alignment pins. The bolts were fastened from the bottom side of the model into tapped holes in test side of the model to avoid having to fill holes on the test surface of the model. Bondo® body filler was used on the seam at the leading edge and sanded smooth with 600-grit sandpaper. Six copper pipes in the spanwise direction were equally spaced along the chord line, beginning from 10.5% chord and going to 60%, and extended 2 inches on both sides of the aluminum model. A thin layer of conductive grease was applied between the copper pipe and the aluminum to fill any gaps. This created a better interface for heat transfer than if left with air between the aluminum and copper. Finally, two endplates were secured to the ends of the model to encourage 2-D flow over the wing. Drawings for the aluminum model are shown in Figures 6 through 9.

The span of the aluminum test model was 24 inches. This length was just long enough to prevent the end plates from casting a significant shadow on the model surface when the heat lamp is turned on. A small shadow was cast on the surface but not large enough to disturb the data near the viewing area of the camera. Because the model was solid aluminum, keeping the span short helped reduce the weight.

4.3 RP Plastic Test Model

The plastic test model was constructed with white ABS plastic using a rapid-prototyping machine. It was constructed in four spanwise sections, each containing a top and bottom part. The seams between the top and bottom pieces were located on the bottom side of the model, with the furthest upstream seam at 3% chord. The seam between the two middle spanwise sections was located inside the camera viewing area. All spanwise sections were aligned using pins and were secured to an inner aluminum frame by bolts through the upper surface of the plastic. This held the plastic securely to the aluminum and, combined with a layer of grease between both surfaces, ensured a proper transfer of heat. None of these bolts were in the camera viewing area. These bolts were covered with a layer of Bondo® and sanded smooth. The grease, however, had a tendency of seeping through the seams between the plastic pieces.

The aluminum frame contained six copper pipes extending the length of the span plus two inches on either side. These were located 0.6 inches from the surface and placed at the same chordwise locations as the copper pipes on the solid aluminum model.

The aluminum frame was used to structurally support the model as well as provide a good conductor to evenly heat or cool the wing from inside the model. The aluminum frame only contacted the top test surface of the wing, leaving much of the inside of the RP wing as empty space. End plates were bolted to the ends of the aluminum frame to encourage 2-D flow over the wing. Drawings of the RP model are shown in Figure 10 through Figure 13.

The RP plastic was ¼ inch thick in most places other than near the leading edge. It was not, however, solid plastic throughout the thickness but contained a sparse cross-hatching pattern of plastic inside each RP part with pockets of air in between as shown in Figure 14. This was a setting on the RP machine that maintains structural support while saving material. The RP machine builds each part layer by layer from the ground up and has a higher resolution in the plane parallel with the base surface. Each part was oriented in the machine with the span in the vertical direction, creating a wing with the most accurate profile shape possible from the machine. It also creates small, consistent chordwise ridges between each layer. This can be seen in the data from the profilometer shown in Figure 15.

5. TEST SETUP

5.1 Wind Tunnel Facility

The experimental tests were performed in the 3’x4’ wind tunnel located in the Fluids Laboratory in the Department of Aerospace Engineering at Texas A&M University. It is a closed circuit wind tunnel with airspeed controlled by variable pitch fan blades and temperature maintained at 13° ±0.5°C.

The test section is three feet tall and four feet wide and equipped with a pitching mechanism located on a strut in the center of the test section as shown in Figure 16. It pivots about an axis that is 13¼ inches from the test section floor and has a 5⅝ inch long arm extending from this axis up to the mounting plate near the center of the cross-sectional area of the test section. The bottom side of the model mounts on top of this plate.

A stepper motor operates the pitching mechanism and requires calibration to set the angle of attack. The mechanism was found to have some play in the linkages that affected the angle of attack of the model. This mattered most as the model rotated from negative to positive angles and the center of gravity of the model crossed the pivot point. This caused the load in the linkages to switch from tension to compression, and an error of nearly 1 degree in angle of attack resulted. However, exact angles were not of critical importance because the objective was not to collect transition data on the airfoil but to determine how to best use IR. Good repeatability was necessary in order to directly compare IR images. The stepper motor required recalibration periodically to ensure repeatability.

The test section is constructed from acrylic, which is highly reflective to IR radiation. To reduce the intensity of stray IR radiation within the test section, the ceiling was coated with black paper. Furthermore, both the camera and heat lamp required holes to be cut in the test section wall in order to optically access the model. The IR camera and the heat lamp are mounted on top of the test section and directed downward at the top of the model. A 2.5 inch diameter hole was cut in the acrylic for the camera and was located 2.3 inches off-center to accommodate a pre-existing, ⅝ inch wide slit in the center of the ceiling for a streamwise traversing mechanism. Another hole, 5 ¼ inches in diameter, was cut for the heat lamp 15.6 inches from the center. To reduce the heat absorbed by the acrylic, the lamp was mounted so that it protruded about ½ inch into the test section. The gap around the holes was not sealed as the test section is already vented to the room by design. The ceiling of the test section is shown in Figure 17.

5.2 External Heat Lamps

A single 375 watt IR heating lamp was used to heat the test model located near the middle of a 3’x4’ test section, approximately 16 inches away from the heat lamp. The lamp was mounted 13¼ inches to the side of the camera. Assuming the model surface is perfectly smooth, this puts the expected reflection of the heat lamp outside of the camera’s field of view. This also produced a radiant power distribution on the surface of the model within the viewing area of the camera that is roughly equivalent to the design of an existing configuration of heat lamps at the LSWT. This earlier design incorporated 10 heat lamps, each at 375 watts, and was calculated to generate just over 100 W/m^2 within the viewing area of the camera at just under 5 feet away from the lamps. The power distribution and expected heat lamp reflections are shown in Figure 18. All calculated wattage distributions assume the model to be a flat surface at zero angle of attack and that 57% of the rated wattage is radiated from the heat lamp in a uniform hemispherical distribution. The heat lamp efficiency is taken from the posted efficiency of a similar heat lamp rated at 250 watts (Office of Energy Efficiency 2009).

5.3 Internal Water Circulation

Water was pumped through the test models to provide an internal source of temperature control. Ice water was originally used because it could be controlled by simply maintaining ice in the water reservoir. This creates a cold model in a warm airflow, thus convection heating, not cooling, is the driving mechanism. A submersible pump was used to circulate the ice water at 0.66 gallons per minute through ¼ inch ID tubing as shown in Figure 19. The ice water was later changed to tap water when condensation became an issue on the aluminum model surface. Because the tunnel temperature is controlled and kept around 13°C, the tap water, at 23°C, provided an internal heat source. The warm water was routed directly from the faucet tap at an average flow rate of 0.63 gallons per minute. This changed slightly for each test, varying ±0.16 gallons per minute.

The inlet line to the model was split into two; one inlet line was connected to the furthest upstream copper pipe on the model while the other was connected to the furthest downstream. The return lines were also connected to both ends of the model. This created two, overlapping, internal paths through the model as shown in Figure 20 with water in one path flowing in opposite direction from the other to ensure a uniform heating or cooling of the model.

5.4 Infrared Camera

The IR camera used for this experiment was a Merlin Mid IR camera from FLIR Systems. It uses an Indium Antimonide detector on a 320x256 focal plane array, and is internally cooled to 77 Kelvin. The camera can detect IR radiation with wavelengths between 3 and 5 μm and measure temperature differences of 0.025 °C. It was equipped with a 25mm lens, producing a field-of-view (FOV) of 22°x16°. The camera was oriented so that the 22° FOV dimension would be aligned with the chord dimension of the test model in order to capture as much of the chord length as possible.

Absolute pixel values are assigned to each pixel in the IR image produced by the camera. These values, ranging from 0 to 4095 for a 12 bit image, represent the measured intensities of IR radiation and can be calibrated to a temperature. While it is useful for this setup to calibrate the camera in order to understand the process in physical units, a calibration is not necessary to identify transition. A change in surface temperature associated with transition is all that is needed from the IR image, not absolute temperature values. Once the image is captured, these pixel values can be mapped with various colors or grayscales, and the scale of this mapping can be adjusted to fit the range of values in the image. However, the values themselves do not change.

The camera was connected directly to a desktop computer and operated using software that was provided with the camera. This software displayed live images from the camera and could record images at various frame rates. The video files were exported as 12-bit tiff files for post-processing in MATLAB.

A temperature calibration was applied to the images during post-processing to understand the results in physical units. The calibration data was taken by cold soaking a steel plate with a surface thermocouple adhered to the surface in a freezer. The plate was removed from the freezer and placed in front of the camera with the lens close to the location of the thermocouple, similar to that shown in Figure 21. An IR image was captured and the associated temperature was recorded. The plate was allowed to warm up and images were taken as the plate approached room temperature, each time the plate temperature was recorded. Then the camera was aimed at a black acrylic surface that was heated with a heat gun for several minutes and again had a thermocouple adhered to the surface. The process of capturing images and recording the associated temperature was repeated as the surface cooled down to room temperature. The average pixel value of each image was equated to the measured temperature, and the data was fit to a fourth-order polynomial.

5.5 Thermocouples

Because the local convection rate is dependent on the temperature differential between the surface and the air, it is important to measure the air temperature in order to base comparisons. Similarly, the temperature of the model is driven by the internal water temperature and therefore is also measured. Additionally, the temperature of the model surface was measured in order to provide a second means of measuring transition to support the results of the IR images. Altogether there were five thermocouples that collected temperature data during the experiment. A J-type thermocouple was installed upstream of the test model to measure the tunnel air temperature. Two K-type thermocouples were installed on the test model, one at 25% chord and the other at 60% chord and positioned at different span locations to keep the upstream thermocouple from interfering with the downstream one. Each of these thermocouples was built into a self-adhesive pad for adhering to surfaces as shown in Figure 22. The last two were T-type thermocouples and were installed as shown in Figure 23 into the inlet and exit water lines used to internally control the model temperature.

All thermocouples were connected to a thermocouple DAQ module. The thermocouple for measuring the temperature of the tunnel air was connected to its own thermocouple DAQ module while the four others were connected to a separate 4-channel thermocouple module. These modules were equipped with their own cold junction compensation to produce a temperature from the measured voltage.

5.6 Pitot Tube

The tunnel is equipped with a Pitot-static tube just upstream of the model. This sensor collects both total and static pressure and is connected to a Barocel® pressure sensor, which measures the difference between the two. This difference is the dynamic pressure of the airflow and is used to calculate tunnel airspeed.

6. TEST CONFIGURATIONS AND CONDITIONS

Two forms of temperature control were tested: external heat lamps and internal water circulation. Both were tested for every test model configuration. The water circulated through the model was initially ice water but was later changed to tap water when condensation on the model surface became an issue. There were two separate models: solid aluminum and ABS plastic with an aluminum core. Each of these models was tested with various surface treatments. With the exception of the polished aluminum, all configurations were tested with a trip strip located at 30% chord and covering a short length of the span. This ensured a known turbulent region within the IR image and was used to compare the natural transition location. All configurations were tested at a Re_c of 6.6×10^5. The painted RP model, discussed later, was also run at a Re_c of 2.2×10^5 and 4.4×10^5 to observe the effect of Reynolds number. Configurations and test conditions are listed in Tables 1 – 3.

6.1 Solid Aluminum Model Configurations

For the first configuration, the test surface of the aluminum model was polished. The entire model was wet-sanded with 600-grit sandpaper and then finished with fine steel wool to a near mirror finish. The installed model is shown in Figure 24. The average roughness of the surface was measured to be 0.43 μm. This measurement was performed using a profilometer at multiple chord and span locations and in both the chord and span directions within the camera field of view. The smooth metallic finish represents the most preferred finish for aerodynamic testing because the smooth surface delays transition.

The painted aluminum model was made by rough sanding the polished model with 100-grit sandpaper to allow good paint adhesion. The model was then painted with 5 coats of flat black spray paint and wet-sanded with 400-grit sandpaper. This achieved an average roughness of 0.67 μm and added a thickness of approximately 50 μm. Figure 25 shows the painted aluminum model after a run involving ice water circulation. Because of the humid air, condensation can be seen on the cold surface.

A transparent layer of self-adhesive plastic wrap was applied to the painted aluminum surface. Care was taken to avoid air bubbles getting trapped under the wrap as the wrap was applied to the surface. These air pockets might trip the boundary layer and cause premature transition. They would also cause the surface wrap to be locally insulated from the aluminum model by the trapped air and consequently have a different temperature. The wrap did not cover the entire bottom surface of the model or the entire span, only a section on the test surface just larger than the viewing area of the camera. The wrap added about 75 μm of thickness and had an average surface roughness of 0.13 μm. The model was also tested with the wrap painted flat black. The paint on the wrap was wet-sanded with 400-grit sandpaper, which produced an average roughness of 0.48 μm. Pictures of the clear and painted wrap configurations can be seen in Figure 26 and Figure 27 respectively.

The aluminum was also examined with a layer of glossy black Monokote®, which had a thickness of about 50 μm and an average roughness of 0.09 μm. Monokote®, shown installed on the model in Figure 28, is often used to coat wings on model airplanes and adheres to surfaces by applying heat. However, it was difficult to adhere to the painted aluminum and air pockets were prevalent. These air pockets caused the associated regions of Monokote® to be insulated from the highly conductive aluminum and were therefore a different temperature in the IR image as seen in Figures 51 and 56. It is probable that the aluminum would diffuse the heat from the hot iron used in applying the Monokote®, preventing enough heat from accumulating to activate the adhesive.

Finally the aluminum was tested with a layer of painted Bondo®, shown in Figure 29. The plastic wrap was removed and two strips of masking tape were applied to the model from leading edge to trailing edge, each at a different span location. The camera viewing area was within the area marked off by the two strips of tape. Bondo® body filler was mixed and applied between the two strips of tape. It was then block-sanded down to approximately the thickness of the masking tape, which was measured to be 130 μm. The tape was removed, and five coats of flat black spray paint were applied to the Bondo®. This was then wet-sanded using 400-grit sandpaper, producing an average surface roughness of 0.61 μm.

6.2 RP Plastic Model Configurations

The plastic parts for the RP model were initially assembled with minimal surface finishing. The bolt heads in the test surface were filled with Bondo® and sanded smooth to prevent influences on the region within the camera viewing area. The layer-by-layer manufacturing method of the rapid prototyping machine produced RP parts with noticeable ridges running streamwise along the surfaces. This is seen in the spanwise profilometer data shown in Figure 15, which measured an average roughness of 17 μm.

However, the average roughness in the chordwise direction was only 0.58 µm. These RP parts were assembled together to form the as-built configuration.

The plastic surface was then sanded smooth, eliminating much of the streamwise ridges. However, there was a noticeable reduction of the glossy finish. This configuration, shown in Figure 31, was tested before painting to determine how merely sanding the surface changes the results. The average roughness was 2.1 µm for a chordwise sample and 5.1 µm for a spanwise sample. The model was then painted flat black and wet-sanded with 400-grit sandpaper, achieving an average surface roughness of 0.68 µm. This was tested as the third RP plastic configuration and can be seen in Figure 32.

The painted RP plastic model was then coated with Bondo® in the same way as the aluminum model. Two strips of masking tape were applied from leading edge to trailing edge at different span locations. A layer of Bondo® was applied between the two pieces of tape, covering the camera viewing area of the model. The Bondo® was sanded down to approximately the thickness of the masking tape, which was measured to be 130 µm, and then painted with five coats of flat black spray paint. A strip of the Bondo® surface was left unpainted to examine any differences between painted and unpainted Bondo®, and the entire surface was finished by wet sanding with 400-grit sandpaper. The average roughness for the painted regions was 0.35 µm whereas the average roughness of the unpainted Bondo® was 4.3 µm. Because of the added thickness of the paint, there were two streamwise steps between the painted and unpainted regions. Care was taken to blend this step near the leading edge where the boundary layer is more sensitive to such disturbances. This configuration is shown in Figure 33.

The fifth and final configuration for the RP plastic model examined covering the wing with Monokote®, which had an average roughness of 0.09 µm. The layer of Bondo® was left on the surface and simply covered over with a layer of Monokote® as shown in Figure 34. The two streamwise ridges that resulted from the added thickness of the paint were also left in place. Covering these ridges with Monokote® provided a realistic application of the coating as its primary function would be to cover over model imperfections.

6.3 Vortex Generator Configurations

Vortex generators (VGs) were tested on the aluminum model coated with the painted adhesive wrap. They were constructed in pairs from 0.011” thick aluminum sheet with the corners folded up. Two configurations were tested: one large VG, shown in Figure 35 and an array of 3 smaller VGs as shown in Figure 36. Both VG configurations were located with the front of the VGs at 20% chord. The large VG had a streamwise width of 1.18 inches, a maximum spanwise width of 2 inches, and an angle of 24° from the streamwise direction. The smaller VGs had a streamwise width of 0.51 inches, a maximum spanwise width of 1.02 inches, an angle of 34° from the streamwise direction, and were separated by 1.35 inches between pairs.

6.4 Testing Procedures

Before testing began, the stepper motor for the pitching mechanism was calibrated. This was recalibrated every few days to ensure repeatability. All water circulation lines were connected and chord markers were adhered to the surface. The chord markers were made from aluminum tape cut into triangles and were placed on the surface every 10% chord. A different shaped marker was used at 50% chord to identify it and all subsequent markers in the IR image. Not all markers were visible in the IR image at the same time, but the 50% chord marker was always visible. The surface thermocouples were installed at 25% and 60% chord.

For each heating method, the model was allowed to soak for approximately 10 minutes to achieve a uniform temperature. The tunnel was then turned on and adjusted to the correct airspeed. Another several minutes were given to allow the tunnel air temperature to drop to normal operating temperatures. This time also allowed the model temperature to adjust to its new equilibrium.

At the beginning of every angle of attack sweep, the model was brought down to -10° and then back up to -8°. The model would then be pitched up through the angle of attack sweep. Going past -8° and then back up ensured that the load within the gearing was consistently in the same direction throughout the sweep.

The angle of attack was set by a stepper motor and controlled using Labview. This program also recorded tunnel airspeed, tunnel air temperature, model surface temperatures, and water circulation temperatures. All data fields were collected at 10 kHz for 1 second and averaged together to make a single data point every second for each field.

IR images were collected every 10 seconds for tests involving a sweep through angles of attack and every ½ second for tests recording transient responses. For angle of attack sweeps, each angle was held for at least 1 minute before moving to the next angle. Every configuration was tested with a sweep from -8° to at least 12° in increments of at the most 2°. Some sweeps were tested in 1° increments. For transient tests, the model was held at -4° angle of attack for at least 10 minutes to ensure equilibrium and then rotated to 0° angle of attack. Data was collected until the surface temperature appeared to reach equilibrium.

Temperature, airspeed and angle of attack data were recorded on a separate computer than the computer used to collect IR images. Consequently, the images were not perfectly synchronized with the collected data. However, because each angle was held for a minimum of 1 minute, it was not necessary to have the data be exactly matched with an image. For angle of attack sweeps, the last image recorded for each angle is taken as the most accurate because it has had the most time to reach equilibrium. The last 10 seconds of data for the corresponding angle are then matched with this image.

7. RESULTS AND DISCUSSION

7.1 Data Analysis

IR images were analyzed in MATLAB using the image processing toolbox. In each IR image the flow is from left to right, and the chord markers seen in the image were used to map the pixel locations in the IR image to the chord location of the model. Every 10% chord was marked on the model and was visible in the IR image. Linear interpolation provided chord locations between chord markers.

Pixel values were extracted for each image of interest, and two streamwise temperature profiles were created from these values: one profile that included the turbulent region caused by the trip strip; the other was outside the influence of the trip strip. This is done for every configuration but can be clearly seen in Figure 97. The profile plotted in red is the turbulent region caused by the trip strip at 30% chord. This profile is found by averaging several streamwise profiles taken from the upper white box shown on the IR image in Figure 96. The profiles from the lower white box in the same image were averaged together to form the profile plotted in black in Figure 97. The camera calibration was applied to the profiles to get a temperature distribution from the pixel values.

Because convective heating, not cooling, was the driving mechanism for configurations using ice water, the temperature profile was opposite of every other configuration in which the model is heated instead of cooled. To better compare profiles at a glance, the temperature axis of ice water configurations are reversed as seen in Figure 97.

The temperature profile was calculated as a fraction of the difference between a characteristic hot and cold temperature. This is shown on the right vertical axis as demonstrated in Figure 97. For tap water circulation, the water and tunnel air temperature were used as the characteristic hot and cold temperatures respectively. This was reversed for ice water circulation so that the tunnel and the water temperature were the hot and cold temperatures respectively. For the heat lamp, the characteristic hot temperature was the equilibrium black body temperature. This assumes the heat lamp operates at 57% efficiency and projects in a hemispherical pattern. The calculated temperature varied with tunnel temperature but was typically around 34°C. This was found for the infinitesimal area of the model closest to the heat lamp. The tunnel temperature was used as the characteristic cold temperature.

Temperature profiles were also extracted from the IR images that captured the transient response. For each run a point was tracked through the series of profiles as the surface temperature adjusted to a new equilibrium location. An example of this is shown in Figure 98. The tracking point is marked by a yellow dot and was located in the region that began as laminar and became turbulent once the model was pitched. Various profiles are plotted at different stages of the response. Furthermore, the response of the tracking point is plotted as a fraction of the difference between the initial and final pixel value as demonstrated in Figure 99. This response is fit to an exponential decay function. The fit was limited to the data that was collected after the model finished pitching though often a significant response had already taken place while the model was pitching. The start and end times of the when the model was pitching are shown as vertical black lines on the plot and a green dot is shown where the section of data used to fit the exponential decay function begins.

Each tested configuration contains a sequence of figures listed in the FIGURES section. The sequence begins with the IR image for the configuration with flow from left to right at 0° angle of attack. The image contains two boxes that correspond to the temperature profiles plotted directly below the IR image. The third figure in the sequence is the thermocouple temperature measurements from the angle-of-attack sweep. This includes the two surface thermocouple measurements and the tunnel air measurements. This is typically followed by a plot of temperature profiles showing the evolution of the temperature distribution at different stages in the transient response. These profiles show the point that is used for plotting the response in the final figure of the sequence.

7.2 Polished Solid Aluminum

The polished solid aluminum appeared very reflective to IR radiation such that the reflections of the heat lamp were the dominant source of measured IR in the image as shown in Figure 37. Even with internal water circulation and no heat lamp, the reflectivity of the surface was enough that the camera’s own reflection could be seen as shown in Figure 40. With such a high reflectivity, the emitted IR from the model was undetectable amongst the reflected IR. Consequently, no useful data could be extracted from the IR image. Figures 38 and 41 show the extracted temperature profiles. As a reference, a successful transition measurement would produce a temperature profile that closely resembled the ideal case shown in Figure 5.

It was possible the directional variations in absorptivity and emissivity of the model surface may have caused some of the variations otherwise attributed to reflections. Because the surface was curved and the light was emitted radially from the heat lamp, the light struck the different regions of the surface at different angles, and absorption of the energy would likely have varied with this angle. Similarly, the emitted IR radiation varied with direction, and the IR camera only measured the intensity of IR that was emitted or reflected from the surface in the direction of the camera lens. However, because the tunnel ceiling and the camera lens itself could be distinctly seen in the IR image, Figure 40, reflectivity was certainly the primary issue and not variations in emissivity. Variations in absorptivity and emissivity coupled together could have contributed to the inability to use IR on the polished aluminum with the heat lamp. The significance of this would likely be small considering that local energy variations caused by absorptivity variations would diffuse throughout the model. A sequence of IR images taken from an angle of attack sweep with no airflow is shown in Figure 158 without the heat lamp and in Figure 159 with the heat lamp. This shows the results of directional variations without the variations caused by differences in forced convection rates.

Each thermocouple, however, measured an abrupt temperature change as the model was swept through angles of attack. This can be seen in the time history for the surface thermocouple measurements shown Figure 39 for the heat lamp and Figure 42 for ice water circulation. The location of this temperature shift appeared to move upstream with increased angle of attack. The shift was measured first at 60% chord for 0° angle of attack and then at 25% chord when rotated to 8° angle of attack. The angles and locations at which these changes occurred were reasonable for transition, and in both the heat lamp and the ice water circulation the temperature shifted closer to the tunnel air temperature, implying an increase in convection rate. This was expected as the transition of the boundary layer to turbulence should increase the convection rate. This supports the existence of a transition-induced temperature step even though it cannot be seen in the IR image.

7.3 Painted Aluminum

The painted aluminum model, shown in Figure 43, was much less reflective than the polished aluminum shown in Figure 37. This is evidenced by the intensity of the reflections shown in the temperature profiles for the painted aluminum and the polished, Figures 44 and 38 respectively. Despite the reduced reflections, the IR images contained no temperature step signifying transition. The IR image and associated temperature profiles are shown for the heat lamp in Figures 43 and 44 and the internal water circulation in Figures 46 and 47. Instead of a temperature step, the temperature profile from using tap water, Figure 47, showed a only a decrease in temperature from the leading edge to the trailing edge. This implies the thermal conductivity of the aluminum is too high to maintain a sharp gradient. Instead, the temperature distribution was a gradual gradient from the predominantly warm laminar regions to the cool turbulent regions across the chord length of the model. The IR images taken while using the heat lamp show an increase in temperature from the leading edge to about 30% chord and then a decrease to the trailing edge, shown in Figure 44. This initial increase in temperature was likely caused by both the distribution of heat from the heat lamp, as shown in Figure 18, and by reflections. Boundary layer growth might also have been a contributor as shown in the example of an ideal temperature distribution in Figure 5. However, this increase in temperature was not seen for the tap water in Figure 46 and must therefore be unique to using the heat lamp. The distribution of heat from the lamp also caused spanwise variations in temperature with regions nearer the heat lamp being warmer. The black profile in Figure 44 was warmer because it was taken from the bottom of the IR image, a region that is closer to the heat lamp, while the blue and red profile was taken from a region that is further away.

Similar to the polished aluminum, each thermocouple on the painted aluminum surface during the angle of attack sweep showed an abrupt temperature change that signified transition. This is shown in Figure 45 for the heat lamp and Figure 48 for water circulation. However, the IR image, as described above, showed no temperature step but only a gradual change in temperature from the leading edge to trailing edge. The two temperature measurements appeared to not agree. Both the thermocouple and IR temperature measurements are shown in Figure 48. Of the two thermocouples, the downstream measurement was typically warmer than the upstream one. This is expected considering boundary layer growth will cause the downstream sensor to be warmer than the upstream sensor for the same boundary layer state. The IR measurement, however, showed a cool downstream measurement and a warm upstream one, and there were no shifts in temperature that signified transition. A likely explanation is that the thermal conductivity of the aluminum diffused the temperature step in the surface so that at it was merely a gradual gradient across the chord. This is what is measured by the IR camera. The thermocouples, however, were embedded within a thermally insulated adhesive and could maintain a larger temperature difference across its thickness. Also, the point of measurement was not actually the surface but a point within the adhesive pad just above the surface. The local convection rate affects the temperature gradient across the thickness of the adhesive pad and therefore the measured temperature of the thermocouple.

Essentially, the thermocouple adhesive pad and the aluminum surface had different Biot numbers. The high conduction rate within the aluminum, and therefore low Biot number, tends to keep the temperature of the model at a near uniform temperature, inhibiting observable effects of local convection rates. The thermocouple experienced convection effects more than the aluminum surface because of the lower conduction rates, and therefore higher Biot number. Consequently, the thermocouples give more information about the boundary layer state than does the model surface temperature.

The transient response of the model is shown in Figures 49 and 50. Figure 50 demonstrates the speed with which the system responds. Most of the response occurs while the model was pitching. Figure 49 shows, however, that the magnitude of this change is small.

7.4 Aluminum with Surface Wrap

The aluminum model coated with various insulation wraps produced similar results to the painted aluminum. Several areas of the Monokote® were not properly adhered to the painted aluminum surface as shown in Figures 51 and 56 and consequently were cooler because of the insulating layer of air under the coating. However, a temperature profile could be extracted from the IR image that included only regions that were properly adhere. This did not include the turbulent region from the trip strip as shown in Figures 52 and 57. The temperature profile for the clear wrap using tap water, Figure 67, and for the Monokote® using tap water, Figure 57, both cooled gradually towards the trailing edge exactly like the painted aluminum shown in Figure 47. The temperature profiles for the heat lamp, Figure 62 for the clear wrap and Figure 52 for the Monokote®, were similar to the painted aluminum, shown in Figure 44, in that the heat lamp produced warm temperatures in the middle that cooled towards the trailing edge. However, unlike the painted aluminum, few reflections of the lamp appeared in the IR image though both coatings were very smooth and glossy. The reflections appeared to be outside of the field of view of the camera as designed.

The results after painting and wet-sanding the clear, self-adhesive plastic wrap showed signs of a temperature step when used with water circulation as shown in Figure 76. However, the step was too gradual to identify transition accurately. Reflections from the heat lamp, shown in Figure 71, revealed very small scratches in the paint from sanding. This was considerably different from the unpainted version of the plastic wrap. These tiny scratches scattered IR at several different reflection angles, many of which were in the field of view of the camera, causing major interferences in the IR image and therefore the temperature profile as seen in Figure 72.

The time history of the temperature from the surface thermocouples shown in Figures 53, 58, 63, 68, 73 and 78 all show temperature steps similar to that seen for the painted aluminum in Figures 45 and 48 and even for the polished aluminum in Figure 42. The temperature steps seen in these figures are despite there not being a step in the temperature profiles. A likely reason for this is the thermal properties of the adhesive pad surrounding the thermocouple as explained in the previous subsection.

The response times for the heat lamp and water circulation for each configuration, Figures 55 and 60 for Monokote®, Figures 65 and 70 for clear wrap, and Figures 75 and 80 for the painted wrap show a very rapid response such that most of the transient response occurs as the model is pitching. By the time the model has finished pitching it has nearly reached thermal equilibrium. The transient profiles for the Monokote®, shown in Figure 54 for the heat lamp and Figure 59 for the water circulation, revealed a larger transient temperature change than for the clear wrap shown in figure 64 for the heat lamp and Figure 69 for the water circulation. The transient profiles for the painted wrap, shown in Figure 74 for the heat lamp and Figure 79 for the water circulation, revealed even larger temperature changes than the Monokote®, shown in Figures 54 and 59. This was especially true for water circulation, shown in Figure 79, which corresponds to the only configuration of the three surface wraps to identify transition. These temperature changes were relatively small compared to the RP configurations discussed later.

7.5 Aluminum with Bondo®

The aluminum model covered in a thin layer of painted Bondo® produced a severe reflection under the heat lamp as shown in Figure 81. This reflection was similar in shape to the polished aluminum, Figure 37, though much less in magnitude. Even outside of the reflection, no temperature step could be identified in the temperature profile when using the heat lamp, as shown in Figure 82. As with the other sanded surfaces, the reflections in the IR image of Figure 81 revealed tiny scratches in the surface from sanding. These scratches scatter IR in several reflection angles, many of which were in the field of view of the camera. Circulating tap water instead of using the heat lamp produced images in which a temperature step could be identified as seen in Figure 86. However, the surface could not maintain a sharp enough gradient necessary to identify transition accurately as seen in the temperature profile in Figure 87. At 50% chord, the black profile is clearly warmer than the turbulent reference in red and becomes the same temperature around 63% chord, but a particular transition location is not clear. Comparing the Bondo® in Figure 87 to the painted wrap in Figure 77, the painted wrap produced a sharper temperature gradient and therefore a more conducive temperature profile for measuring transition.

The temperature measurements of the surface thermocouples revealed transition-induced temperature steps as seen in Figure 83 for the heat lamp and Figure 88 for the water circulation. In both cases the temperature step occurred almost wholly at one change in angle of attack, whereas in other configurations such as the painted aluminum shown in Figure 45 for the heat lamp and Figure 48 for the water circulation, the change or each thermocouple occurred across multiple changes in angle of attack.

Transient data for the heat lamp is presented in Figures 84 and 85. However, the reflections, shown in Figure 84 as the intense spike, affected most of the data and very little surface temperature data could be taken from it. The transient profiles for the water circulation, shown in Figure 89 show a temperature change similar to the painted wrap shown in Figure 87. Transition in Figure 89 occurred at the location where the temperature profiles began to diverge around 52% chord. The transient response shown in Figure 90 was similar to most other aluminum configurations and showed a very quick response, having nearly reached equilibrium by the time the model had finished pitching.

7.6 RP Plastic As-Built

IR images of the RP plastic model appeared to contain high intensity reflections when tested with the heat lamp as shown in Figure 91. These reflections are the result of the tiny chordwise ridges on the surface and can be seen in the measured surface data in Figure 15. As discussed with the polished aluminum, directional variations in absorptivity and emissivity may also have contributed to the high intensity disturbance. For reference, the as-built RP is shown with no airflow in Figure 160 without the heat lamp and Figure 161 with the heat lamp. These show the directional variations without the variation caused by convection rates.

Despite the intense IR interference, a well-defined temperature step could be seen in the transient temperature profiles in Figure 94 when the transition location was different from the reflection location. This is not as evident in the single profile shown in Figure 92 because the scaling of the plot is set to capture the magnitude of the reflection. The reflections were not an issue when circulating ice water through the model, as shown in Figures 96 and 97, and a distinct transition location could be seen for every angle of attack. The temperature profile in Figure 97 is similar to the ideal temperature distribution shown in Figure 5.

Distinct medium-scale fluctuations could be seen in the temperature profile of most RP plastic configurations using internal water circulation as shown in Figure 97. This was a product of the internal structure of the RP plastic surface. The cross-hatching pattern shown in Figure 14 connected intermittent regions of the outer RP surface to the inner surface that contacted the temperature-controlled aluminum frame. All other regions were insulated by pockets of air. The connected regions would conduct heat between the surface and the aluminum frame quicker than other regions, creating fluctuations in the surface temperature profile. The alignment pins, which were also an internal component, could be clearly seen in the IR image shown in Figure 96 as cool regions at 15% and 42% chord.

The response of the RP plastic for both the heat lamp and water circulation were similar as shown in Figures 95 and 99 and were significantly slower than the aluminum model as demonstrated in Figure 50 for the painted aluminum. The response behavior was also measured by the surface thermocouples shown in Figure 93. A temperature drop signifying transition occurs at -2° angle of attack for the thermocouple at 60% chord and at 4° for the thermocouple at 25% chord. These temperature changes were not as instantaneous as was seen for the aluminum, such as in Figure 45 for the painted aluminum with the heat lamp, but rather contained a pattern of exponential decay. The tunnel temperature, shown in Figure 93, was unsteady and affected the thermocouple measurements, as also seen in Figure 93. This did not affect the ability of the IR image to observe a transition location. The insulating properties of the RP plastic surface allowed it to maintain a temperature step but appeared to increase the response time needed to reach equilibrium. The response time for the as-built RP was typical of all other RP plastic configurations.

7.7 Sanded RP Plastic

The reflections from the heat lamp were much less intense on the sanded RP plastic surface but were spread out across a larger percentage of the IR image as seen in Figure 100 and the associated temperature profile in Figure 101. These reflections revealed tiny ridges and scratches, likely due to sanding and the remnants of the ridges described for the as-built configuration. Warm and cool regions were seen, but a transition location could not be determined amidst the reflections in the temperature profile shown in Figure 101. The transient profiles seen in Figure 103 show transition more clearly as the point, located around 45% chord, where the profiles diverge. However, using internally circulated ice water showed a very discernible temperature step and transition location as seen in the IR image in Figure 105 and the temperature profile in Figure 106.

The time history of the thermocouple measurements in Figure 102 and 107 show a similar time-dependent decay as the temperature changes because of transition. However, this occurs at a higher angle of attack than for the as-built configuration shown in Figure 93. This was likely the result of sanding the streamwise ridges in the as-built configuration to a smoother surface, causing transition to delay until further downstream.

The transient profiles presented in Figure 108 show a clear progression of the temperature step from one equilibrium state to another. The response time using the heat lamp, shown in Figure 104, is marginally quicker than using internal water circulation, shown in Figure 109. This is expected as the heat lamp radiates heat directly to the surface and does not require conduction as internal heating does.

7.8 Painted RP Plastic

Painting the RP black significantly increased the temperature of the surface and the magnitude of the temperature step while using the heat lamp as seen in comparing the temperature profiles in Figures 101 and 117. Both the heat lamp and the ice water produced discernible temperature steps and transition locations, shown in Figures 117 and 127. However, there were significant reflections from the heat lamp as shown by the temperature spike in Figure 117 that would interfere with a transition measurement when both transition and the reflection were at the same location. This reflection appeared minor in comparison to other configurations, particularly the as-built RP configuration as shown in Figure 92.

The paint appeared to decrease the response time when using heat lamps as indicated by comparing the temperature change during pitch of the painted RP in Figure 120 and the sanded RP in Figure 104. The reason for the transient behavior when used with ice water, shown in Figure 131, is uncertain. The variation of conduction rates caused by the internal cross-hatched structure of the RP may have affected the response. However, this response was unique to this configuration. Perhaps water from condensation was present within the model and influenced the response. Condensation occurred later on the aluminum model.

The results of changing the airspeed were examined on the painted RP configuration. As expected, the transition location was further downstream at lower Reynolds numbers, as seen in comparing Figures 111, 114 and 117 for the heat lamp. This same set of figures also shows a decrease in both the magnitude and the gradient of the temperature step as the Reynolds number is increased. This is also seen for the ice water circulation in Figures 122, 125 and 128. This trend is expected and demonstrates the need for a higher heat flux into the surface at increased airspeeds.

The surface temperatures measured by the thermocouples and the tunnel air temperature are given for reference in Figures 112, 115, and 118 for the three Reynolds numbers using the heat lamp and in Figures 123, 126, and 129 for the three Reynolds numbers using internal water circulation. All surface thermocouple measurements showed an exponential decay when changing temperature.

7.9 RP with Bondo®

An identifiable transition location could be seen in the IR images for nearly all angles of attack for both the heat lamp and the internal tap water circulation. This is shown for 0° angle of attack in Figures 132 and 137. The temperature gradients at transition were sharp for both heating methods as seen in Figure 133 for the heat lamp and Figure 138 for the water circulation. This increases the accuracy of the transition measurement. While the tap water produced a slightly sharper gradient and more pronounced peak in the temperature profile, the profile for the heat lamp was smoother. This is because of the internal structure of the RP as discussed earlier.

There were not many spikes in the temperature profile from reflections of the heat lamp as shown in Figure 133. Perhaps fewer reflections were the result of the surface being less rough than the painted RP, an R_A of 0.35 μm compared to 0.68 μm. These numbers are listed in Table 1. A smoother surface would reduce the scatter of IR from the heat lamp, resulting in less reflected IR detected by the camera. However, the surface was not free of reflections as shown in the IR image in Figure 132. The unpainted Bondo®, left unpainted for comparison purposes, contained reflections and was cooler than the painted regions when the heat lamp was used. The painted Bondo® also contained reflections but primarily located closer to the heat lamp. This region, located at the bottom of the IR image in Figure 132, is the only region that was difficult to confirm where transition was located.

The unpainted area of Bondo® had a rougher finish and could be subtly identified in the IR image. Because of the thickness of the paint, there was a step in thickness going from the unpainted to the painted surface. While very subtle, this spanwise-facing step appeared to cause early transition in the IR image shown in Figures132 and 137.

When comparing the response for using the heat lamp on the Bondo®, shown in Figure 136, and the painted RP, shown in Figure 120, the added layer of Bondo® appeared to slow the response time. The response for the Bondo® using tap water circulation, shown in Figure141, is marginally quicker than using the heat lamp, shown in Figure136. The responses were all very similar, which makes it is difficult to conclude decisively which configuration responded quicker.

In addition to the IR images and temperature profiles, the thermocouple measurements are given for reference in Figures 134 and 139 for the heat lamp and water circulation respectively. These plots include measurements of the surface temperature and the tunnel air temperature.

7.10 RP with Monokote® layer

A clear transition location could be determined for all angles of attack when Monokote® was layered over the Bondo® on the RP plastic model. This was true for both heating methods as shown in the IR images in Figures 142 and 147 and the associated temperature profiles in Figure 143 and 148.There were no reflections from the heat lamp to interfere with observing the surface temperature profile as shown in Figure 143. Similar to the aluminum model with Monokote® or the clear plastic wrap, the heat lamp reflection was outside the field of view of the camera as designed. However, the surface was certainly reflective as seen by camera's own reflection in Figures 142 and 147. Therefore the IR intensity measured by the camera was a combination of reflected and emitted IR radiation. However, the intensity of the reflected IR that is detected by the camera is significantly less with the heat lamp reflection outside the camera's field of view.

The response times of both heating methods were comparable. The heat lamp response shown in Figure 146 may have been quicker than the water circulation response shown in Figure 151 as indicated by the time constant for the exponential fit. However, it is difficult to distinguish small changes based on the fit because much of the response occurs before the model is finished pitching and is not accounted for in the fit.

Though covered with Monokote®, the chordwise step in the Bondo® appeared to influence the transition front, as seen from the inconsistent location of the temperature step in Figures 142 and 147. This could also have been the result of air trapped under the Monokote® at the face of the chordwise step. However, there was no other indication of trapped air causing temperature variations. If there had been trapped air there would be indications at chord locations other than transition.

7.11 Vortex Generators

In both VG configurations, the VGs tripped the boundary layer and everything directly downstream was turbulent as seen in Figures 152 –154. Figure 153 compares the temperature profile in the wake of a VG to the temperature profile outside the influence of the VG. The turbulence caused by the VGs spread out in the spanwise direction as the flow moved downstream so that the entire region behind an array of VGs was turbulent at some distance downstream. Any laminar regions passing between VG pairs, such as that shown in Figure 154, were overtaken by the surrounding turbulent regions. The point at which these laminar regions become turbulent is dependent on the angle of attack, but never do they align with the transition location outside of the VG influence. Regions influenced by the VGs always transitioned further upstream than the regions outside of the influence of the VGs, even when the transition location was upstream of the VGs as seen in Figures 156 and 157.

8. CONCLUSION

The results show that IR reflections and heat dissipation on the model are the primary factors inhibiting the measurement of transition location using an IR camera. All response times for RP configurations were comparable and adequately short. The aluminum configurations responded much quicker than the RP but were universally less capable of accurately identifying transition. In all configurations except the RP plastic wing covered with Monokote®, the heat lamps produced inferior results compared to internal water circulation because of the intense reflections off of the surface.

Polished, bare aluminum test models, even with internal water circulation, are altogether incompatible to this measurement technique. Solid aluminum does not perform well because the high thermal conductivity of the material quickly dissipates the heat and eliminates any sharp temperature steps that might otherwise exist. Covering the model with an insulator slightly improved the temperature step, as seen with the painted plastic wrap. However, this was the only wrap to successfully measure transition. This wrap was black unlike the unpainted version of the same wrap and therefore able to absorb and emit more IR radiation. It was also thicker than the Monokote®, providing more insulation at the surface. Temperature differences could be seen on the layer of Bondo®, but not sharp enough to measure transition. Because the thickness of the Bondo® is similar to the plastic wrap, it is assumed that the thermal properties of the Bondo® make it less insulating. The only aluminum configuration to successfully measure transition was the self-adhesive plastic wrap that was painted black and used with internal water circulation.

A possible improvement to the results from aluminum might be achieved by reducing the wall thickness of the aluminum model from a solid design to some finite thickness. In the research by both Carpenter (2009) and Bæk (2008), IR transition detection was successfully used on an aluminum model. They were both black in color and coated with a thin insulator, similar to the aluminum model presented in this thesis. In both cases, however, the model had thin walls, which limited the internal heat conduction.

The RP test model successfully measured transition location in all tested configurations. However, a transition location could not be determined for every angle of attack when using the heat lamp. Transition could only be seen when the transition location and heat lamp reflection were at different locations as seen from the IR camera. When using internal water circulation, a transition location could be measured for all configurations and at all tested angles with little difference between each configuration visible in the IR images. It was also observed that metal pins inside of the RP surface could be seen in the IR image. The RP surface should be designed in such a way as to not inhibit the measurement of transition by the placement of these metal parts.

For nearly all configurations the reflections from the heat lamp caused interference to the IR image, preventing the discernment of a temperature step. This was despite the heat lamp being placed so that its nominal reflection would not be visible in the IR image. Therefore the reflections that were present in the IR image were the result of microscopic surface imperfections that scatter light in directions other than that for which it was designed for. This was the case even for the aluminum model that was sanded with fine grit sandpaper and then polished with fine steel wool.

However, both Monokote® and the unpainted, clear plastic wrap did not have issues with reflections from the heat lamp disrupting the IR image. Both coatings are extremely smooth and therefore scatter light and IR radiation in fewer directions. Even though both are glossy and certainly reflect some of the IR radiation from the heat lamp, the reflection is located outside of the field of view of the camera as designed. Consequently, if heat lamps are to be used at the LSWT, extreme care must be taken to ensure an adequately smooth surface. Smooth surface wraps, such as Monokote®, that are properly applied without trapping air pockets can effectively achieve this.

REFERENCES

Bæk P (2008) Experimental detection of laminar to turbulent boundary layer transition on airfoils in an industrial wind tunnel facility. Thesis, Technical University of Denmark, Copenhagen

Carpenter A (2009) In-fight receptivity experiments on a 30-degree swept wing using micron-sized discrete roughness elements. PhD Dissertation, Texas A&M University, College Station

Green JE (2008) Laminar flow control - back to the future?. In: 38th AIAA Fluid dynamics conference, AIAA 2008-3738, 23–26 June 2008, Seattle, Washington

Office of Energy Efficiency (2009) Lighting reference guide – incandescent lamps. Natural Resources Canada. http://oee.nrcan.gc.ca/publications/equipment/lighting/6571. 2012.03.21

Ricci R, Montelpare S, Artipoli G, Renzi E (2008) Thermographic analysis of mechanical disturbances effects on laminar separation bubble. In: 9th International conference on quantitative infrared thermography, 2–5 July 2008, Krakow, Poland

Rumerman J (2003) The first wind tunnels. U.S. Centennial of Flight Commission. http://www.centennialofflight.gov/essay/Evolution_of_Technology/first_wind_tunnels/Tech34.htm. 2011.12.21

White FM (1984) Heat transfer. Addison-Wesley, Reading, MA

APPENDIX A

TABLES

Table 1 Model Configurations with surface roughness and added thickness

Configuration	Roughness Measurement	R_A (µm)	R_y (µm)	Layers	Added Thickness
RP - As Built	Chordwise	0.58	4.25	none	
	Spanwise	17.27	76.15		
RP - Sanded	Chordwise	2.10	13.89	none	
	Spanwise	5.08	35.00		
RP - Painted	model Avg	0.68	4.94	P	50 µm
RP - Bondo	Painted Region	0.35	4.91	P+B+P	230 µm
	Unpainted Region	4.40	29.03		
RP - Monokote	model Avg	0.09	0.63	P+B+P+M	280 µm
Alum - Polished	model Avg	0.42	3.08	none	
Alum - Painted	model Avg	0.66	4.48	P	50 µm
Alum - Monokote	model Avg	0.09	0.63	P+M	100 µm
Alum - Clear Wrap	model Avg	0.13	0.72	P+W	125 µm
Alum - Painted Wrap	model Avg	0.50	3.82	P+W+P	175 µm
Alum - Painted Bondo	model Avg	0.62	4.27	P+B+P	230 µm

Layers: P = Paint; M = Monokote; W = Adhesive Wrap; B = Bondo

Table 2 List of test configurations for the RP plastic model

RP Configurations	**Heating Method**	**Re_c (10^5)**	**Type of Run**
As Built	Heat Lamp	6.6	AoA Sweep: -8° to 12°, Δ2°
		6.6	Transient: -4° to 0°, Δ4°
	Ice Water	6.6	AoA Sweep: -8° to 15°, Δ1°
		6.6	Transient: -4° to 0°, Δ4°
Sanded	Heat Lamp	6.6	AoA Sweep: -8° to 14°, Δ2°
		6.6	Transient: -4° to 0°, Δ4°
	Ice Water	6.6	AoA Sweep: -8° to 14°, Δ2°
		6.6	Transient: -4° to 0°, Δ4°
Painted	Heat Lamp	2.2	AoA Sweep: -8° to 14°, Δ2°
		4.4	AoA Sweep: -8° to 14°, Δ2°
		6.6	AoA Sweep: -8° to 14°, Δ2°
		6.6	Transient: -4° to 0°, Δ4°
	Tap Water	2.2	AoA Sweep: -8° to 14°, Δ2°
		4.4	AoA Sweep: -8° to 14°, Δ2°
		6.6	AoA Sweep: -8° to 14°, Δ1°
		6.6	Transient: -4° to 0°, Δ4°
Painted Bondo (with unpainted region)	Heat Lamp	6.6	AoA Sweep: -8° to 14°, Δ2°
		6.6	Transient: -4° to 0°, Δ4°
	Tap Water	6.6	AoA Sweep: -8° to 14°, Δ2°
		6.6	Transient: -4° to 0°, Δ4°
Monokote on painted Bondo	Heat Lamp	6.6	AoA Sweep: -8° to 14°, Δ2°
		6.6	Transient: -4° to 0°, Δ4°
	Tap Water	6.6	AoA Sweep: -8° to 14°, Δ2°
		6.6	Transient: -4° to 0°, Δ4°

Table 3 List of test configurations for the Aluminum model

Alum. Configurations	Heating Method	Re_c (10^5)	Type of Run
Polished	Heat Lamp	6.6	AoA Sweep: -8° to 12°, Δ2°
		6.6	Transient: -4° to 0°, Δ4°
	Ice Water	6.6	AoA Sweep: -8° to 14°, Δ2°
		6.6	Transient: -4° to 0°, Δ4°
Painted	Heat Lamp	6.6	AoA Sweep: -8° to 14°, Δ2°
		6.6	Transient: -4° to 0°, Δ4°
	Tap Water	6.6	AoA Sweep: -8° to 14°, Δ2°
		6.6	Transient: -4° to 0°, Δ4°
Monokote	Heat Lamp	6.6	AoA Sweep: -8° to 14°, Δ2°
		6.6	Transient: -4° to 0°, Δ4°
	Tap Water	6.6	AoA Sweep: -8° to 14°, Δ2°
		6.6	Transient: -4° to 0°, Δ4°
Clear Wrap	Heat Lamp	6.6	AoA Sweep: -8° to 12°, Δ2°
		6.6	Transient: -4° to 0°, Δ4°
	Tap Water	6.6	AoA Sweep: -8° to 12°, Δ2°
		6.6	Transient: -4° to 0°, Δ4°
Painted Wrap	Heat Lamp	6.6	AoA Sweep: -8° to 14°, Δ2°
		6.6	Transient: -4° to 0°, Δ4°
	Tap Water	6.6	AoA Sweep: -8° to 14°, Δ2°
		6.6	Transient: -4° to 0°, Δ4°
Painted Wrap: Lg VG	Tap Water	6.6	AoA Sweep: -8° to 16°, Δ2°
Painted Wrap: Sm VGs	Tap Water	6.6	AoA Sweep: -8° to 18°, Δ2°
Painted Bondo	Heat Lamp	6.6	AoA Sweep: -8° to 14°, Δ2°
		6.6	Transient: -4° to 0°, Δ4°
	Tap Water	6.6	AoA Sweep: -8° to 14°, Δ2°
		6.6	Transient: -4° to 0°, Δ4°

APPENDIX B

FIGURES

Figure 1 Hotfilm array installed on test wing surface

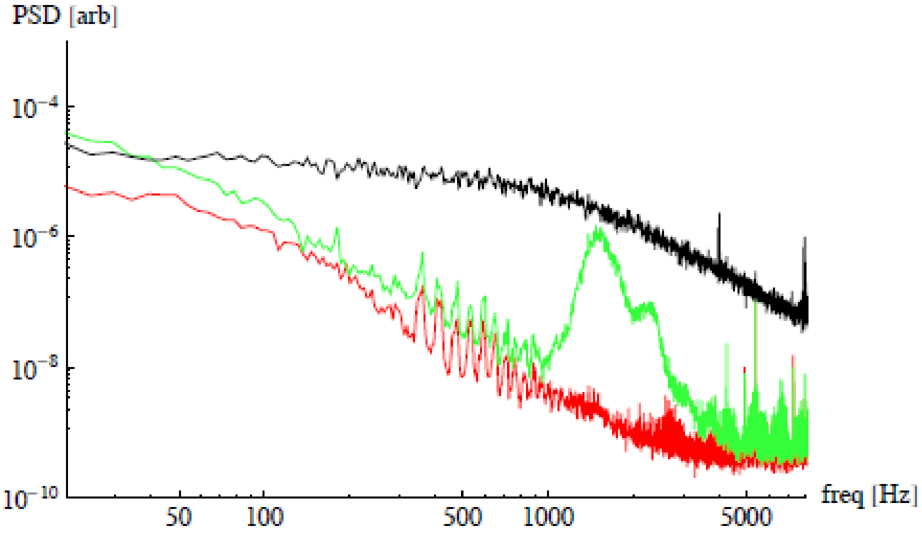

Figure 2 Example of voltage responses from hotfilms. Black is turbulent, red is laminar and the green is transitioning.

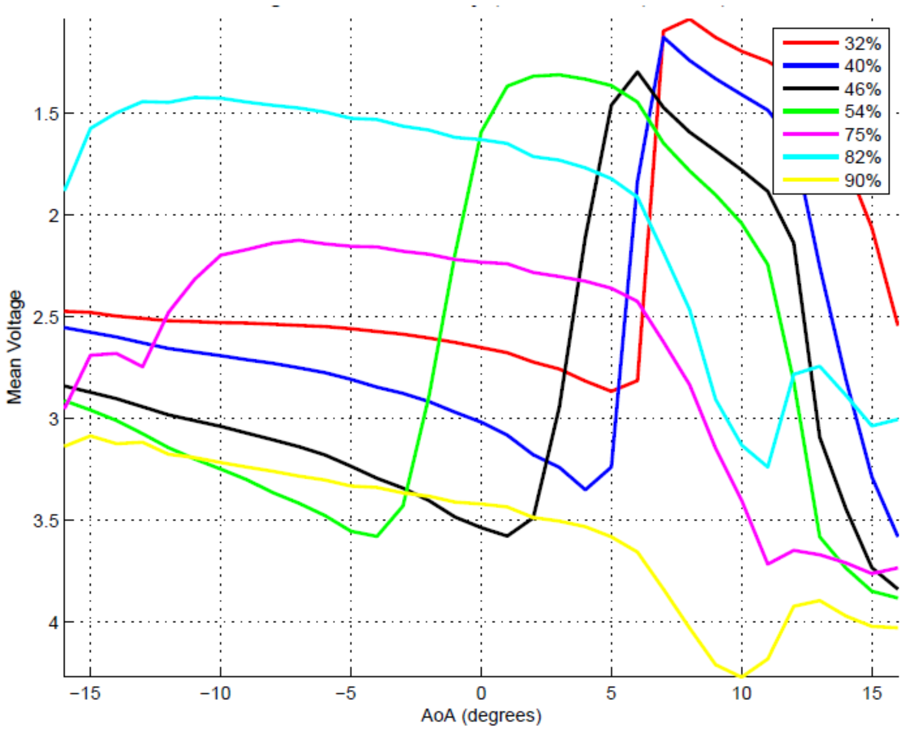

Figure 3 Example of mean voltage response from each hotfilm sensor as wing is pitched. The sharp step represents transition.

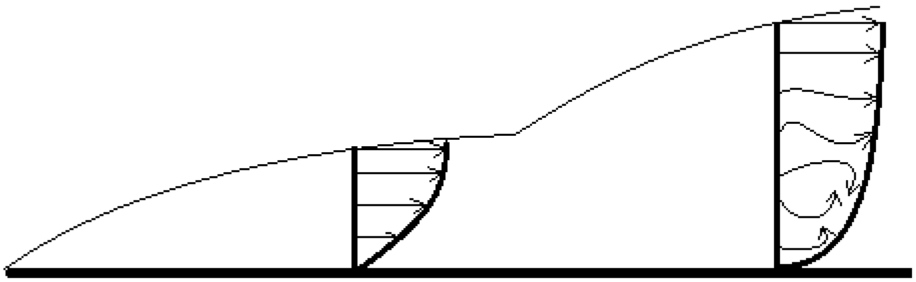

Figure 4 Diagram of boundary layer transition.

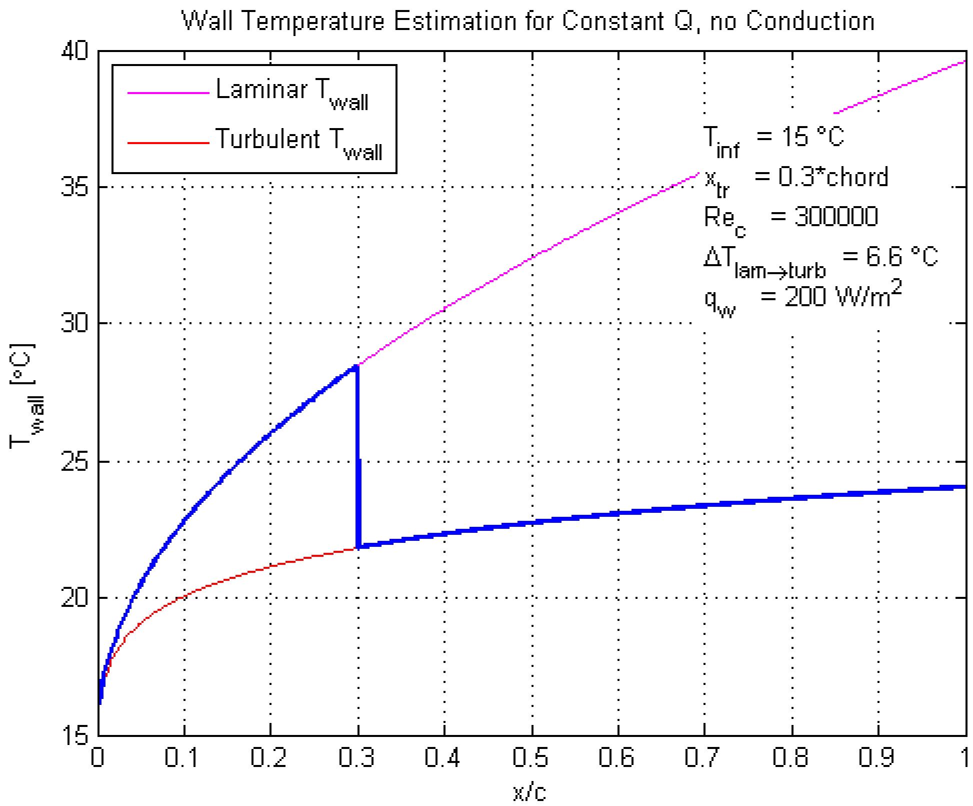

Figure 5 Example of theoretical temperature step for a flat plate with constant heat flux.

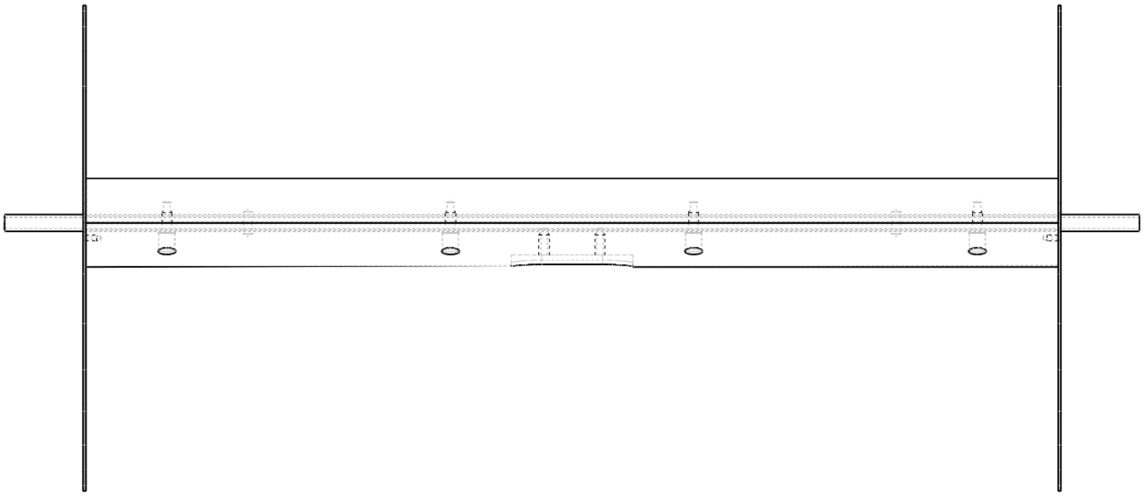

Figure 6 Aluminum Model – Front View

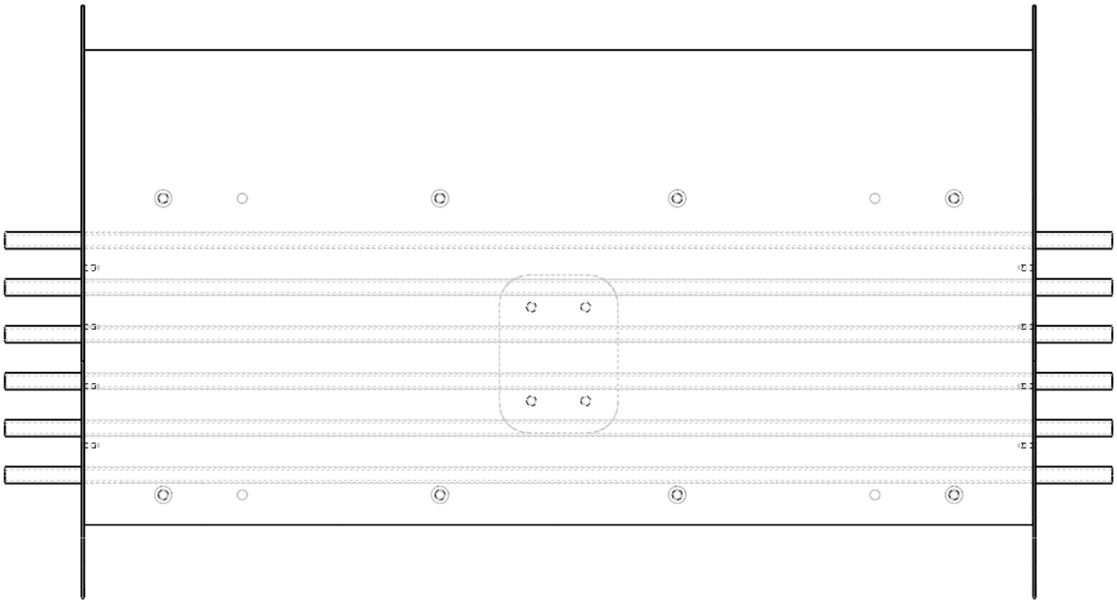

Figure 7 Aluminum Model – Top View

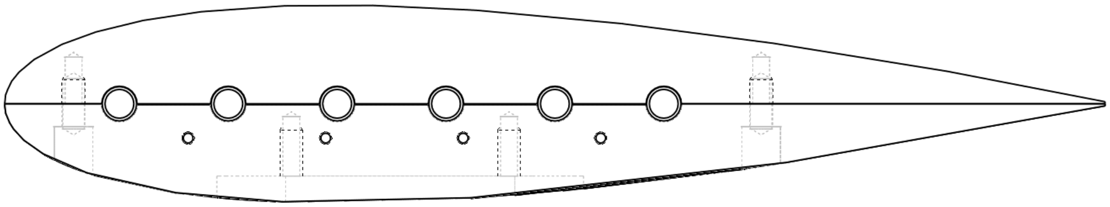

Figure 8 Aluminum Model – Side View

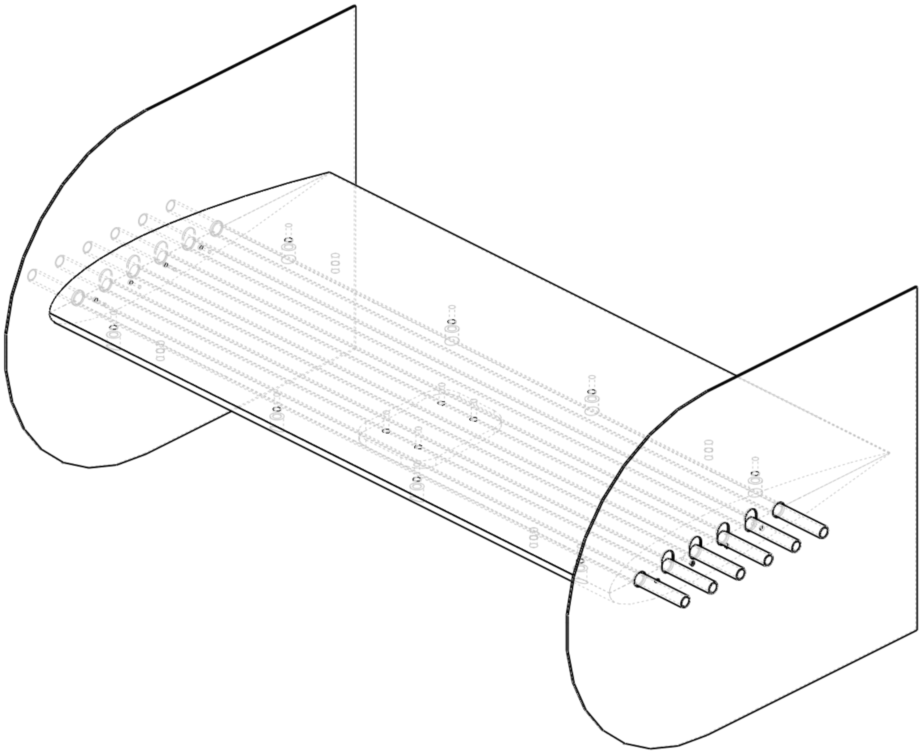

Figure 9 Aluminum Model – Isometric View

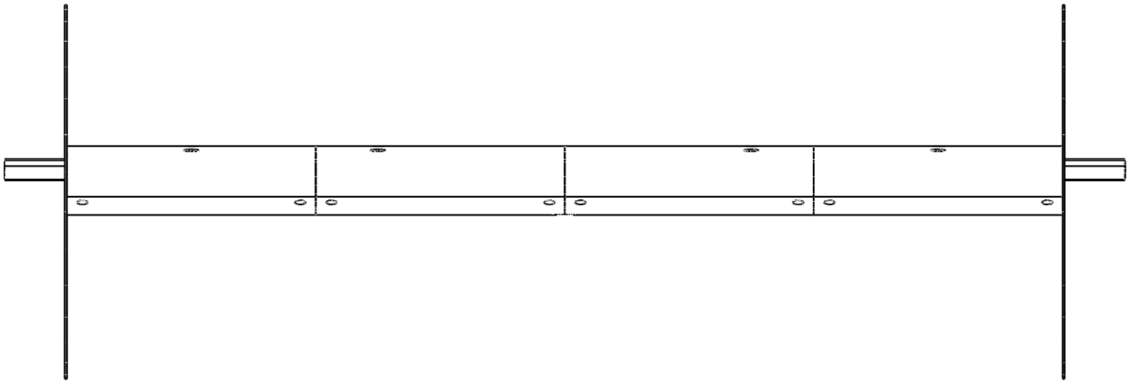

Figure 10 RP Model – Front View

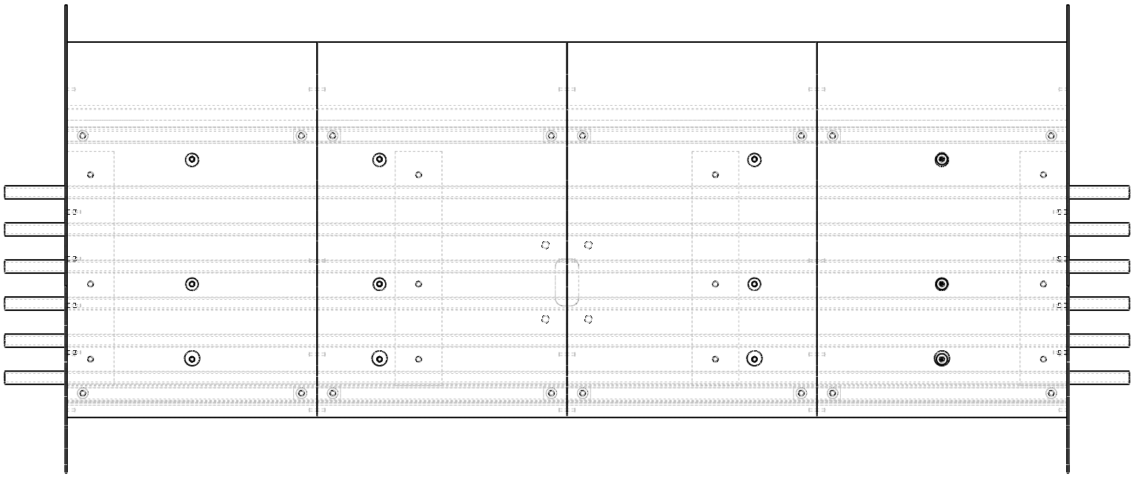

Figure 11 RP Model – Top View

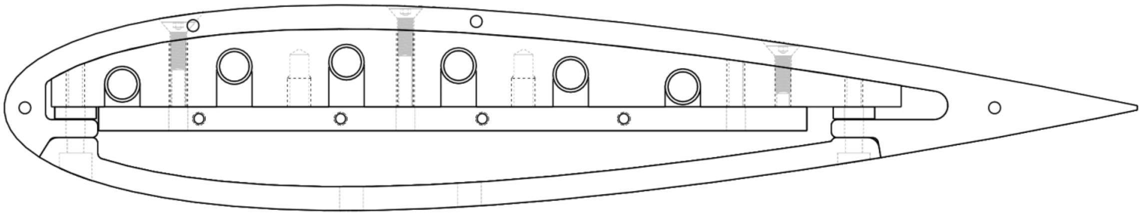

Figure 12 RP Model – Side View

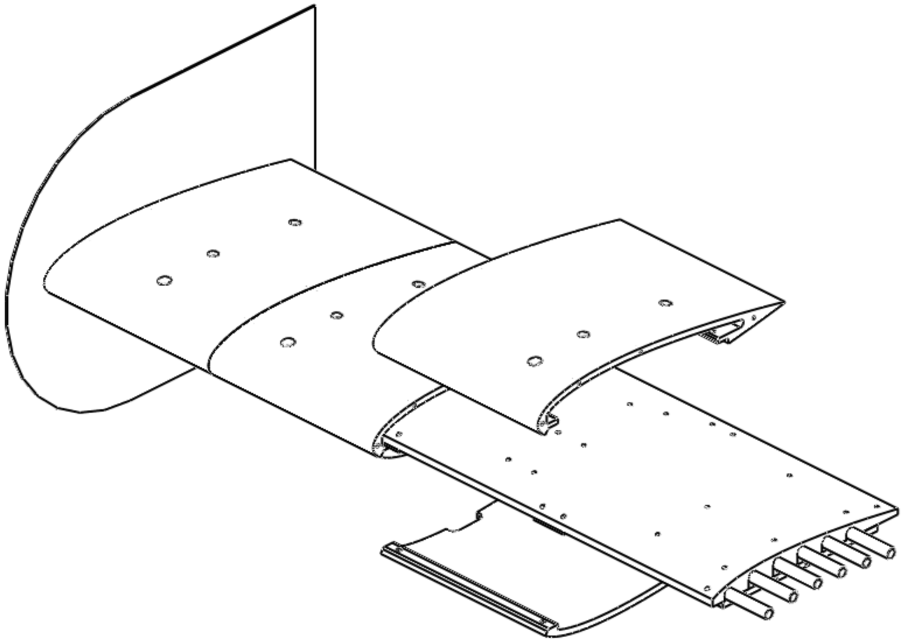

Figure 13 RP Model – Exploded Isometric View

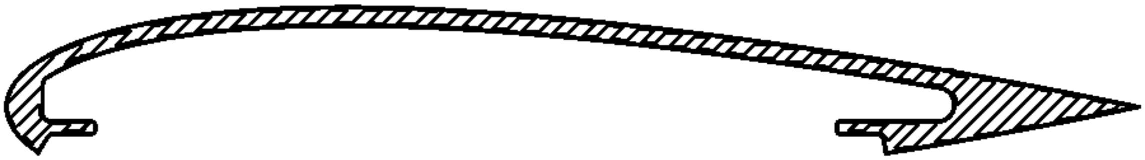

Figure 14 Internal structure of RP part showing cross-hatching pattern

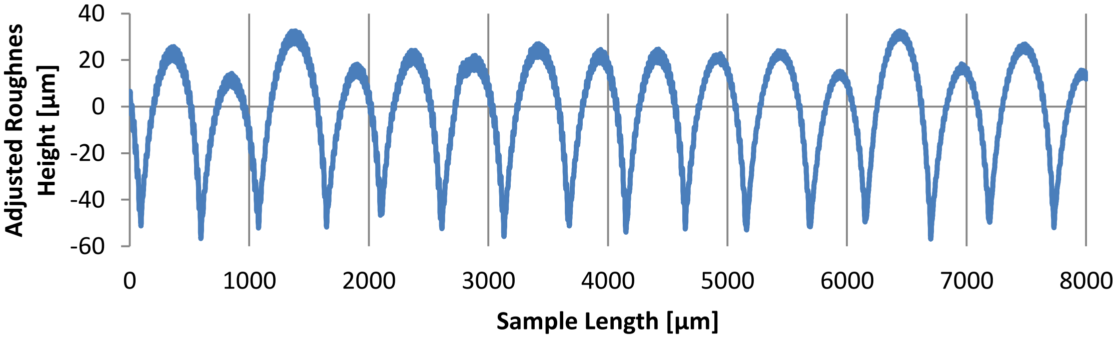

Figure 15 Spanwise surface profile of as-built RP

Figure 16 Pitching mechanism in the test section

Figure 17 Test section ceiling covered with black paper and showing the lamp mounted in the ceiling hole (left) and the hole cut for the camera (right).

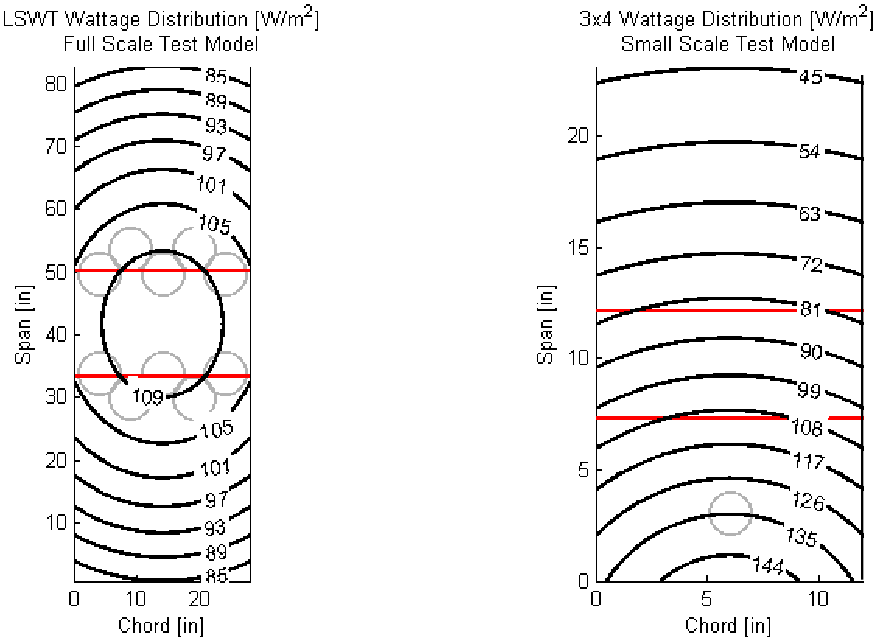

Figure 18 Distribution of heat on the test model at LSWT (left) according to an existing design and in the 3'x4' wind tunnel (right) under the current setup; red lines indicate the viewing area of the camera and grey circles represent the expected heat lamp reflections

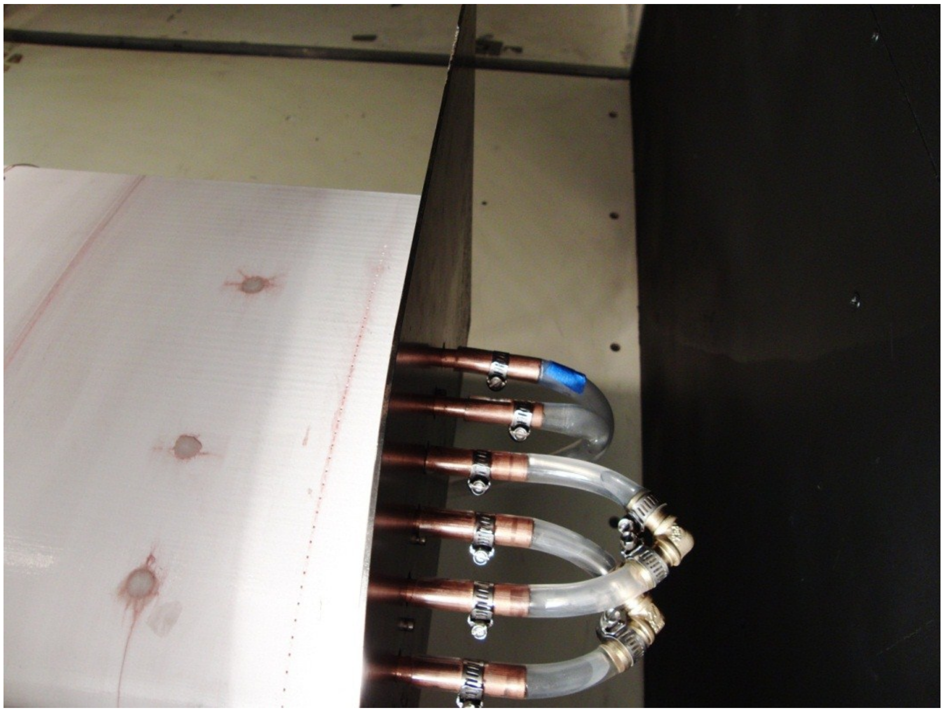

Figure 19 Circulation lines connected to model

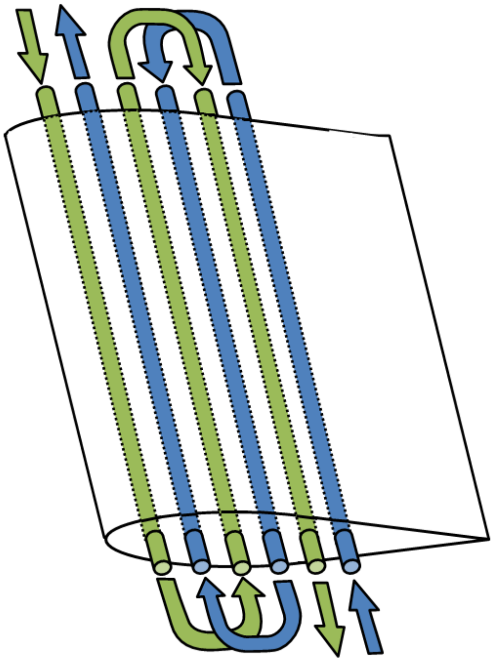

Figure 20 Diagram of two internal circulation routes flowing in opposite directions for even temperature distribution

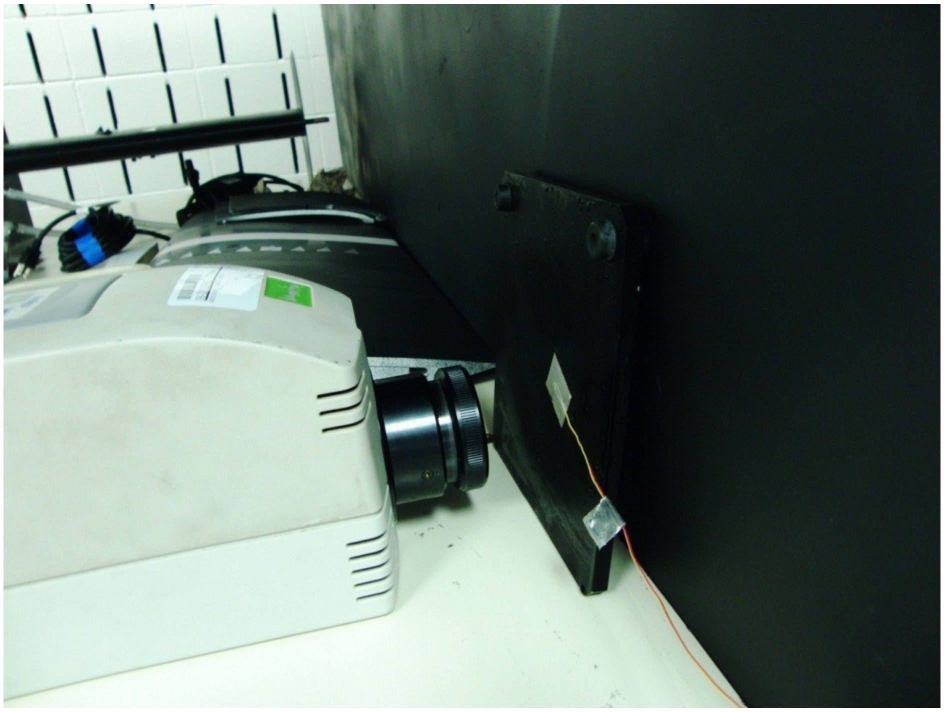

Figure 21 Camera calibration setup, shown with camera away from plate

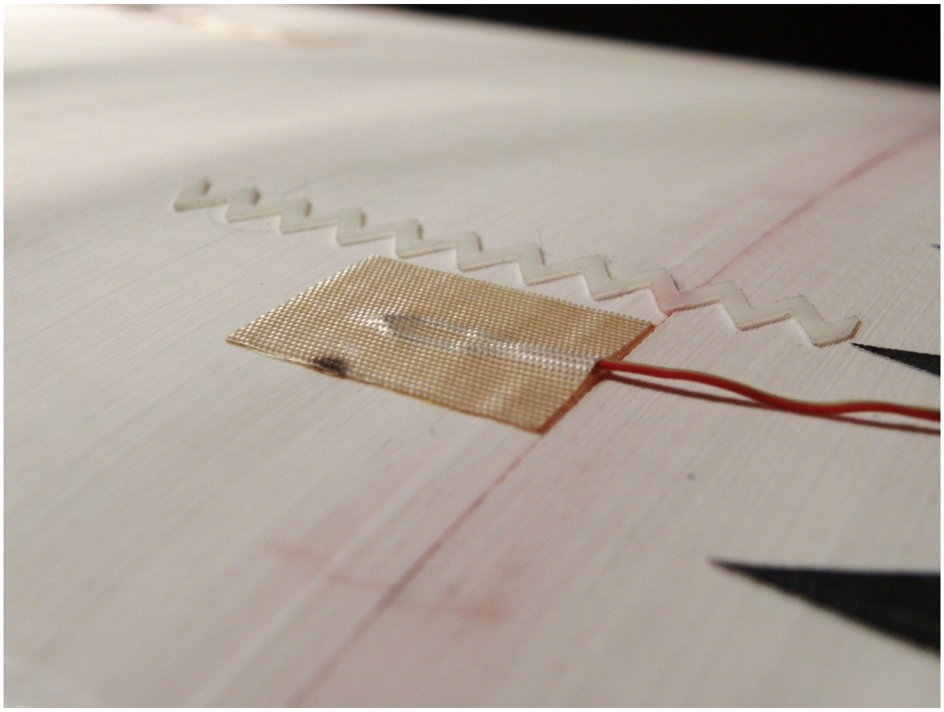

Figure 22 Thermocouple adhered to surface

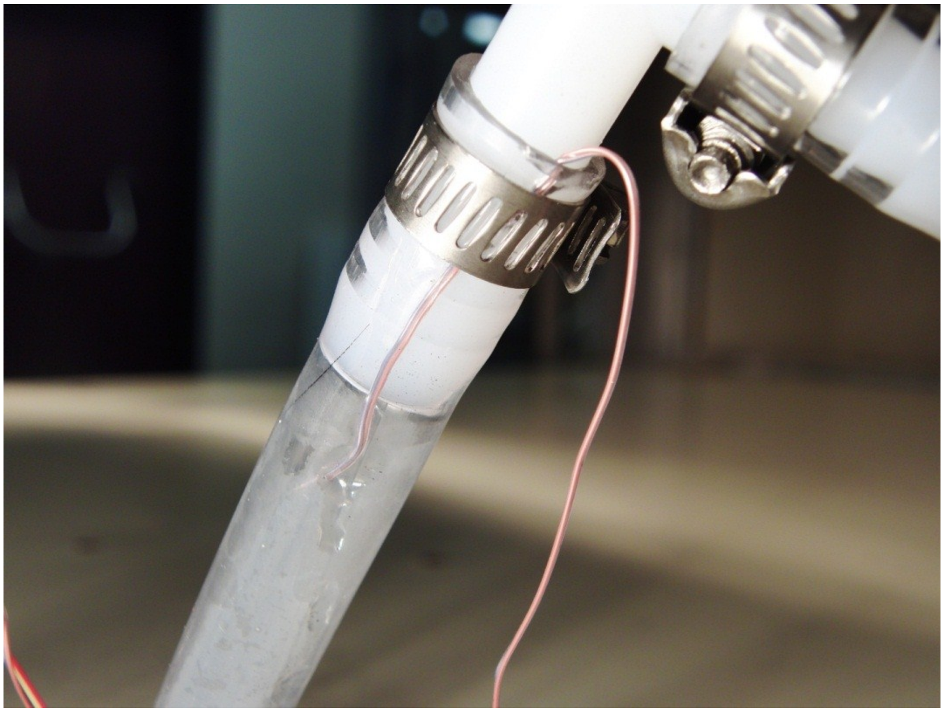

Figure 23 Thermocouple installed in water line

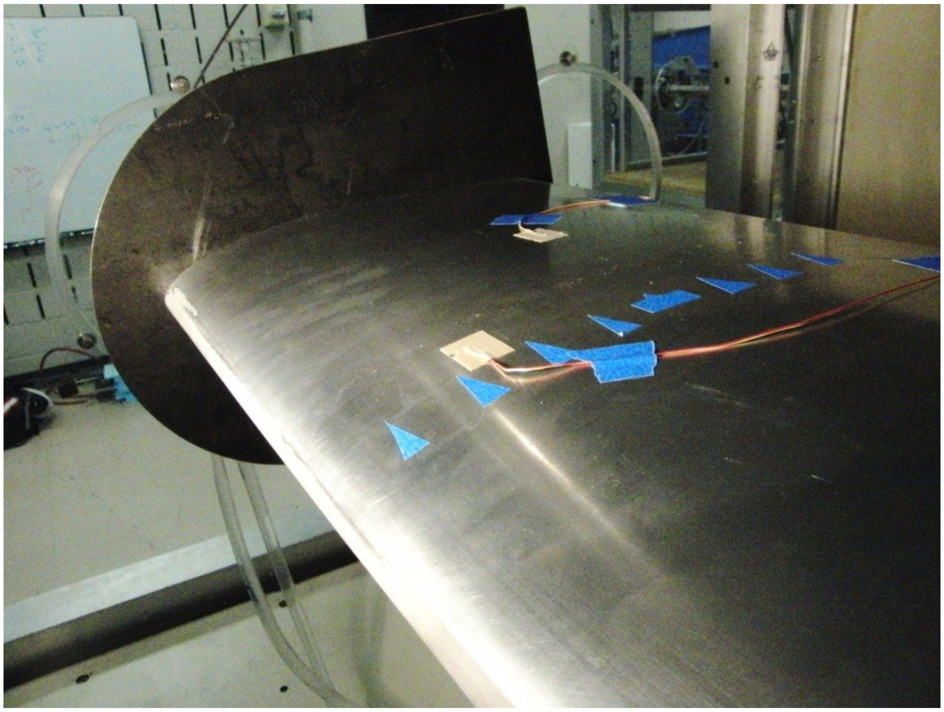

Figure 24 Polished aluminum test model

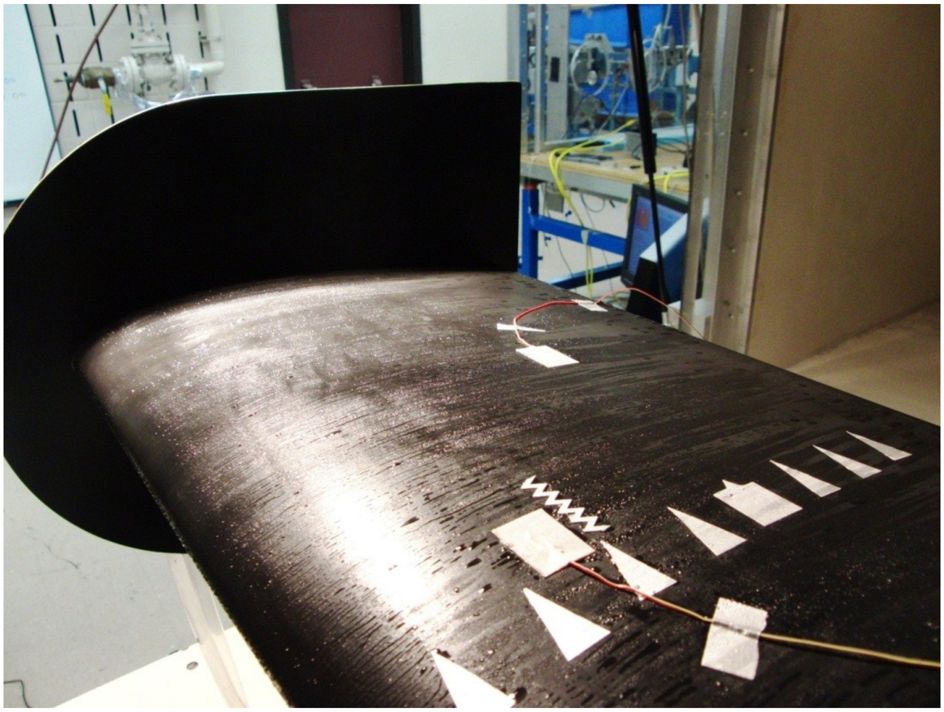

Figure 25 Painted aluminum test model shown with condensation droplets formed when using ice water circulation.

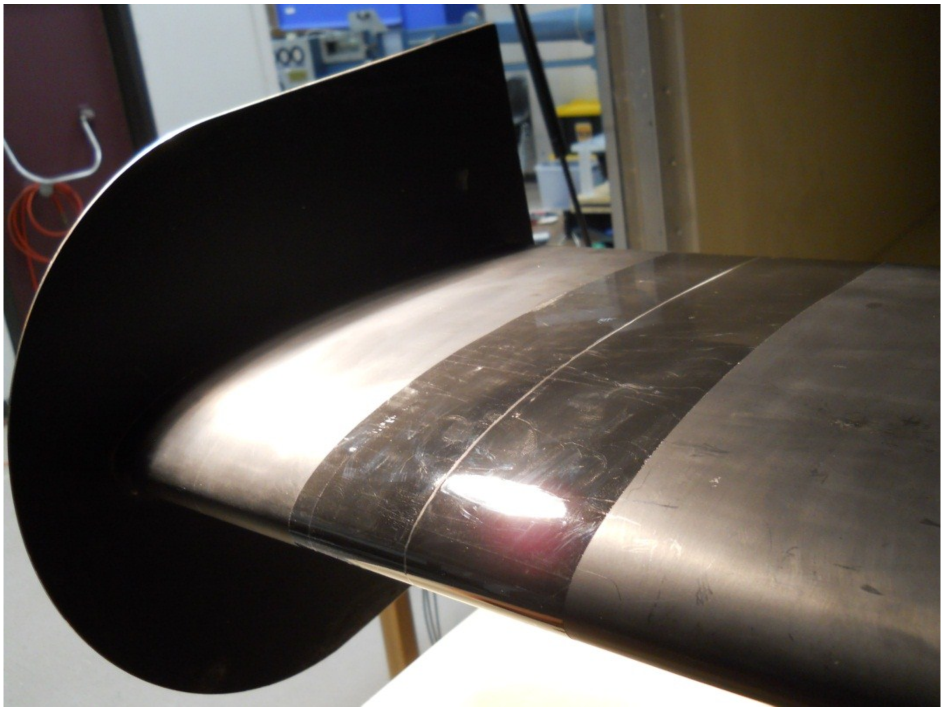

Figure 26 Painted aluminum with clear plastic wrap; Sample application shown, actual test application of wrap covered larger area as shown in Figure 27.

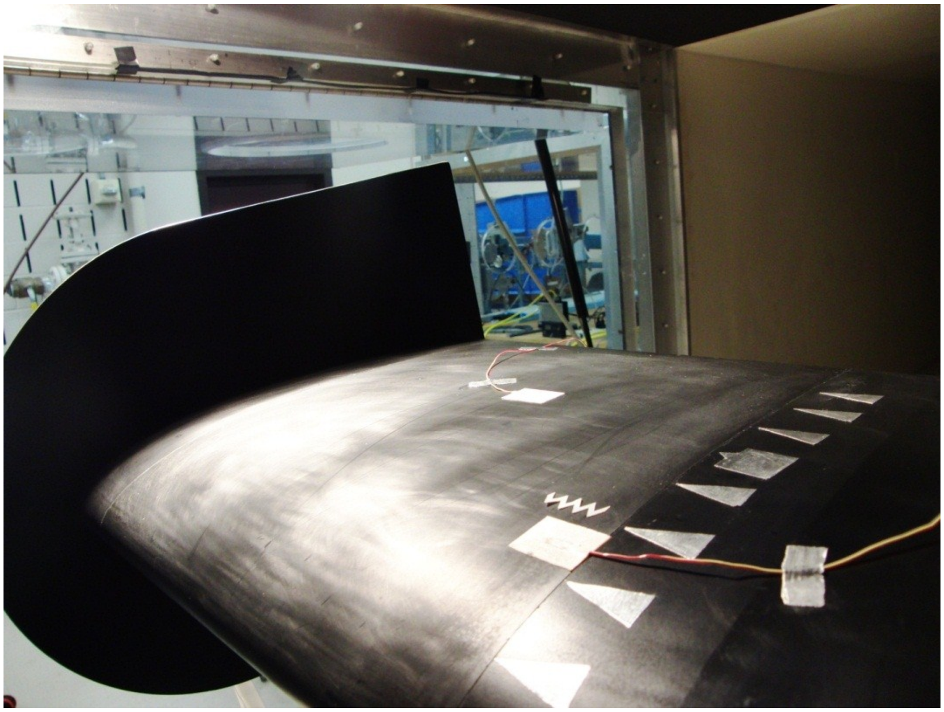

Figure 27 Painted aluminum with painted plastic adhesive wrap

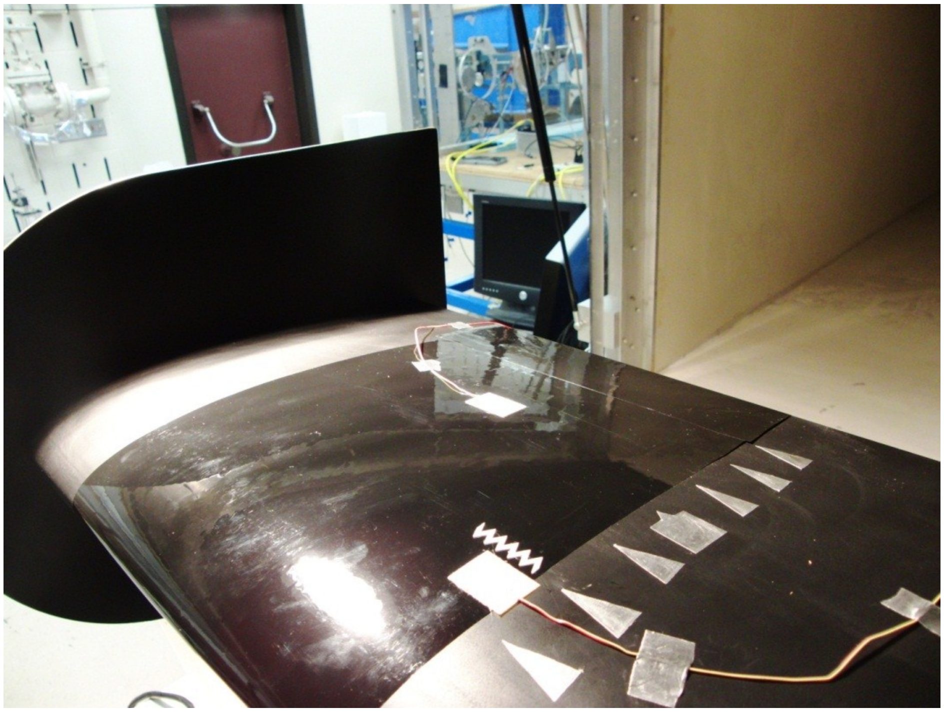

Figure 28 Painted aluminum test model with Monokote

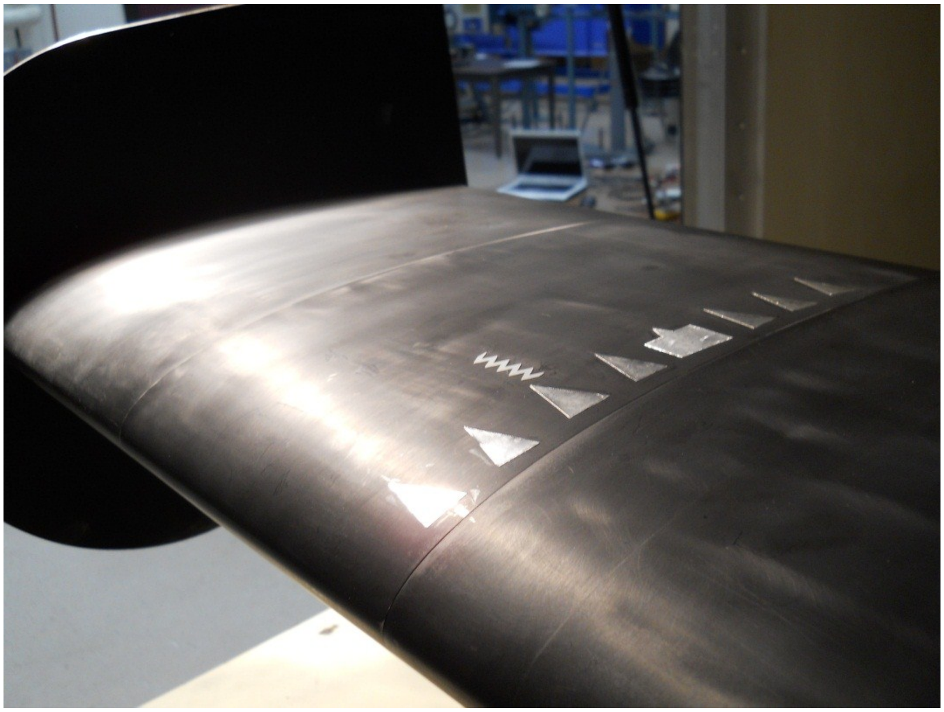

Figure 29 Aluminum model with painted Bondo

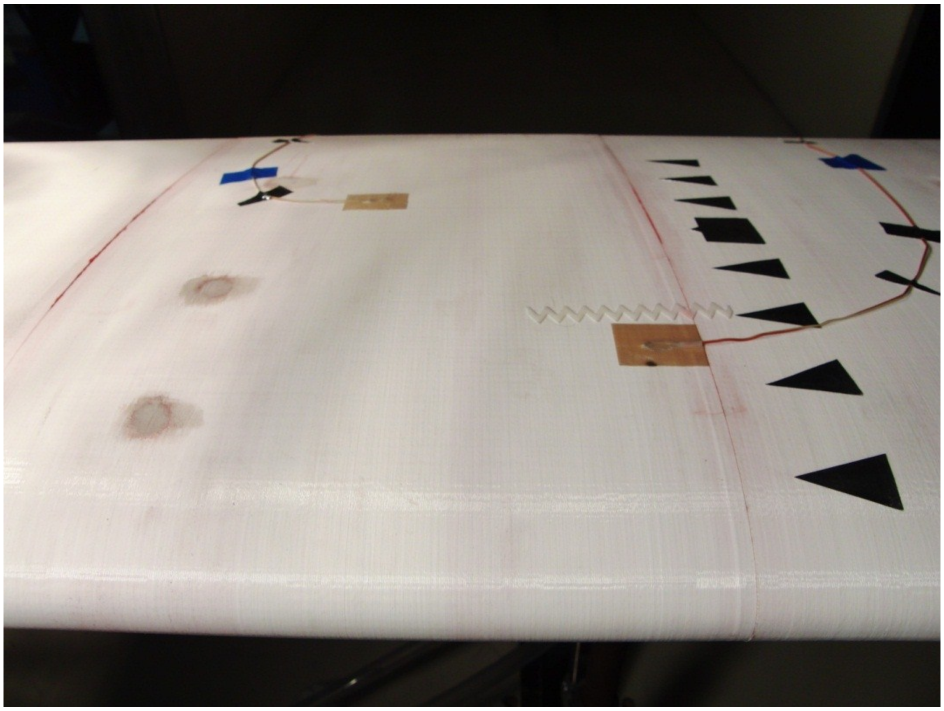

Figure 30 As-built RP plastic test model

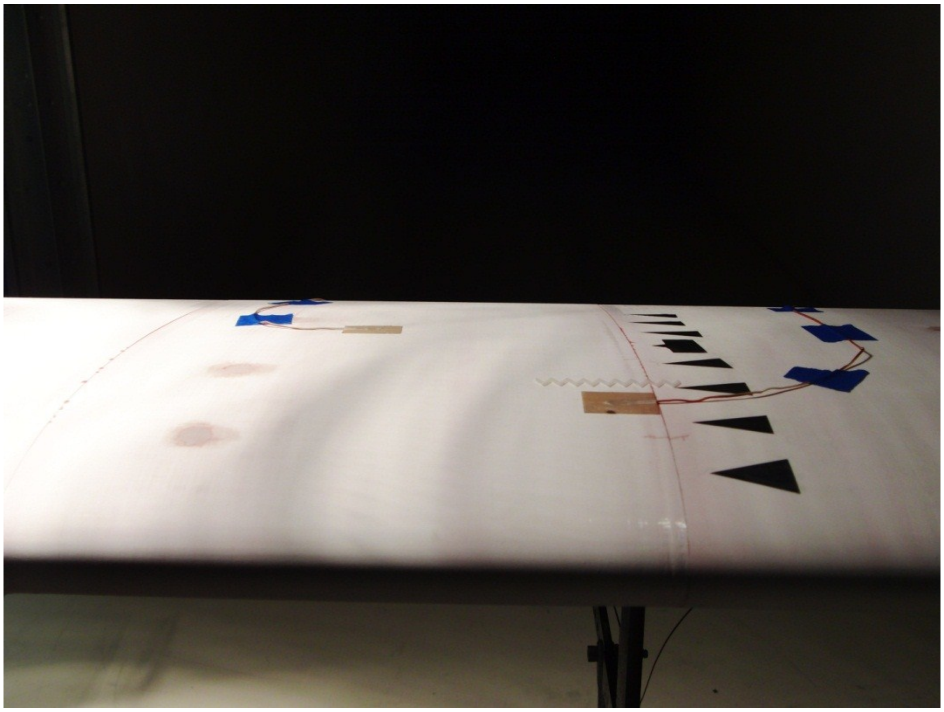

Figure 31 Sanded RP plastic test model

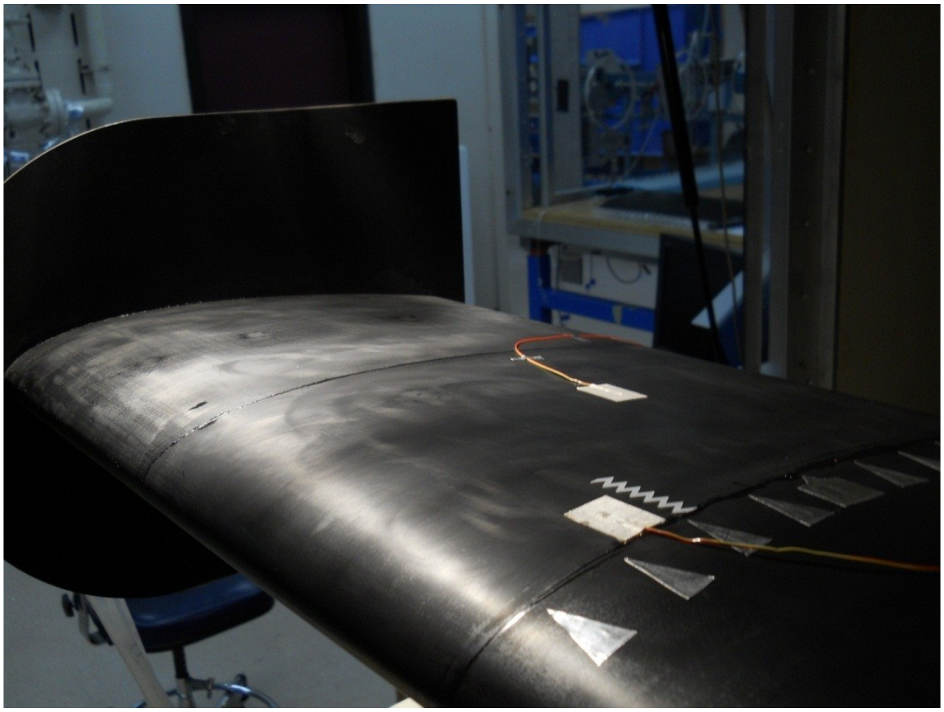

Figure 32 Painted RP plastic test model

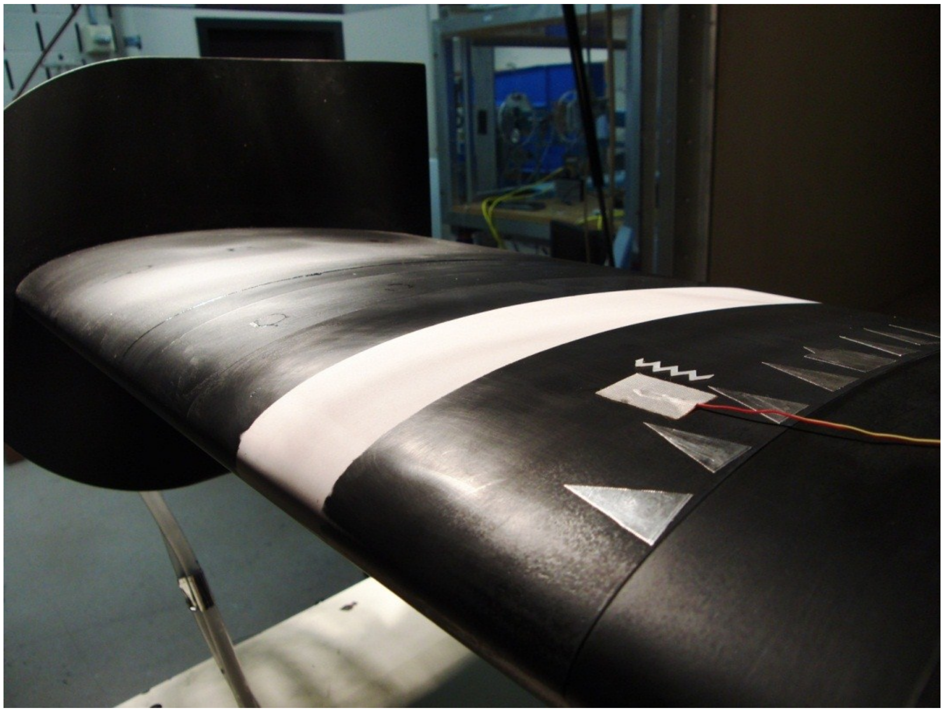

Figure 33 Painted RP plastic test model with a layer of Bondo. A strip of the Bondo has been left unpainted.

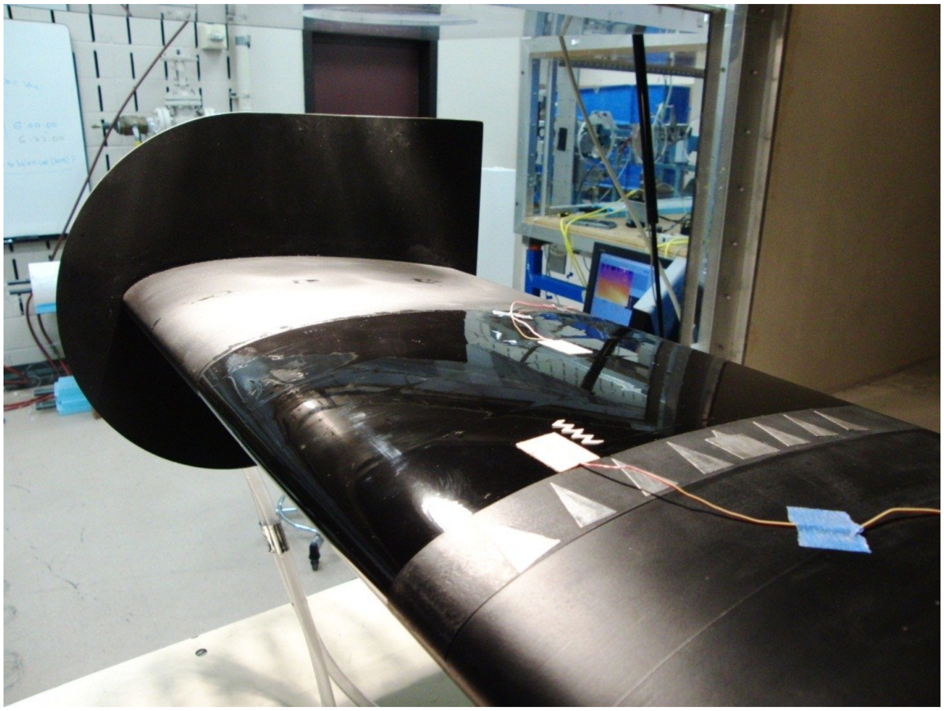

Figure 34 Painted RP plastic test model with Monokote over the layer of Bondo

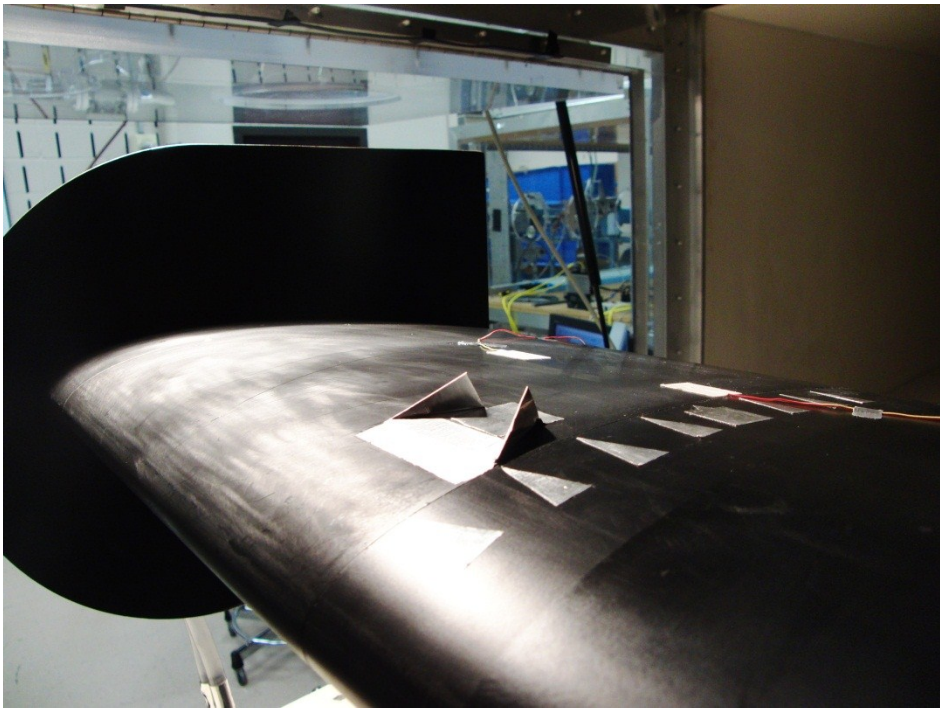

Figure 35 Aluminum with painted adhesive wrap and large VG

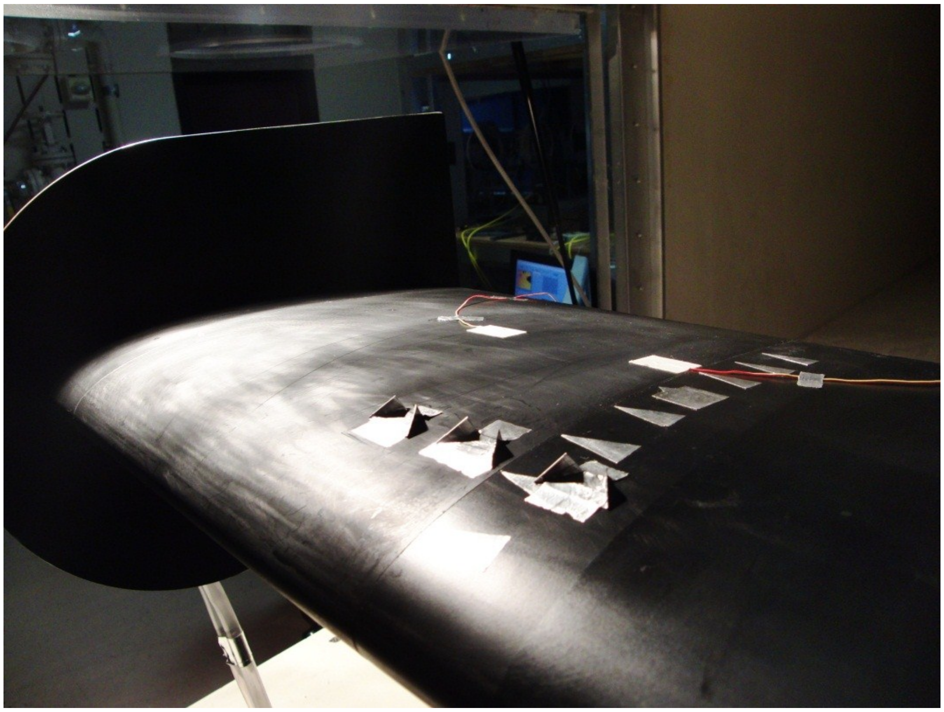

Figure 36 Aluminum with painted adhesive wrap and small VGs

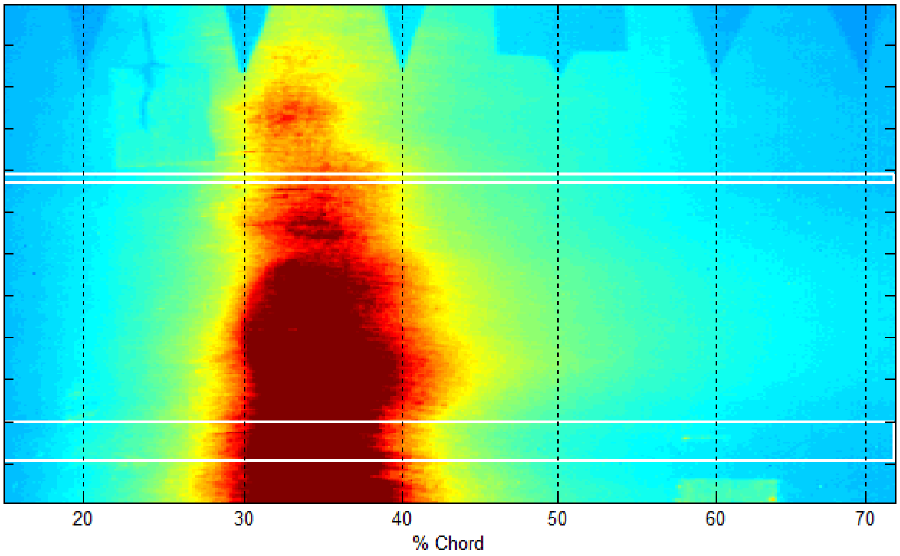

Figure 37 IR image of polished aluminum under the heat lamp
AoA = 0° and $Re_c = 6.6\times10^5$

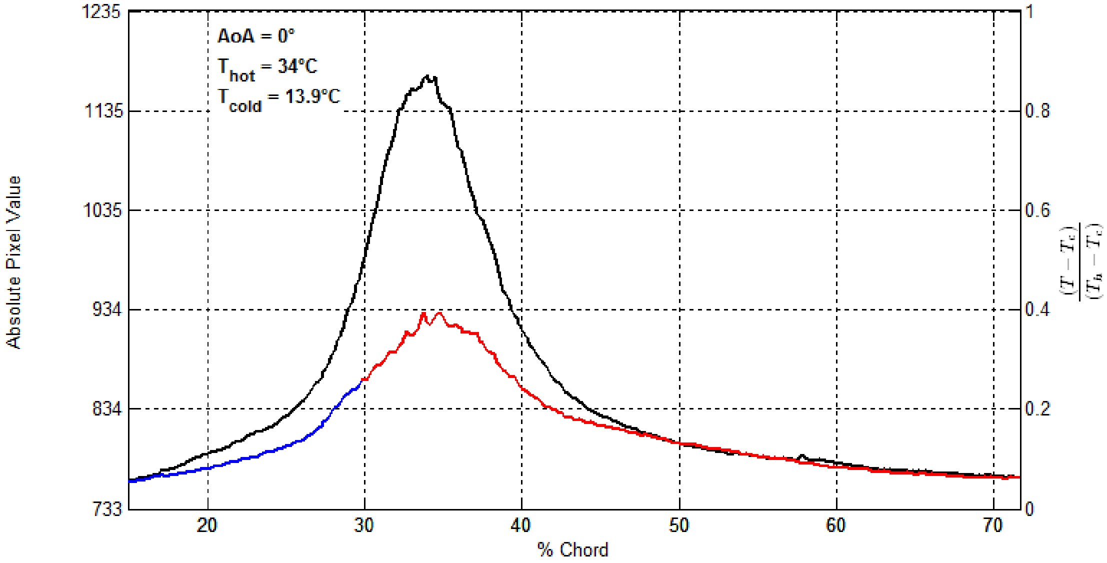

Figure 38 Surface temperature profile of Figure 37

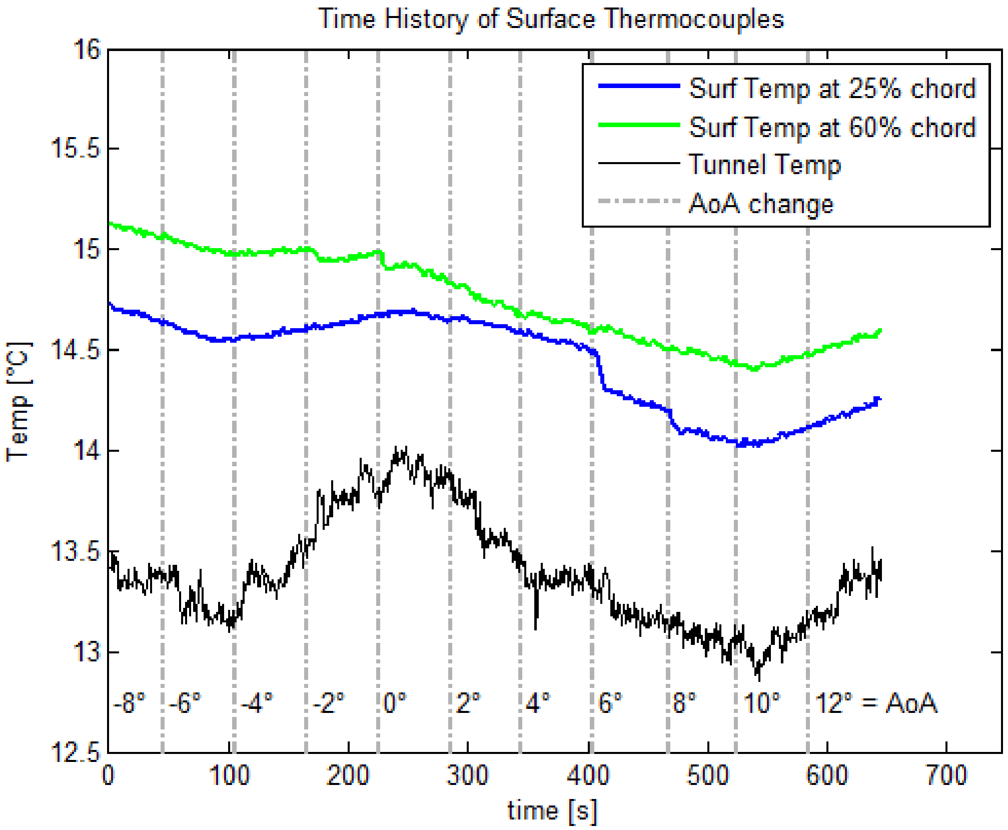

Figure 39 Time history of tunnel and surface temperatures for entire run corresponding to Figure 37

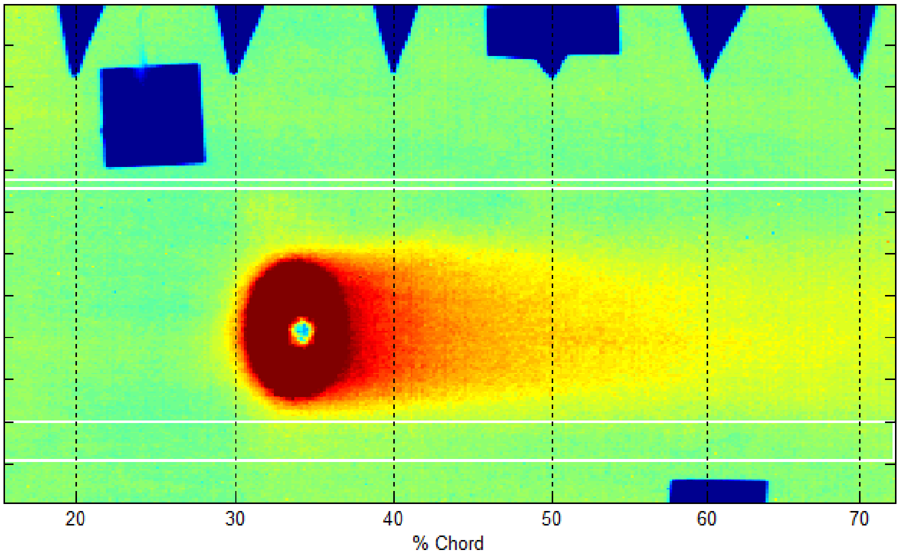

Figure 40 IR image of polished aluminum with ice water circulation AoA = 0° and $Re_c = 6.6\times10^5$

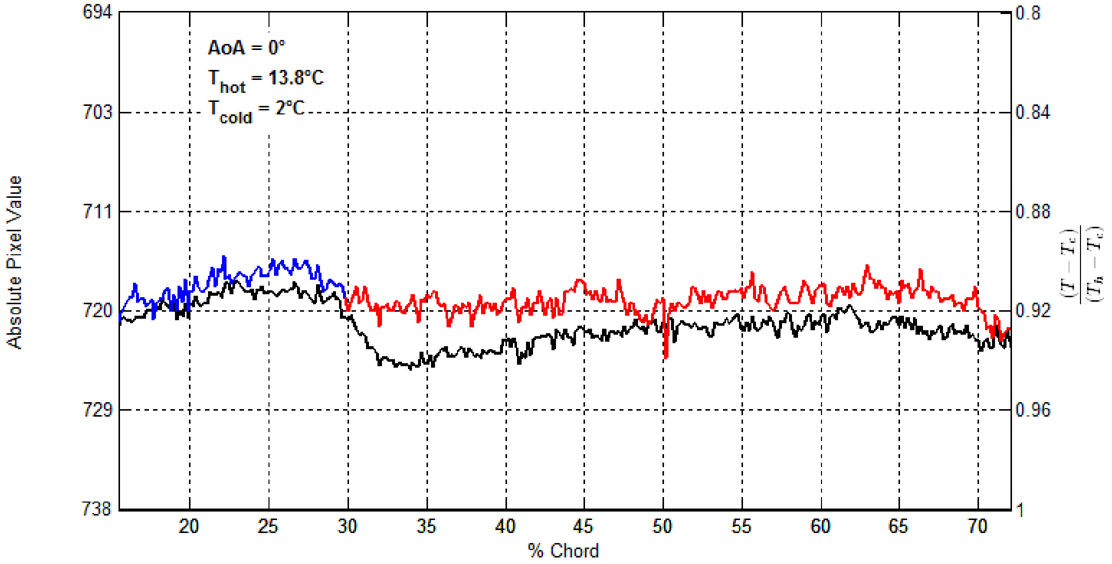

Figure 41 Surface temperature profile of Figure 40

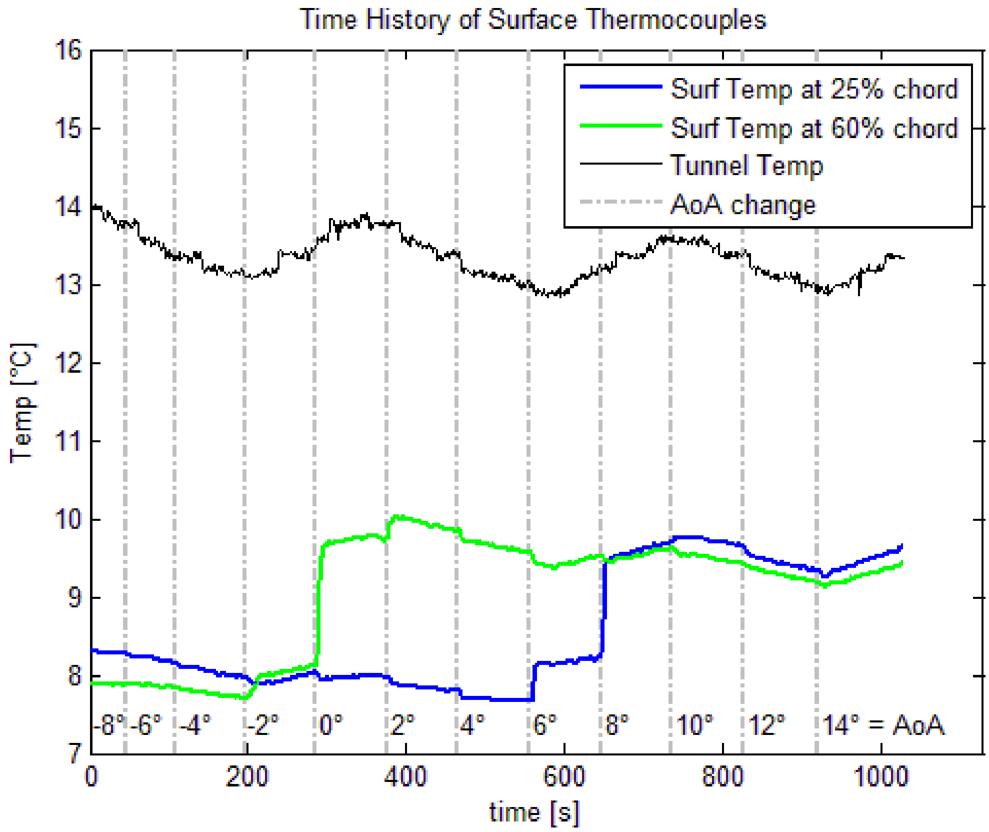

Figure 42 Time history of tunnel and surface temperatures for entire run corresponding to Figure 40

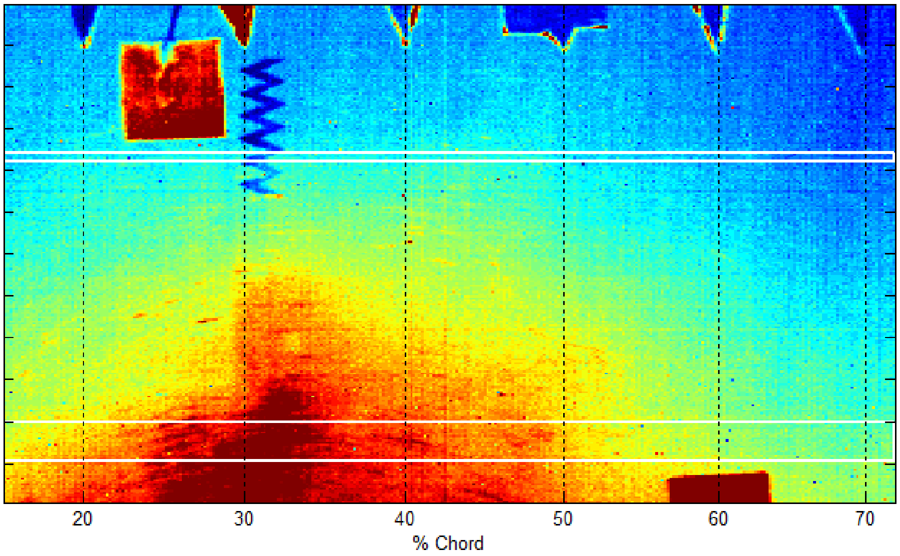

Figure 43 IR image of painted aluminum using the heat lamp
AoA = 0° and $Re_c = 6.6 \times 10^5$

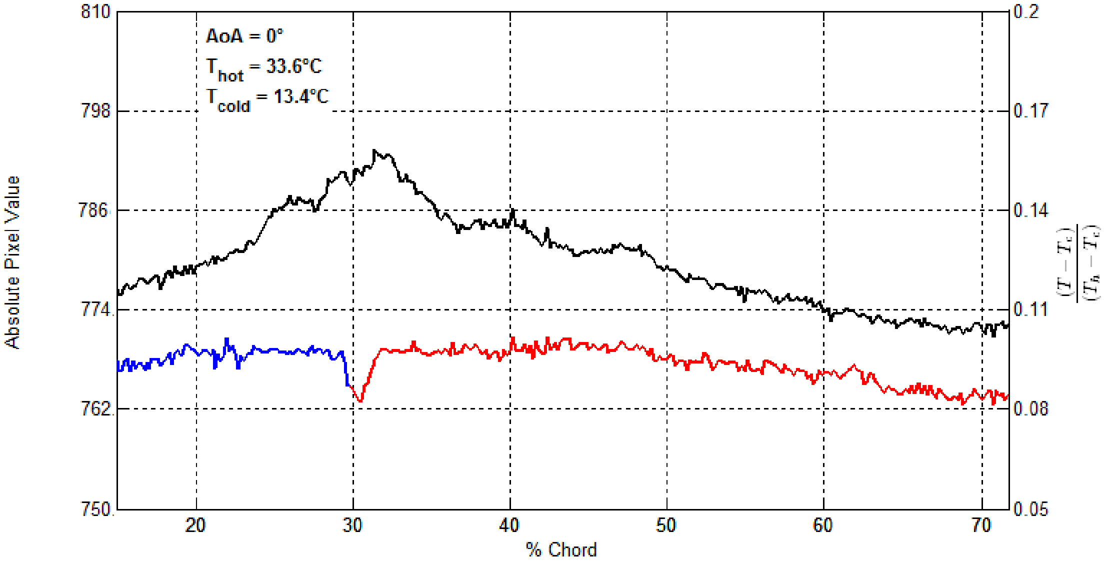

Figure 44 Surface temperature profile of Figure 43

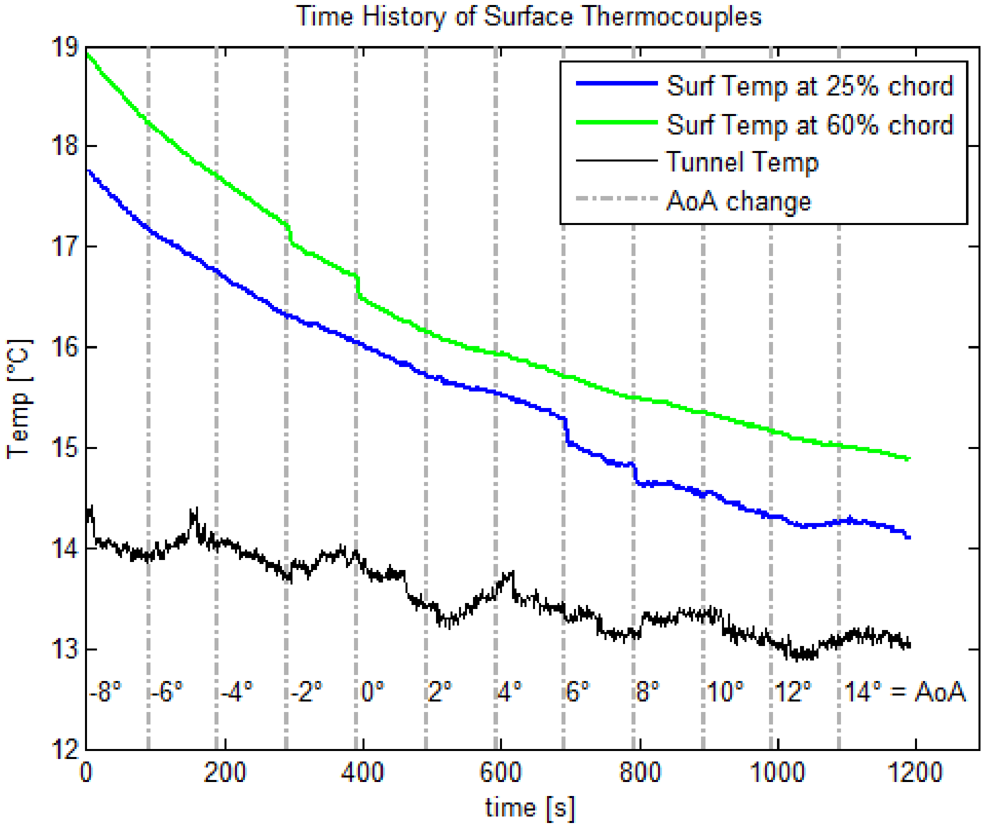

Figure 45 Time history of tunnel and surface temperatures for entire run corresponding to Figure 43

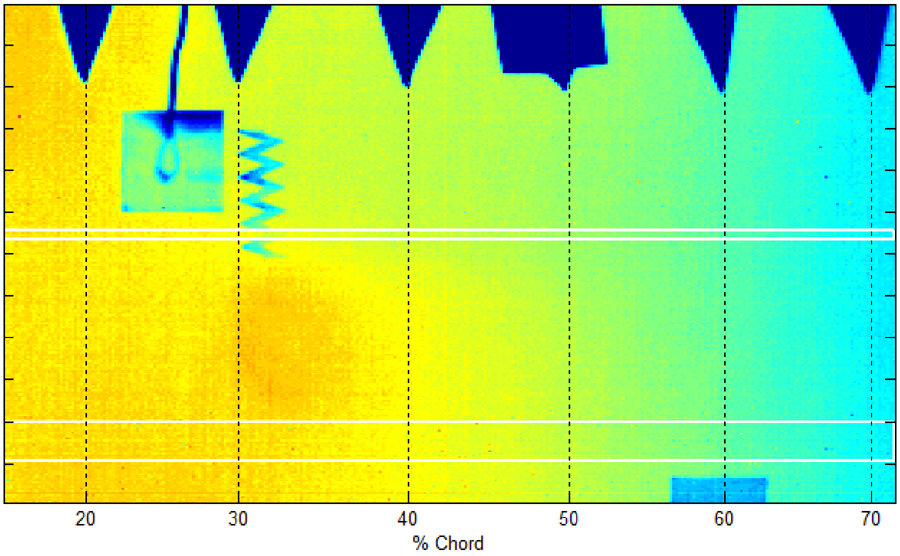

Figure 46 IR image of painted aluminum using tap water circulation AoA = 0° and $Re_c = 6.6\times10^5$

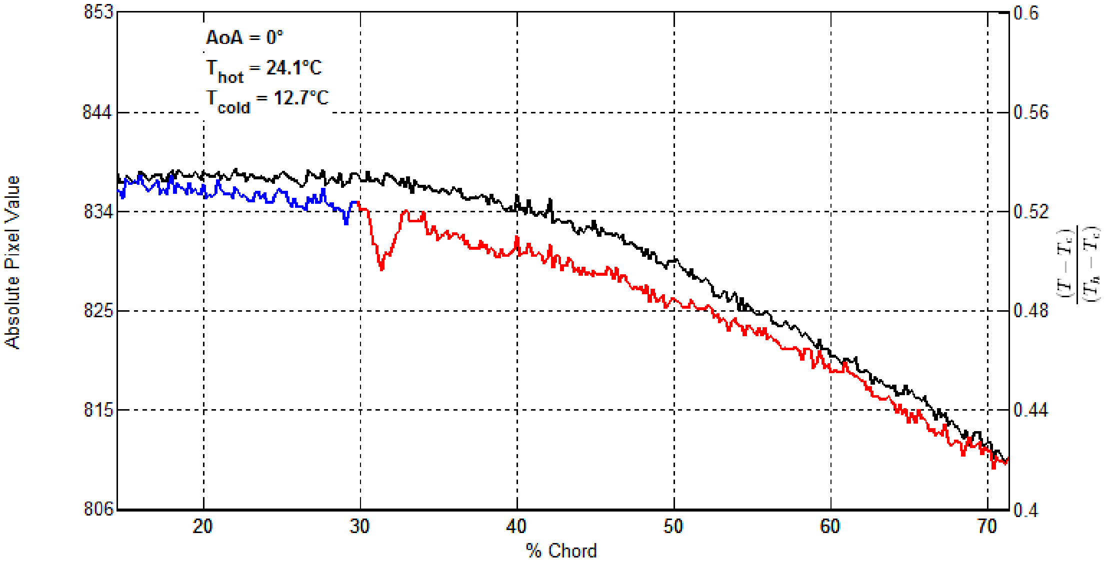

Figure 47 Surface temperature profile of Figure 46

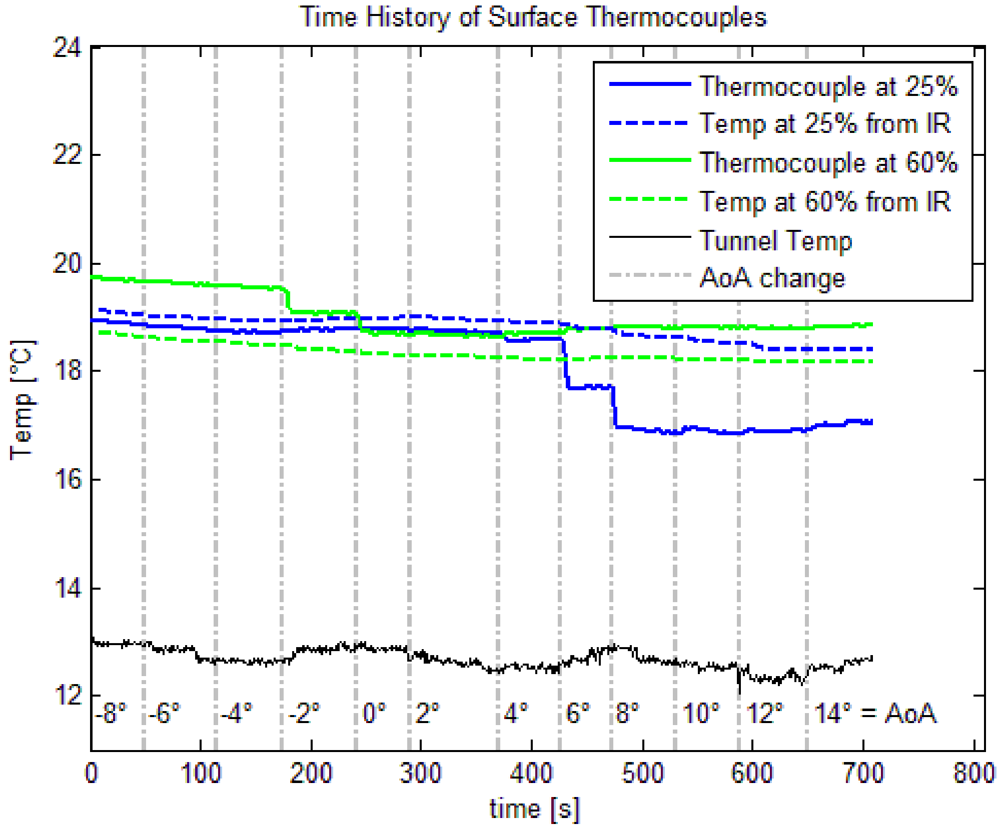

Figure 48 Time history of tunnel and surface temperatures from both the surface thermocouples and the IR camera for entire run corresponding to Figure 46

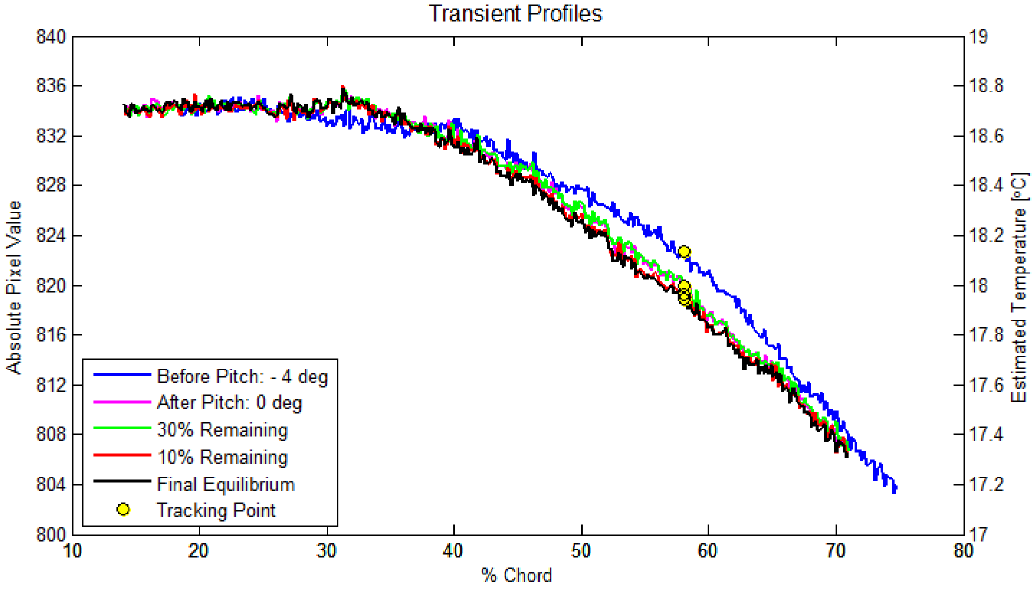

Figure 49 Temperature profiles throughout transient response as the model is pitched from AoA = -4° to 0°; configuration corresponds to Figure 46

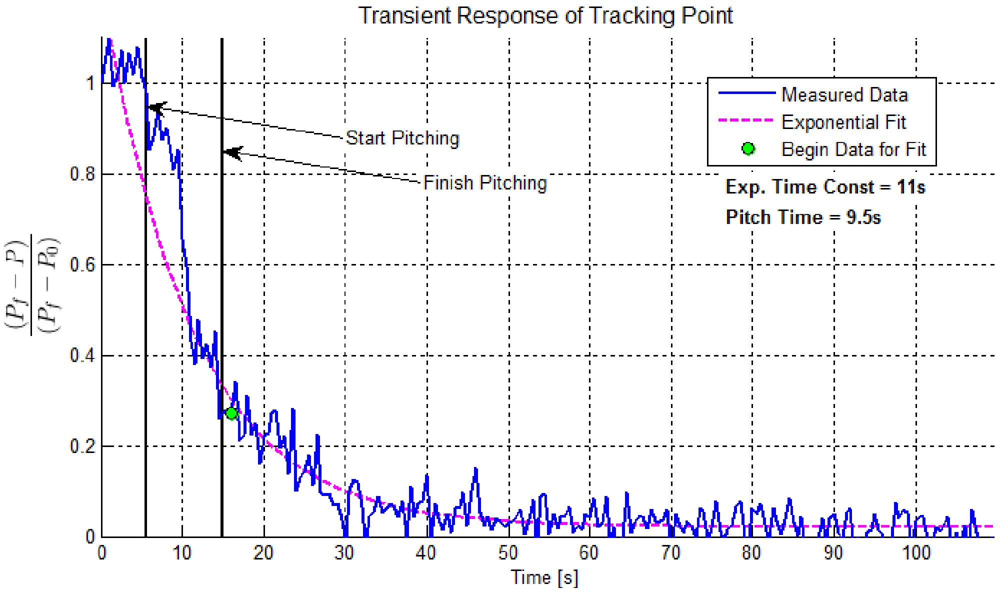

Figure 50 Response of tracking point shown in Figure 49 as a yellow circle Data is fit to an exponential decay function

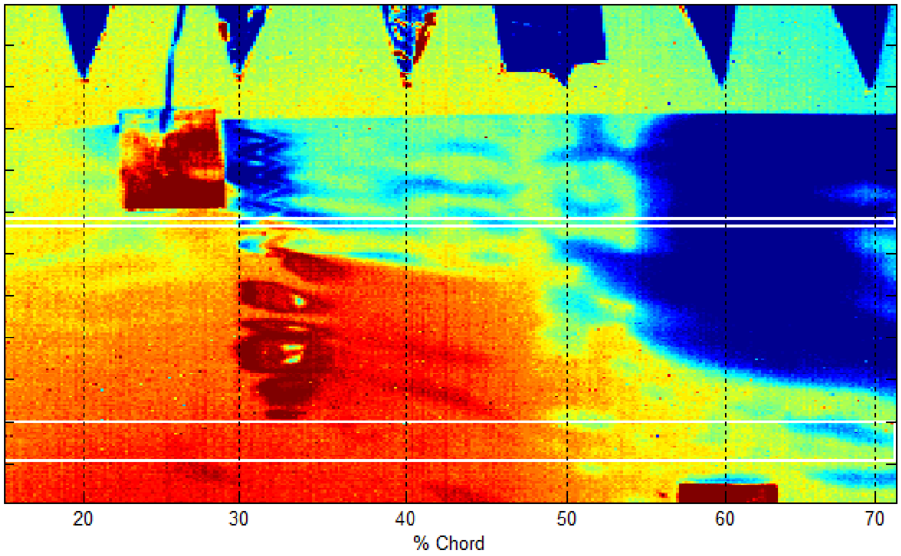

Figure 51 IR image of painted aluminum wrapped in Monokote under the heat lamp AoA = 0° and $Re_c = 6.6 \times 10^5$

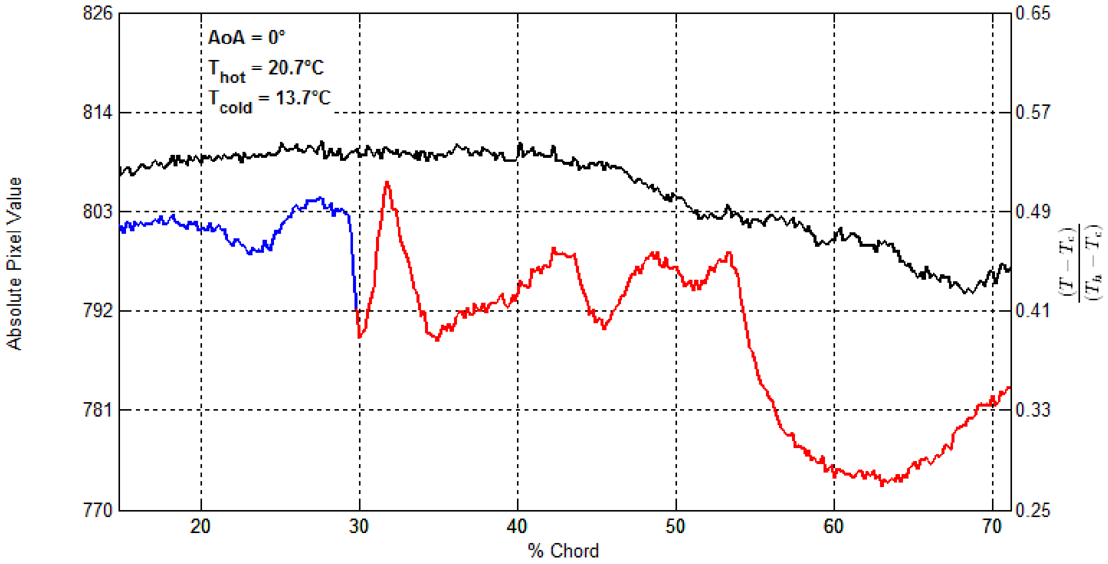

Figure 52 Surface temperature profile of Figure 51

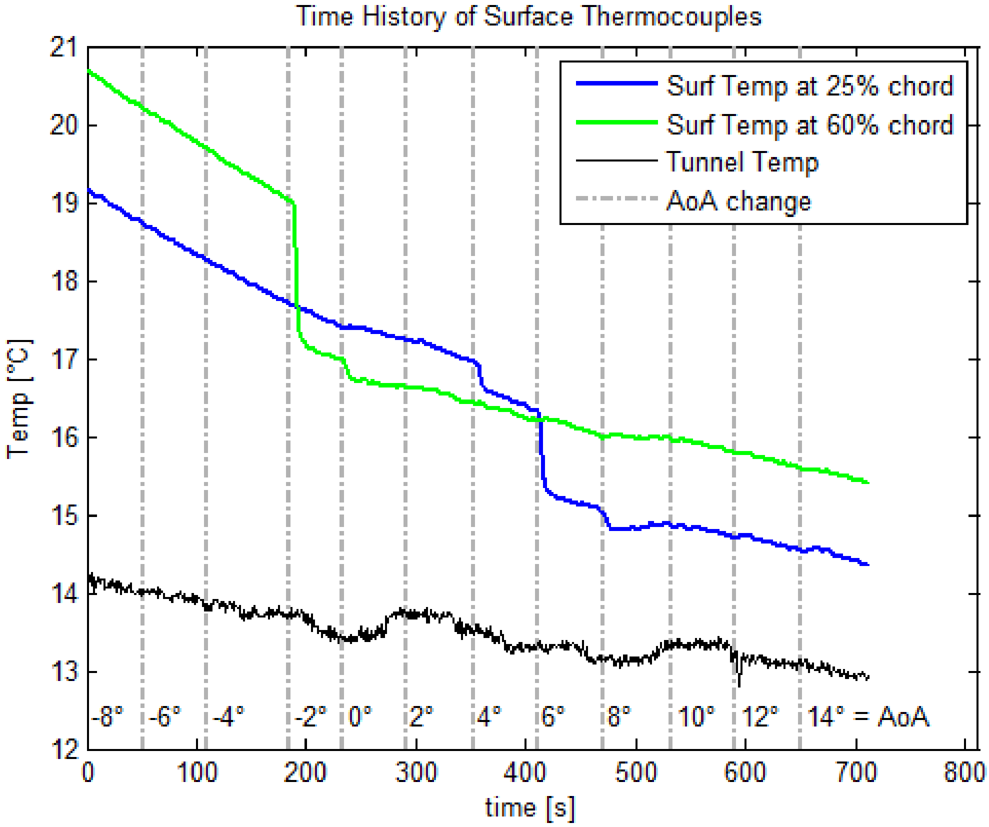

Figure 53 Time history of tunnel and surface temperatures for entire run corresponding to Figure 51

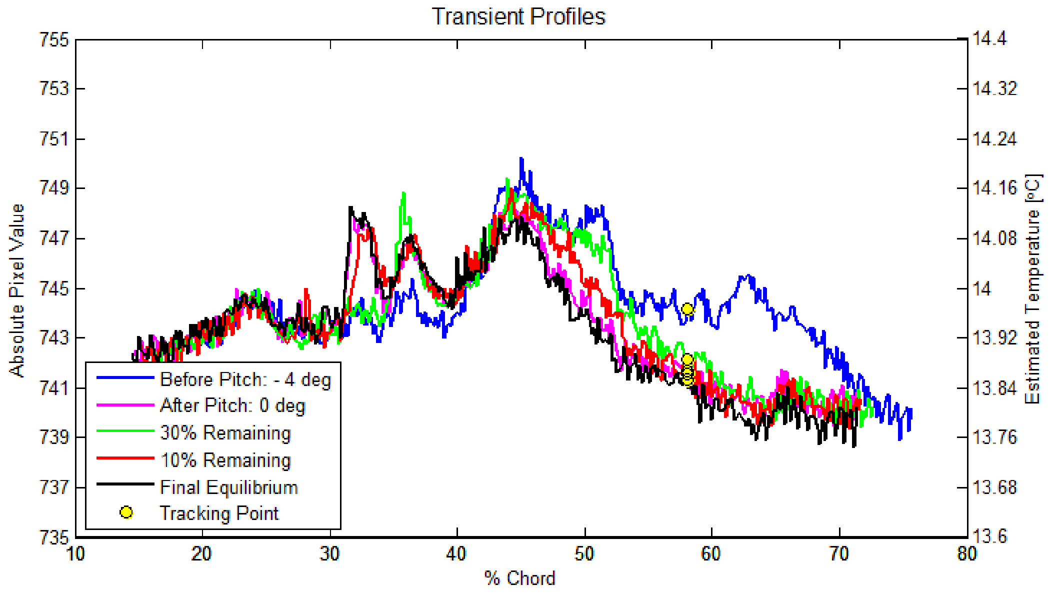

Figure 54 Temperature profiles throughout transient response as the model is pitched from AoA = -4° to 0°; configuration corresponds to Figure 51

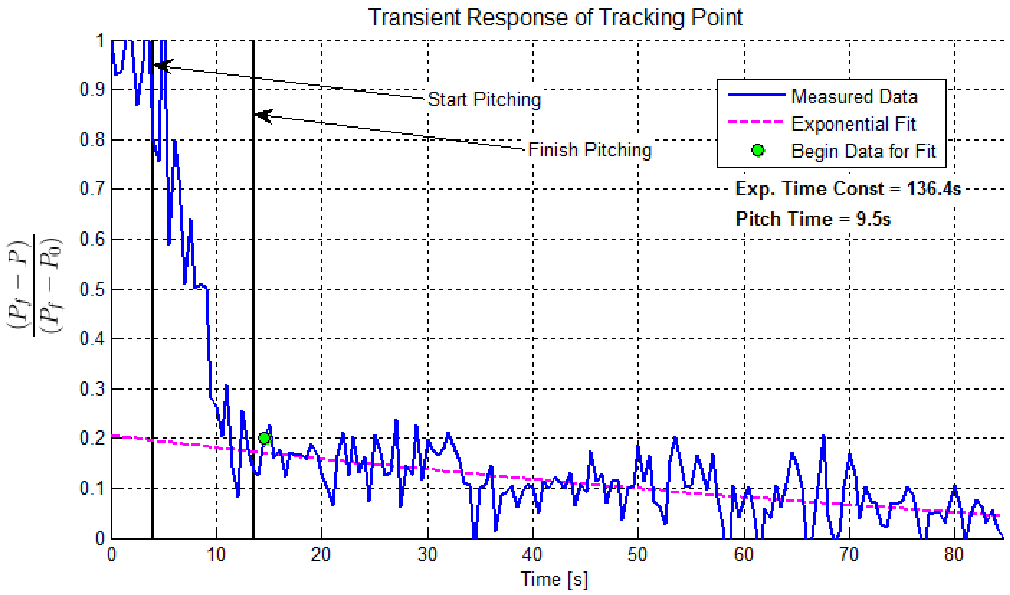

Figure 55 Response of tracking point shown in Figure 54 as a yellow circle Data is fit to an exponential decay function

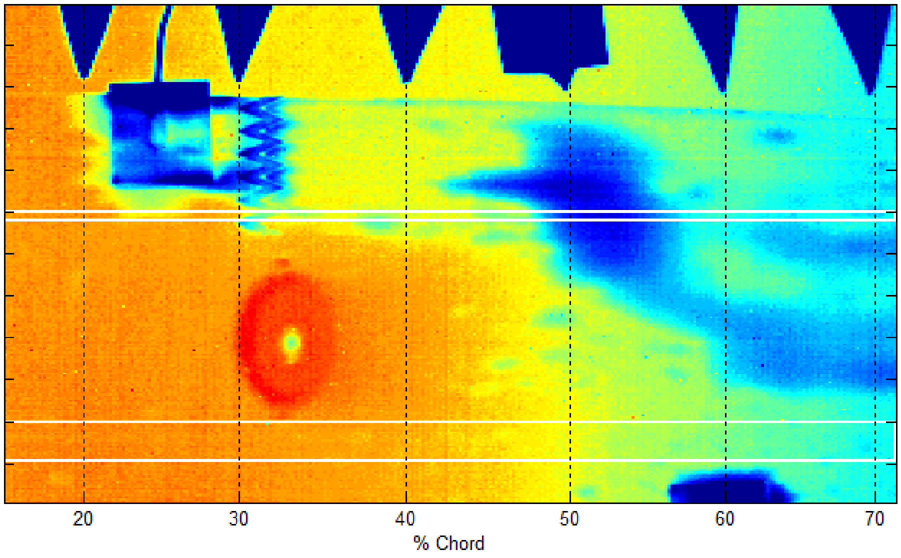

Figure 56 IR image of painted aluminum wrapped in Monokote and using tap water circulation; AoA = 0° and $Re_c = 6.6\times10^5$

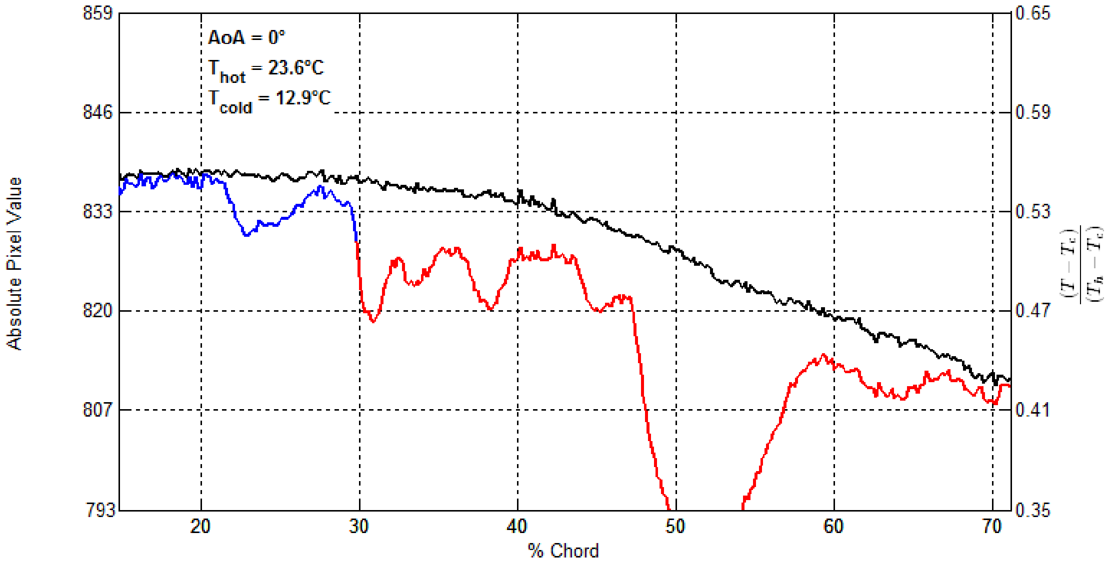

Figure 57 Surface temperature profile of Figure 56

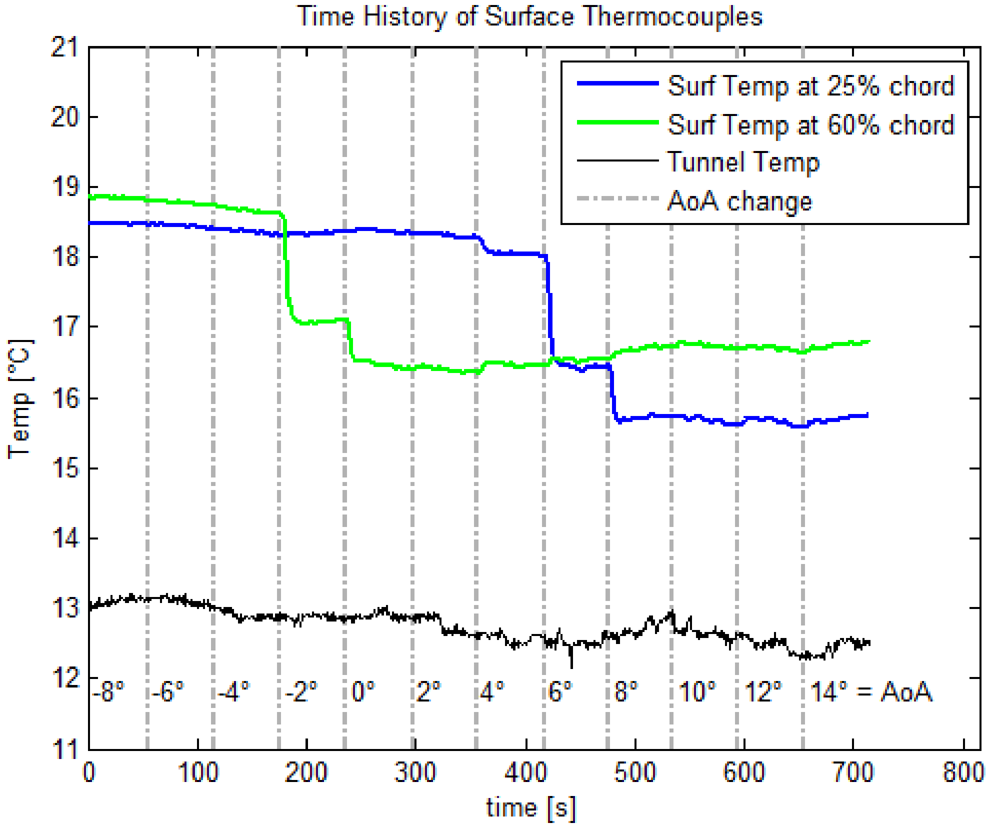

Figure 58 Time history of tunnel and surface temperatures for entire run corresponding to Figure 56

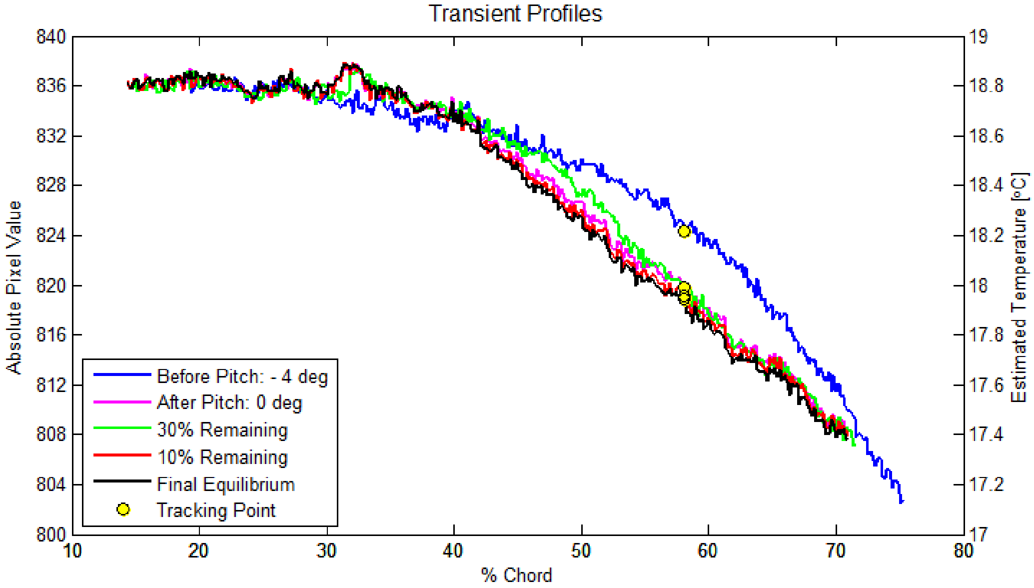

Figure 59 Temperature profiles throughout transient response as the model is pitched from AoA = -4° to 0°; configuration corresponds to Figure 56

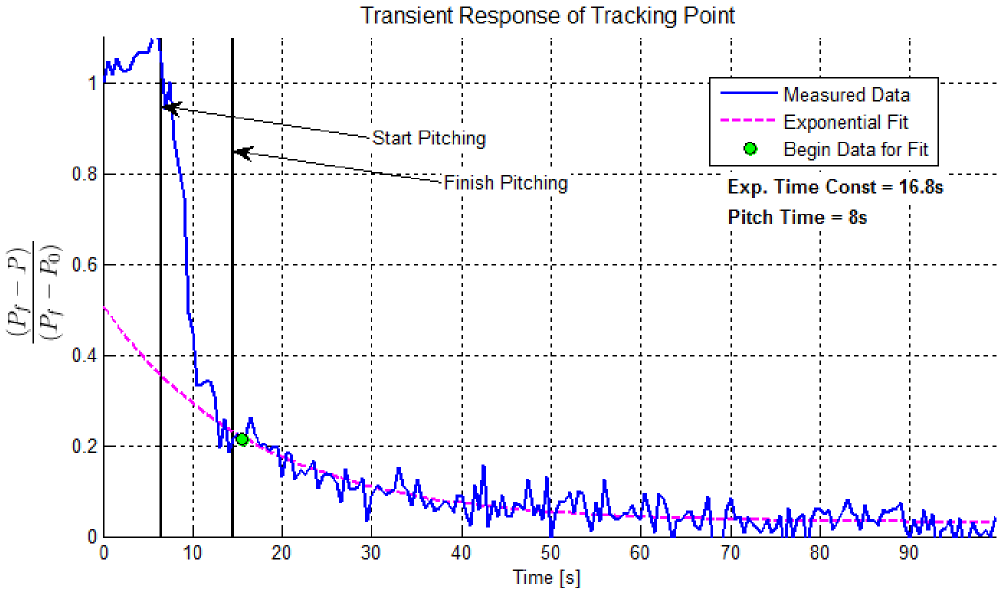

Figure 60 Response of tracking point shown in Figure 59 as a yellow circle Data is fit to an exponential decay function

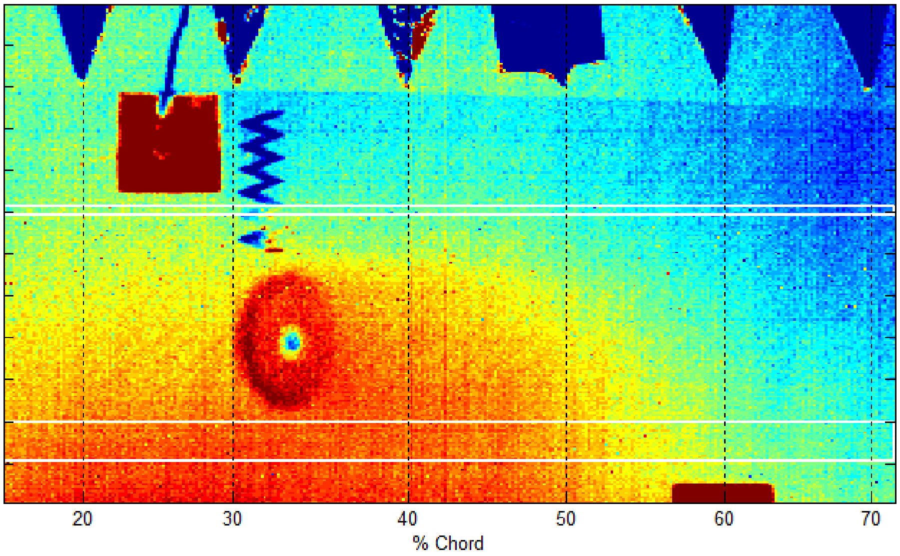

Figure 61 IR image of painted aluminum with clear plastic adhesive wrap using the heat lamp, AoA = 0° and $Re_c = 6.6 \times 10^5$

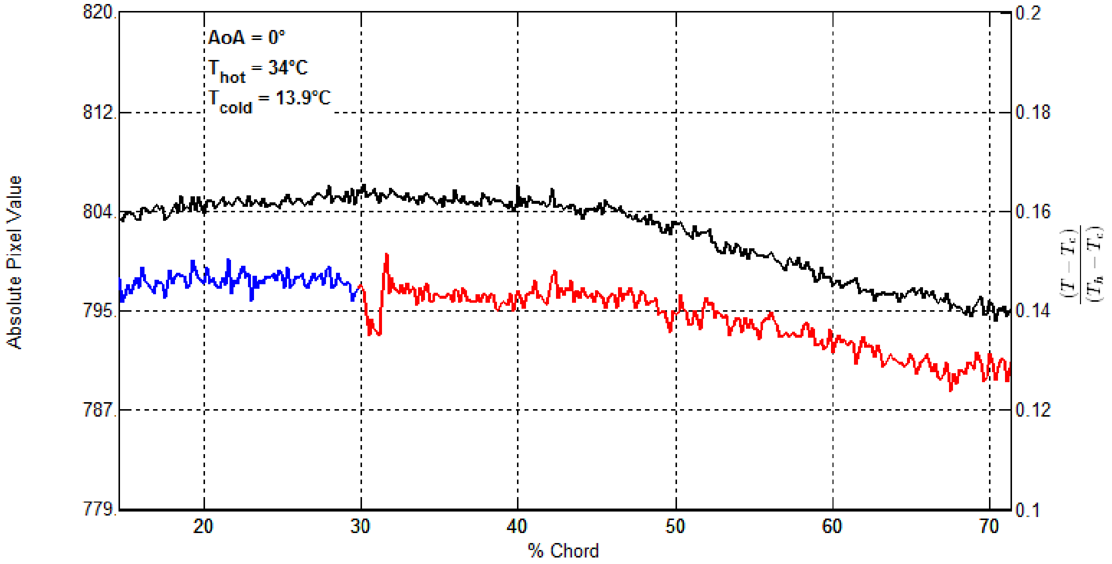

Figure 62 Surface temperature profile of Figure 61

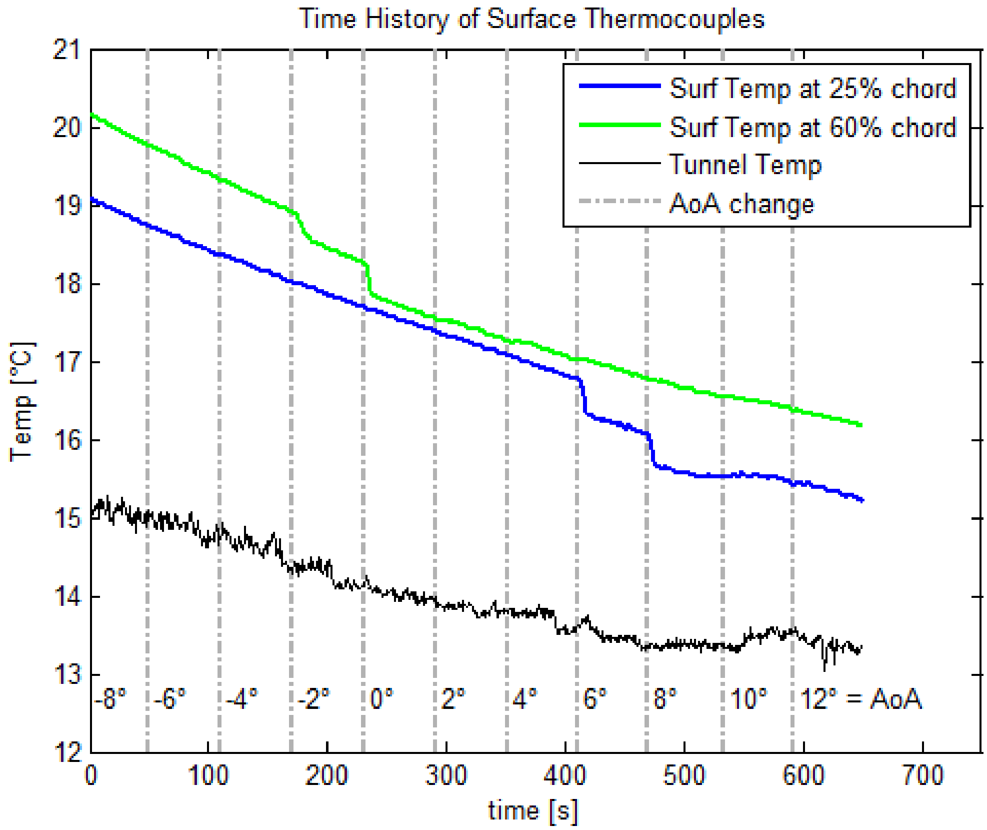

Figure 63 Time history of tunnel and surface temperatures for entire run corresponding to Figure 61

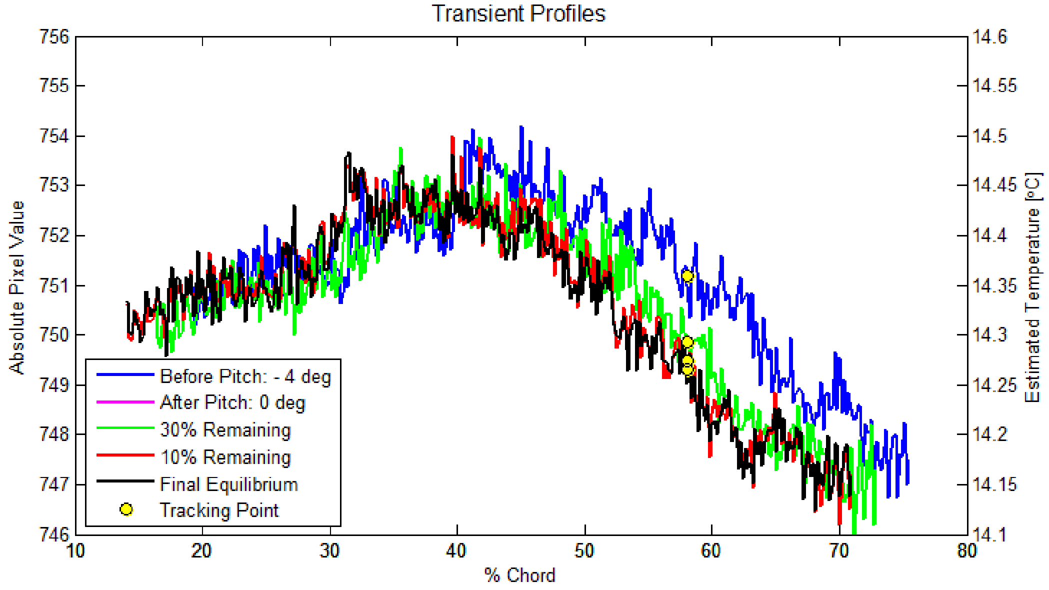

Figure 64 Temperature profiles throughout transient response as the model is pitched from AoA = -4° to 0°; configuration corresponds to Figure 61

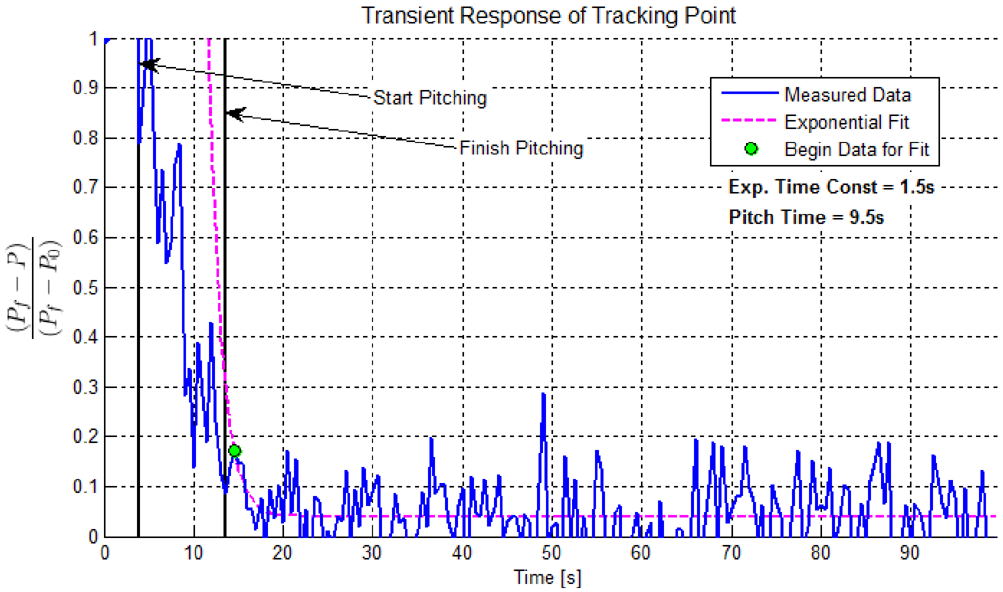

Figure 65 Response of tracking point shown in Figure 64 as a yellow circle Data is fit to an exponential decay function

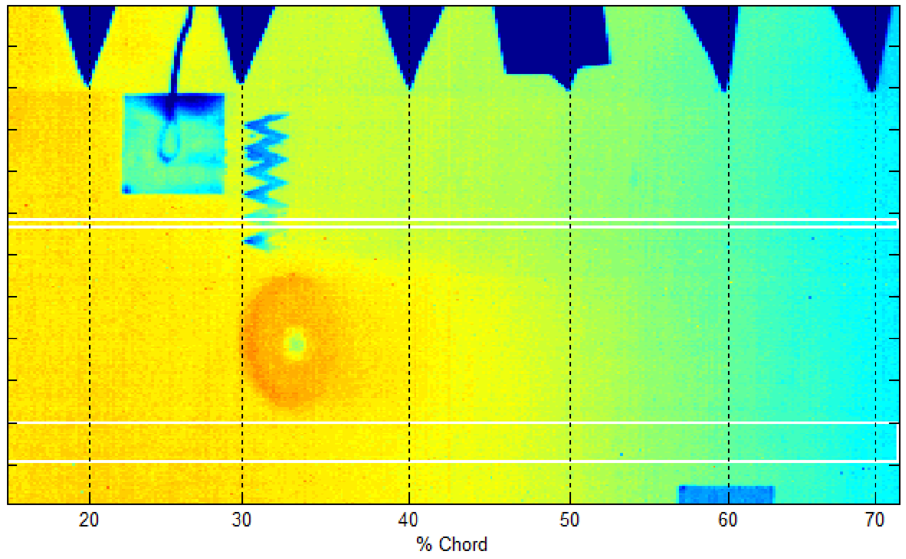

Figure 66 IR image of painted aluminum with clear plastic adhesive wrap using tap water circulation, AoA = 0° and $Re_c = 6.6\times10^5$

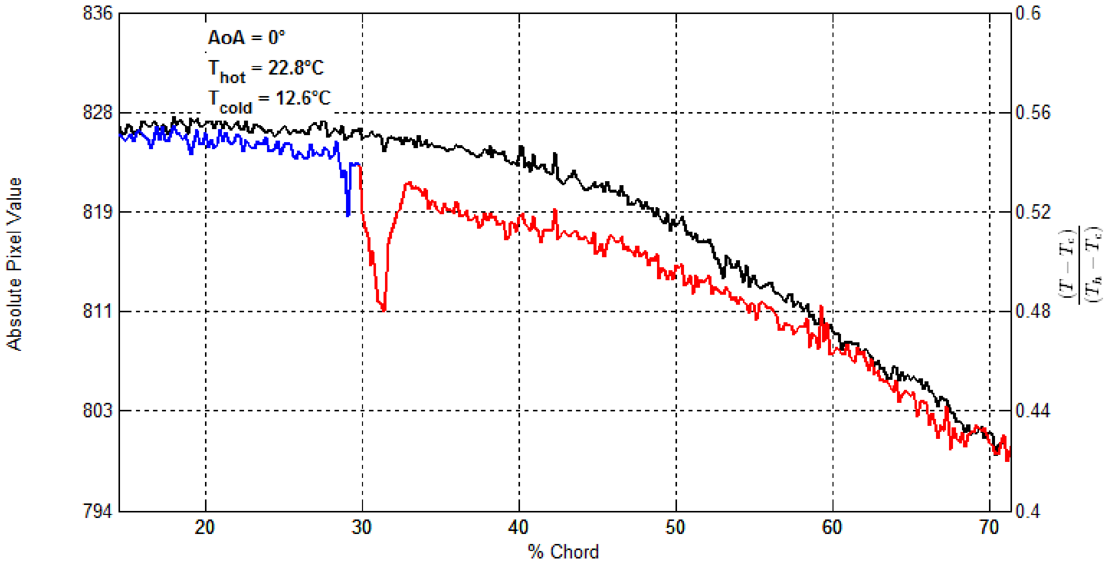

Figure 67 Surface temperature profile of Figure 66

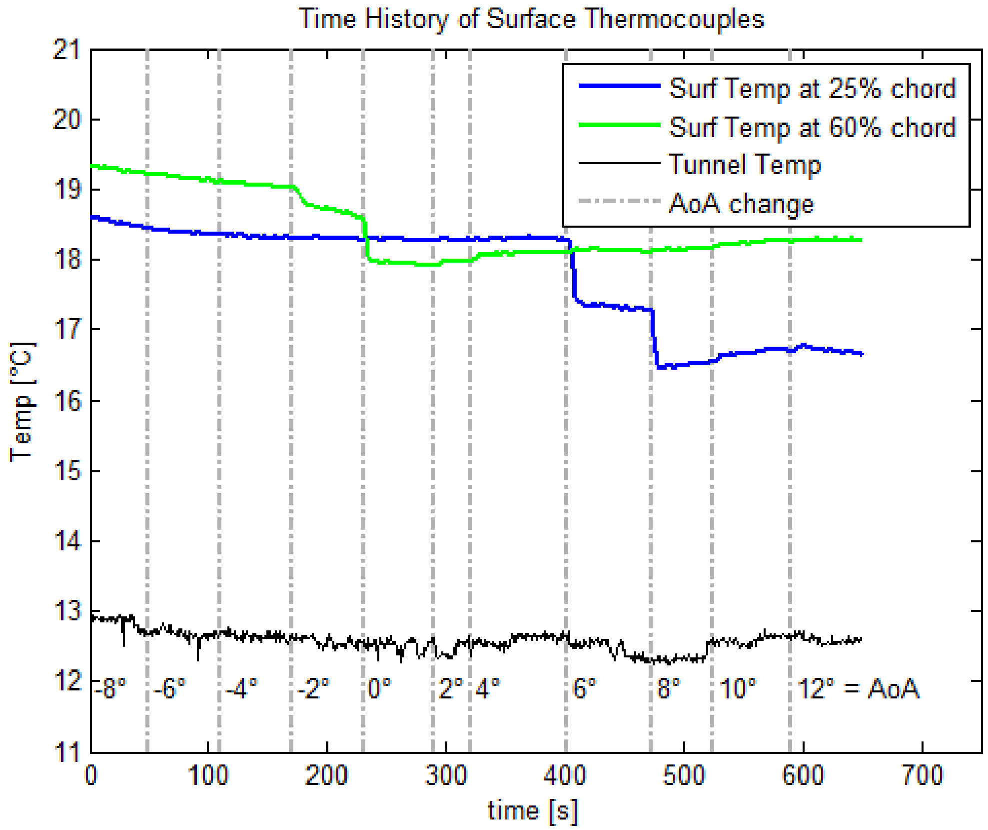

Figure 68 Time history of tunnel and surface temperatures for entire run corresponding to Figure 66

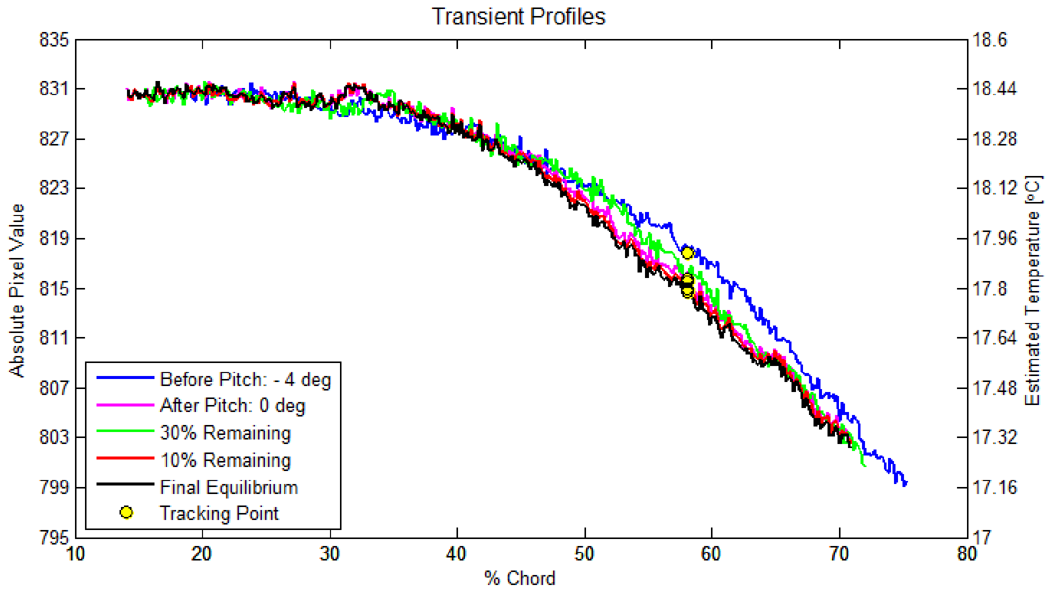

Figure 69 Temperature profiles throughout transient response as the model is pitched from AoA = -4° to 0°; configuration corresponds to Figure 66

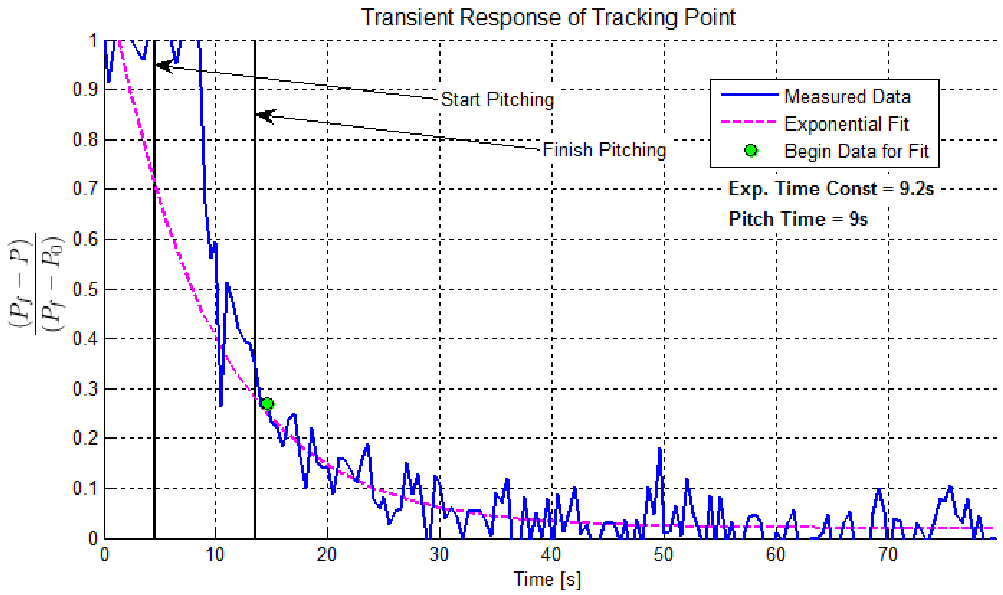

Figure 70 Response of tracking point shown in Figure 69 as a yellow circle Data is fit to an exponential decay function

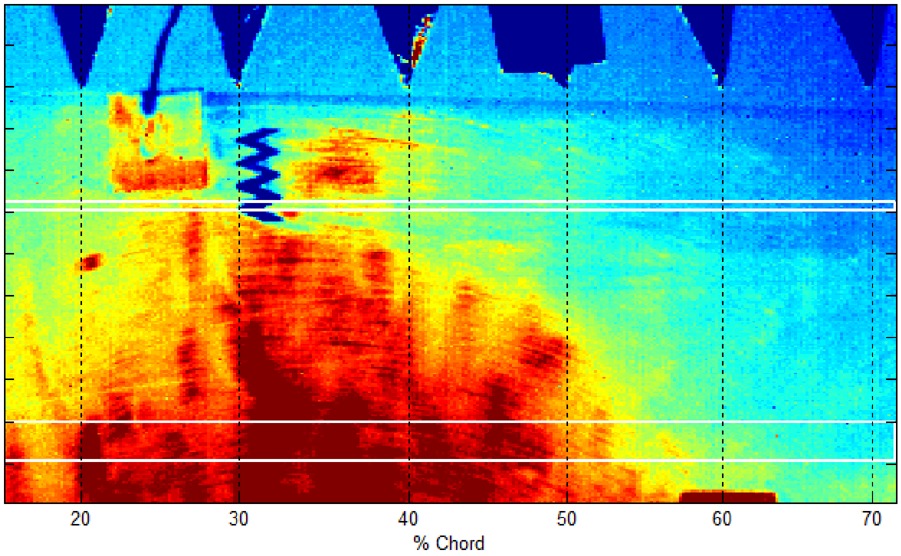

Figure 71 IR image of painted aluminum with painted plastic adhesive wrap under the heat lamp, AoA = 0° and $Re_c = 6.6 \times 10^5$

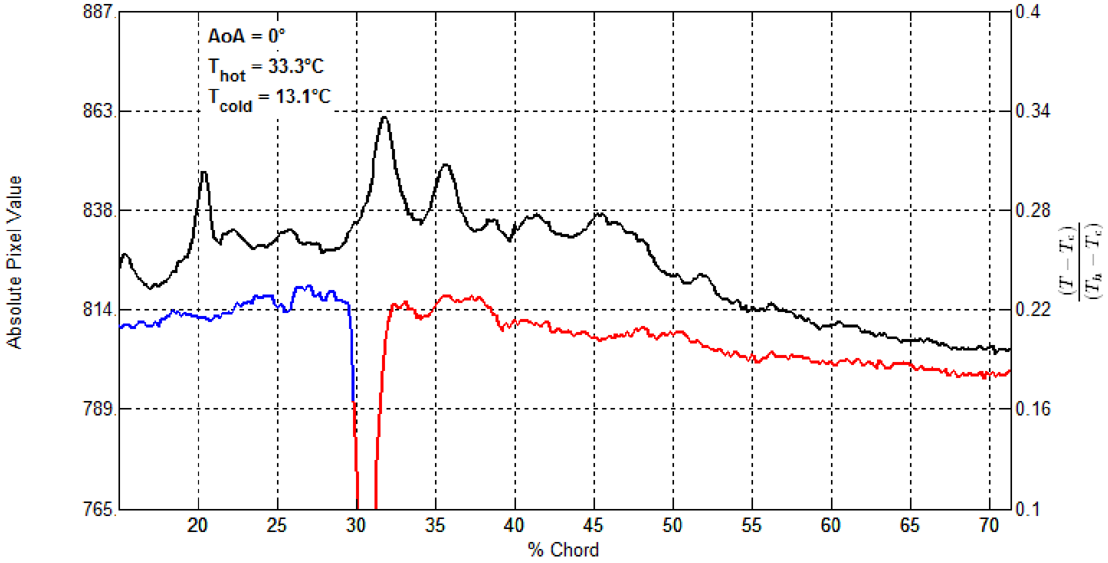

Figure 72 Surface temperature profile of Figure 71

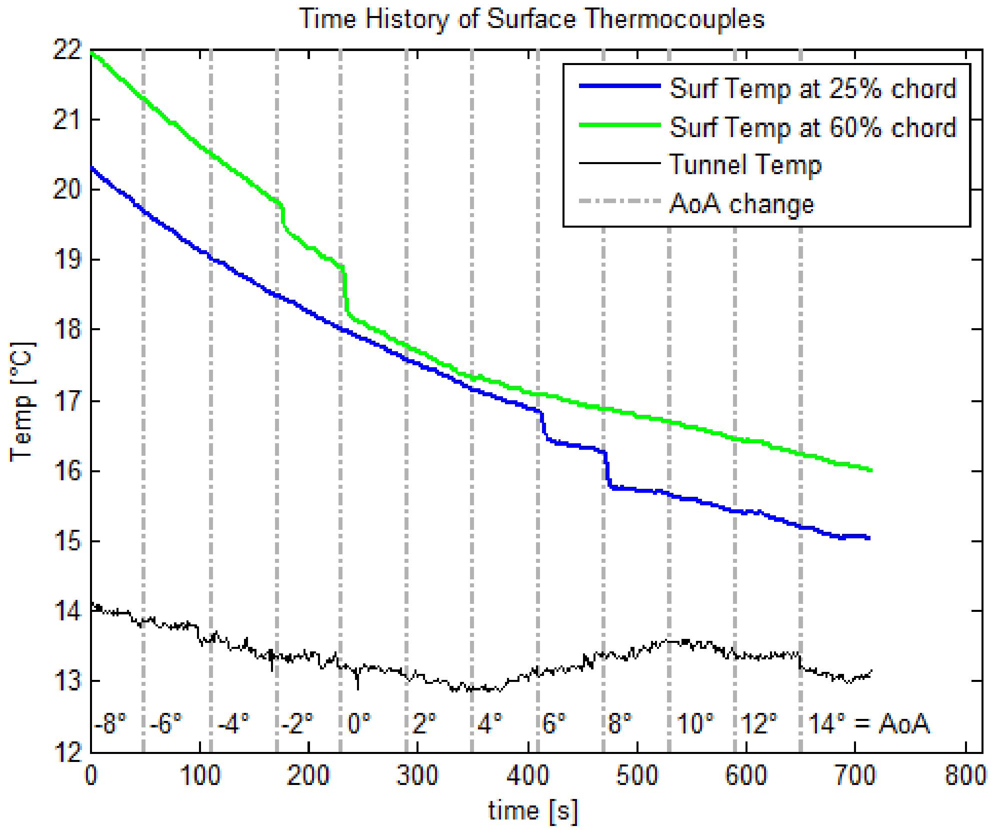

Figure 73 Time history of tunnel and surface temperatures for entire run corresponding to Figure 71

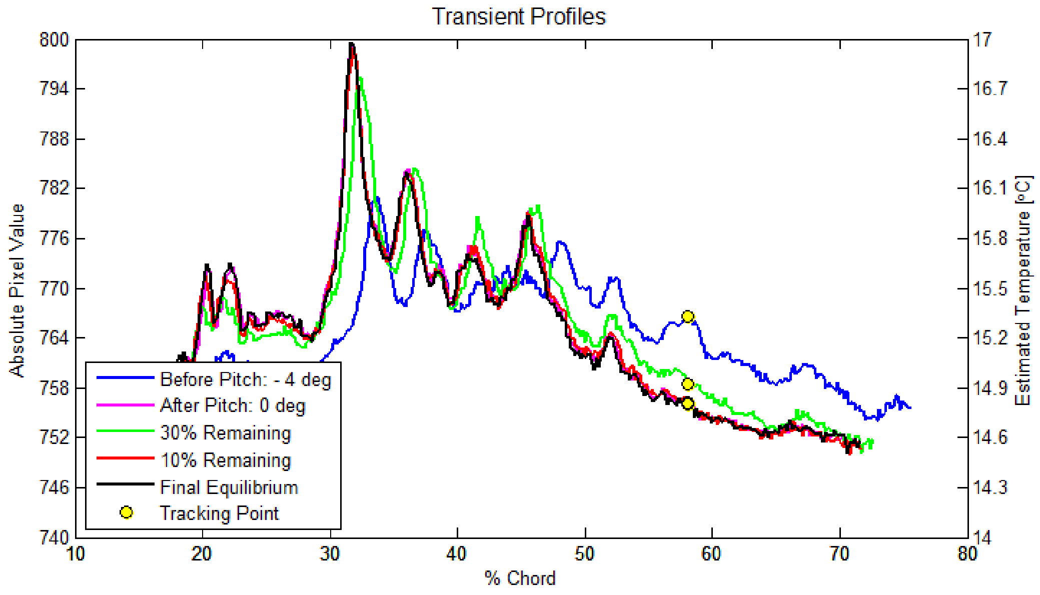

Figure 74 Temperature profiles throughout transient response as the model is pitched from AoA = -4° to 0°; configuration corresponds to Figure 71

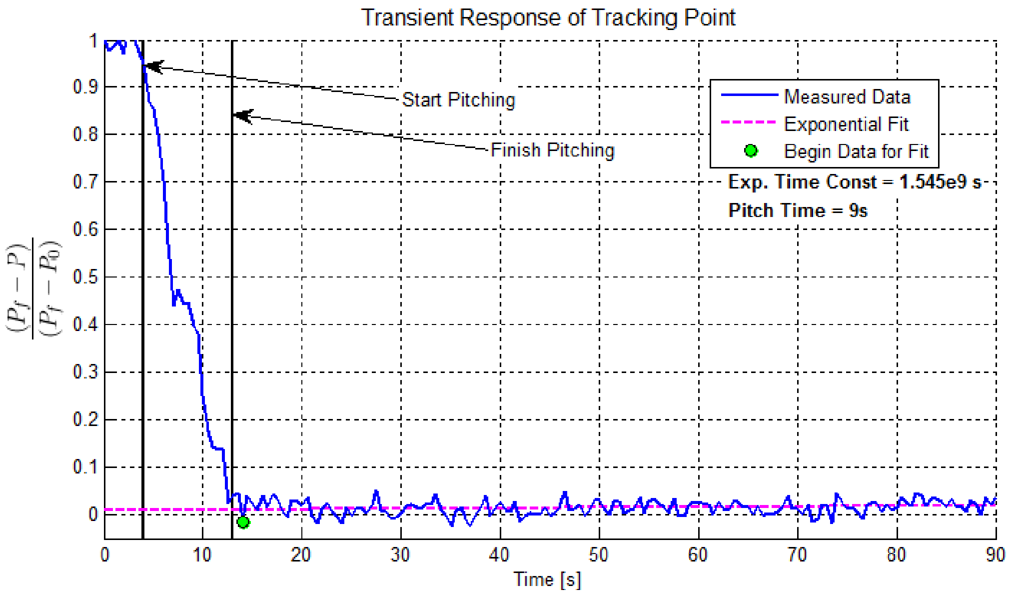

Figure 75 Response of tracking point shown in Figure 74 as a yellow circle Data is fit to an exponential decay function

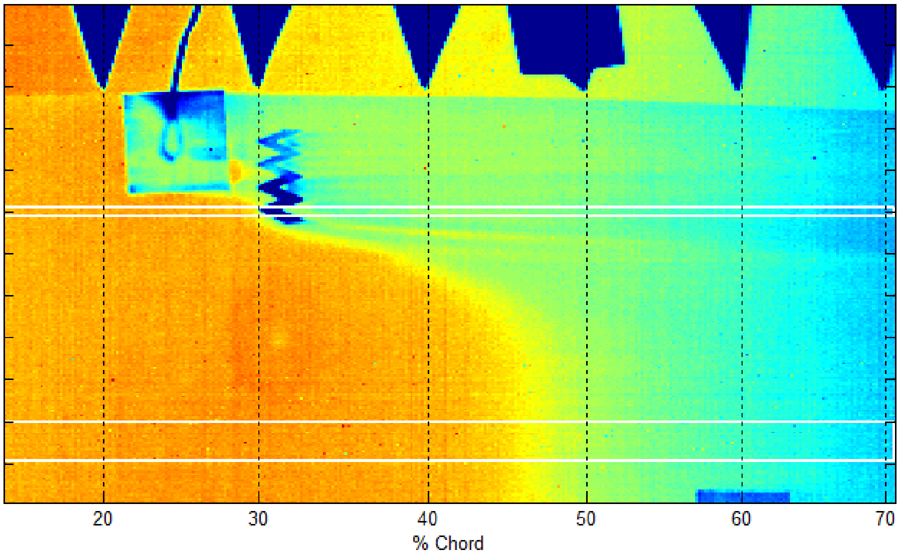

Figure 76 IR image of painted aluminum with painted plastic adhesive wrap using tap water circulation, AoA = 0° and $Re_c = 6.6\times10^5$

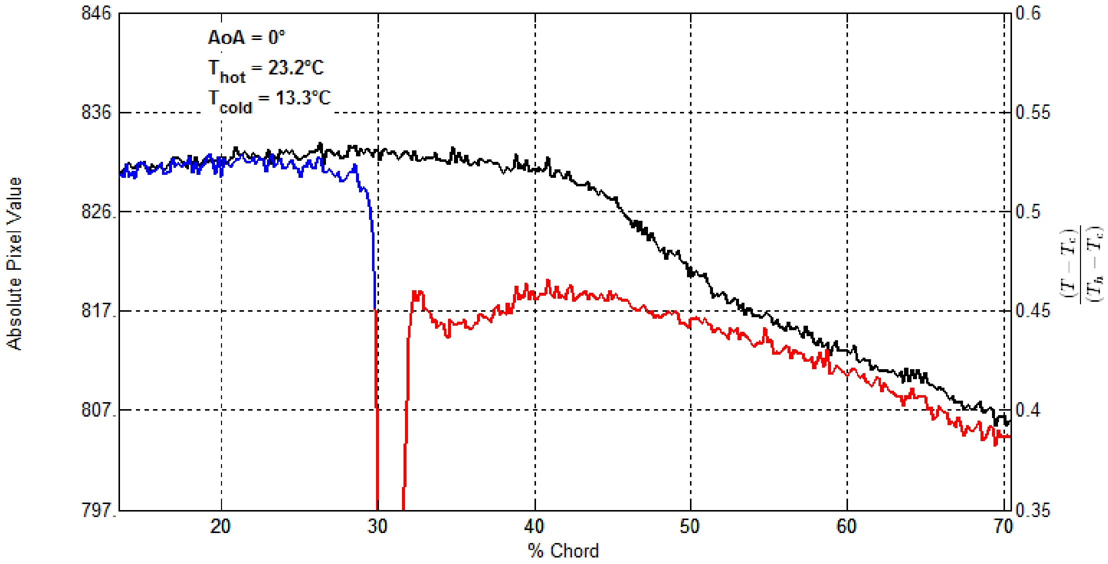

Figure 77 Surface temperature profile of Figure 76

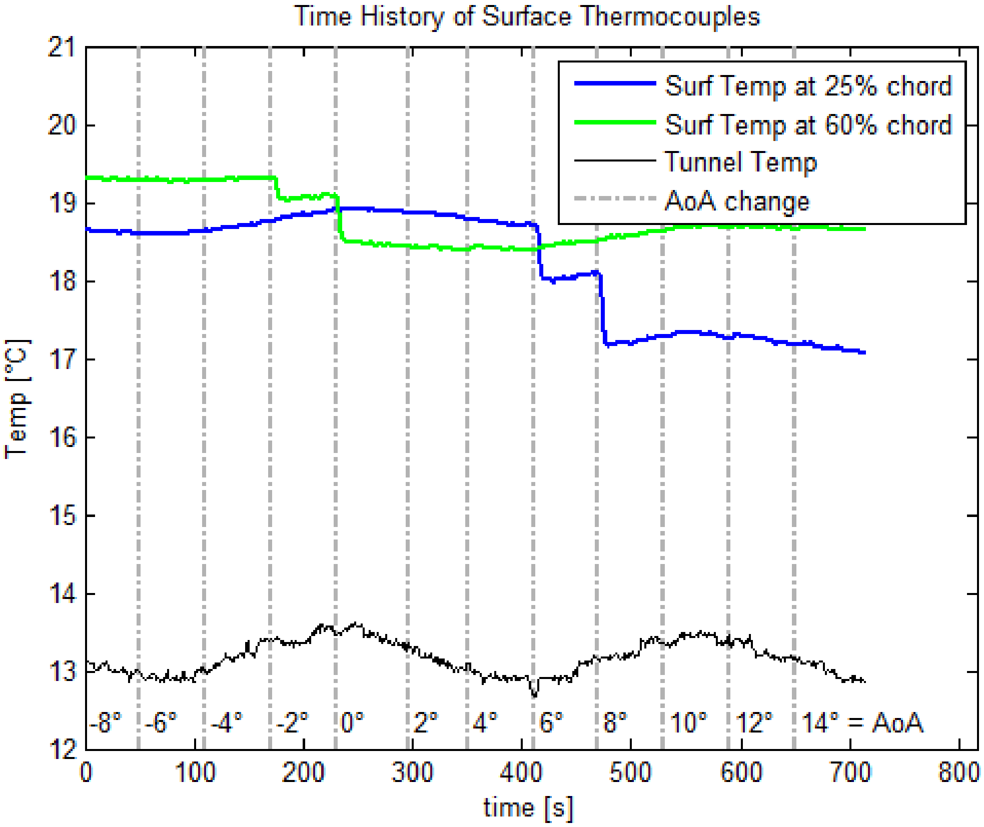

Figure 78 Time history of tunnel and surface temperatures for entire run corresponding to Figure 76

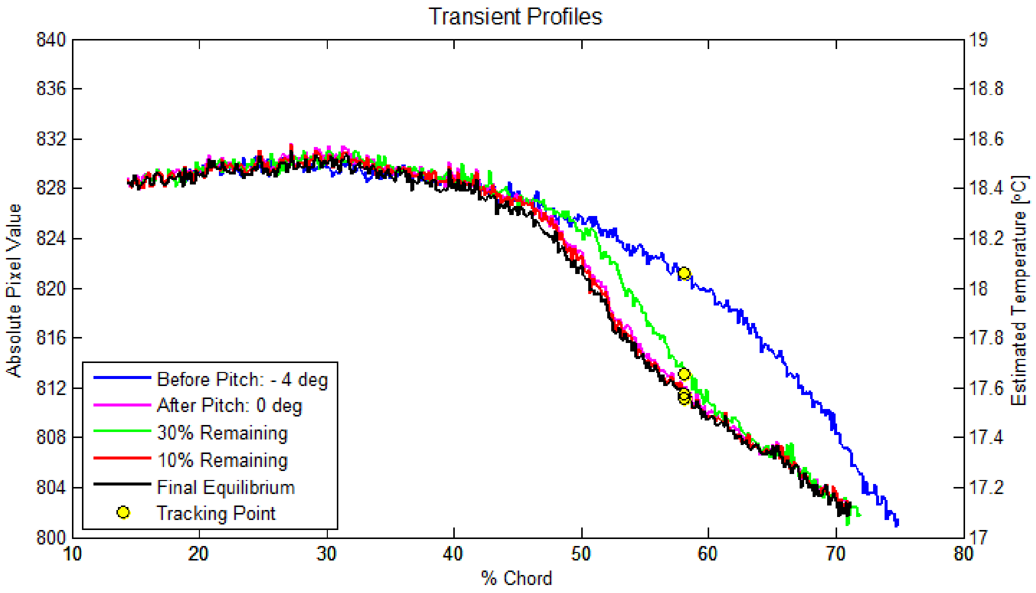

Figure 79 Temperature profiles throughout transient response as the model is pitched from AoA = -4° to 0°; configuration corresponds to Figure 76

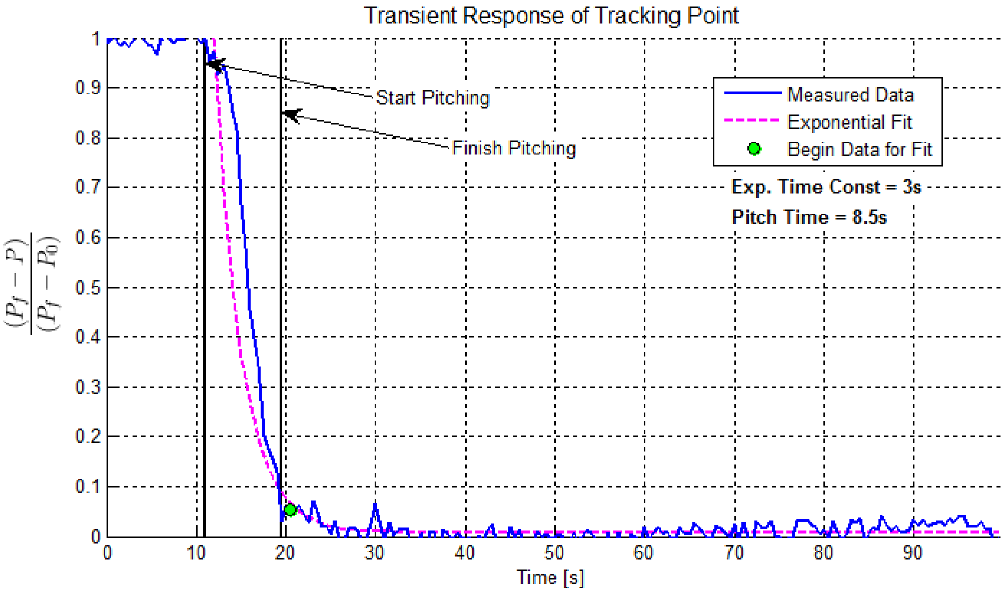

Figure 80 Response of tracking point shown in Figure 79 as a yellow circle Data is fit to an exponential decay function

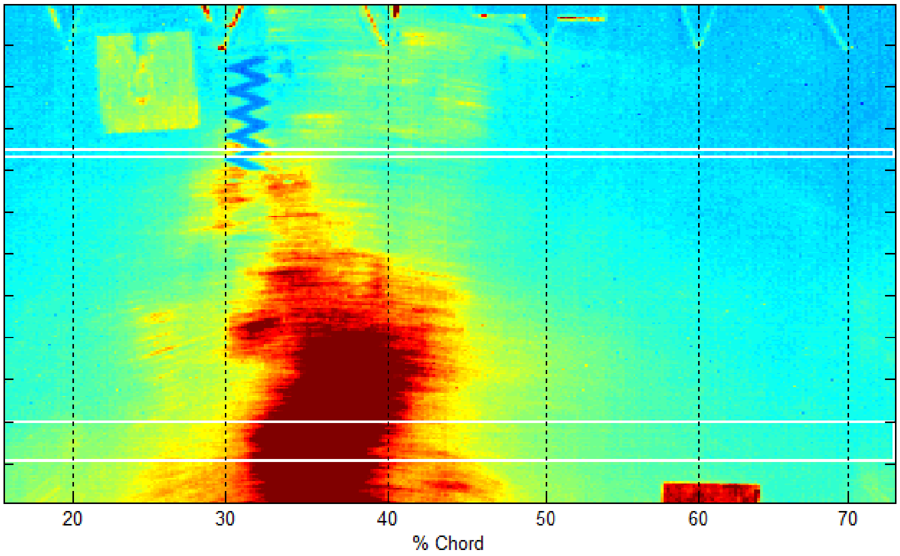

Figure 81 IR image of painted aluminum with layer of painted Bondo and using the heat lamp, AoA = 0° and $Re_c = 6.6\times10^5$

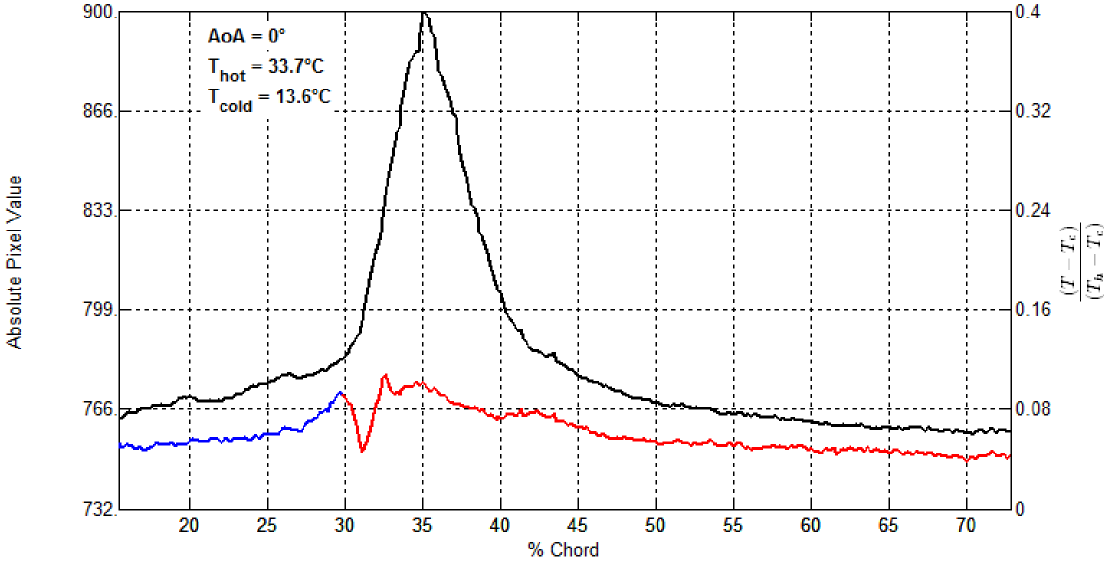

Figure 82 Surface temperature profile of Figure 81

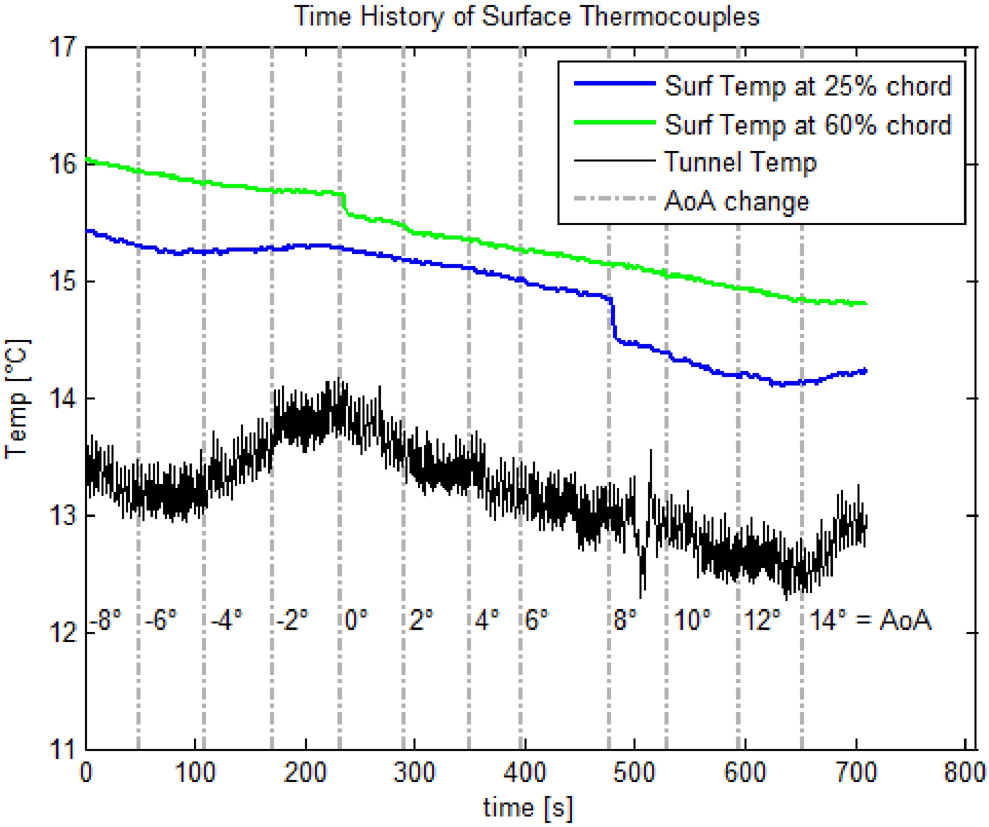

Figure 83 Time history of tunnel and surface temperatures for entire run corresponding to Figure 81

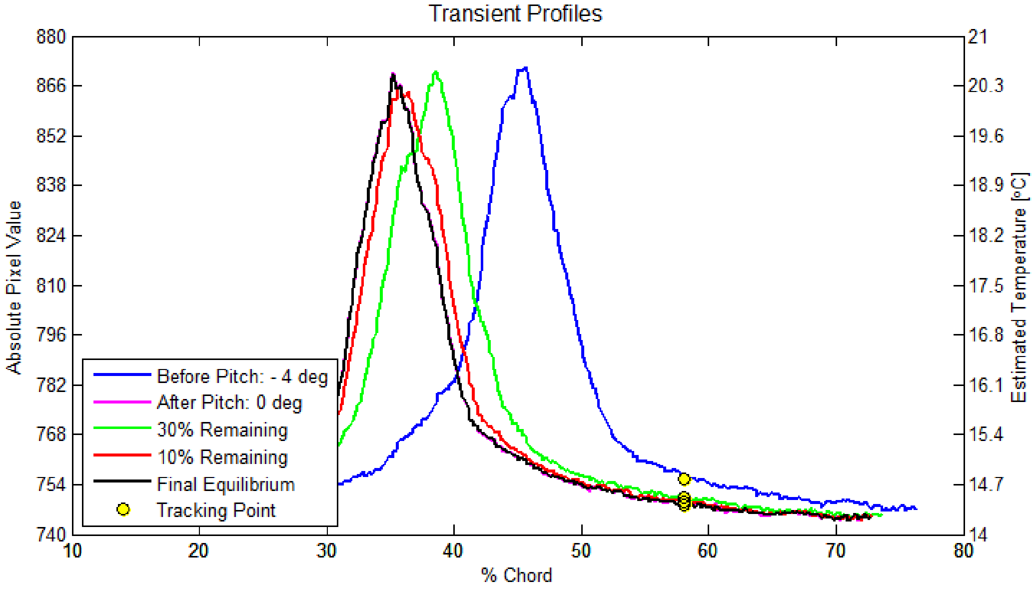

Figure 84 Temperature profiles throughout transient response as the model is pitched from AoA = -4° to 0°; configuration corresponds to Figure 81

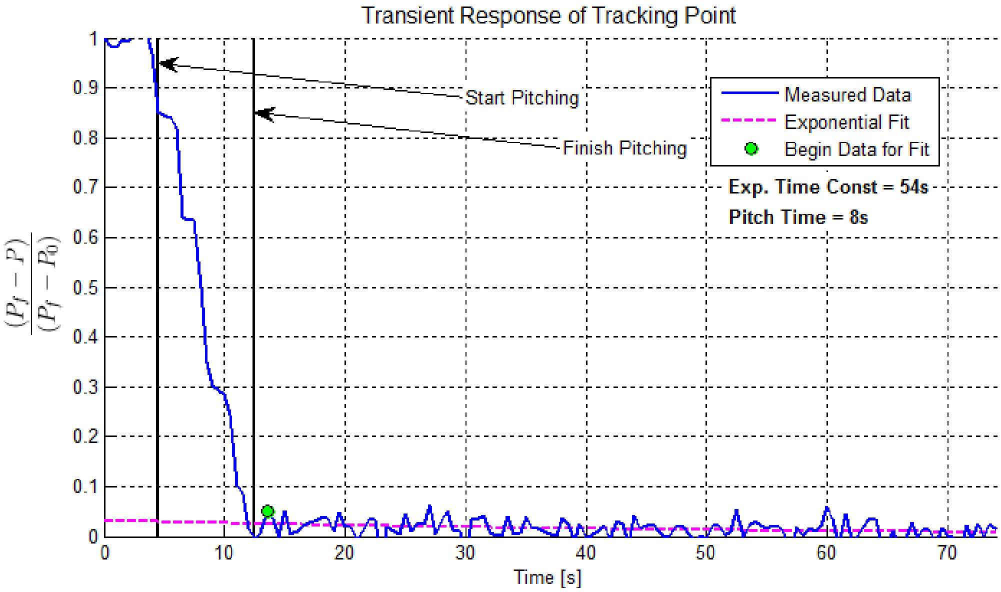

Figure 85 Response of tracking point shown in Figure 84 as a yellow circle Data is fit to an exponential decay function

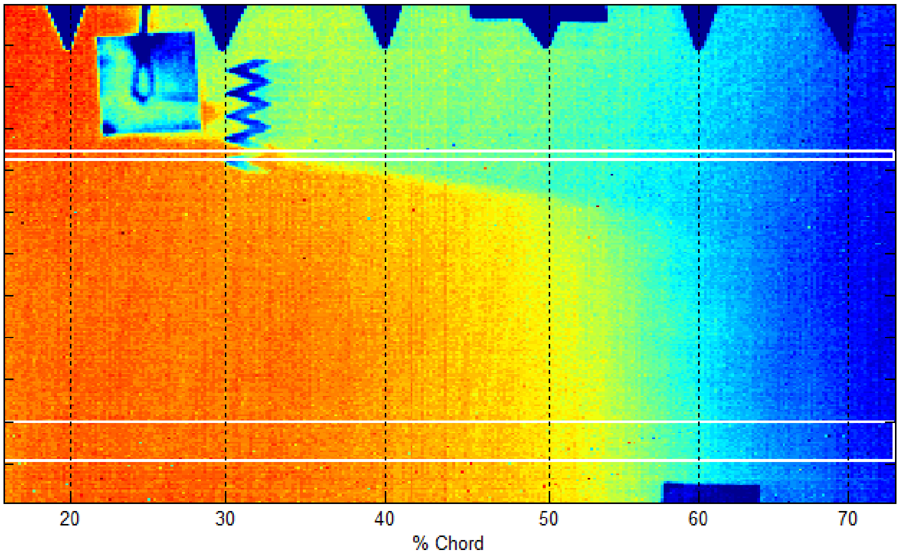

Figure 86 IR image of painted aluminum with layer of painted Bondo and using tap water circulation, AoA = 0° and $Re_c = 6.6 \times 10^5$

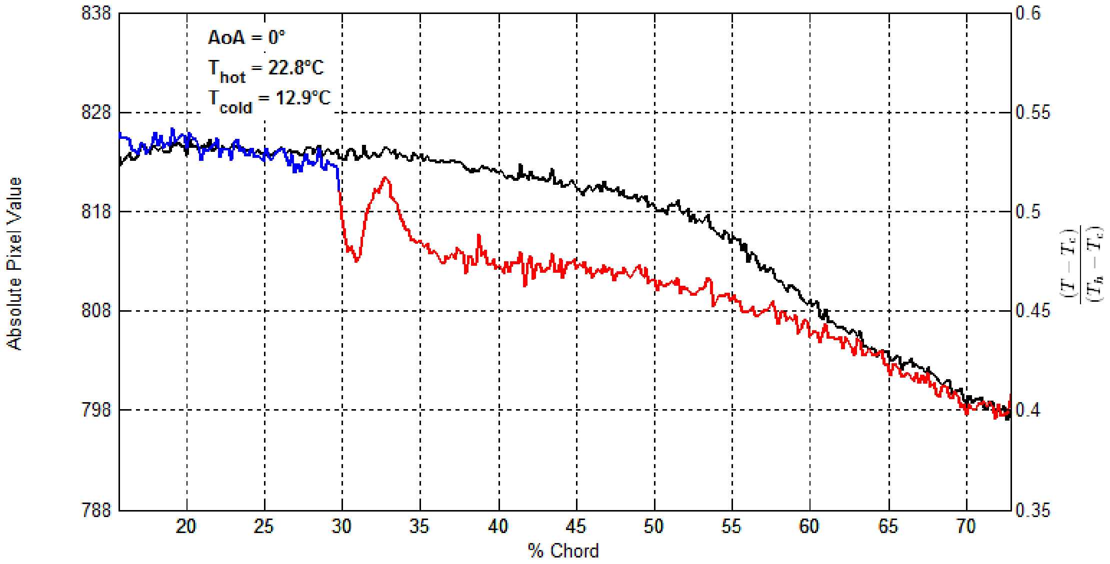

Figure 87 Surface temperature profile of Figure 86

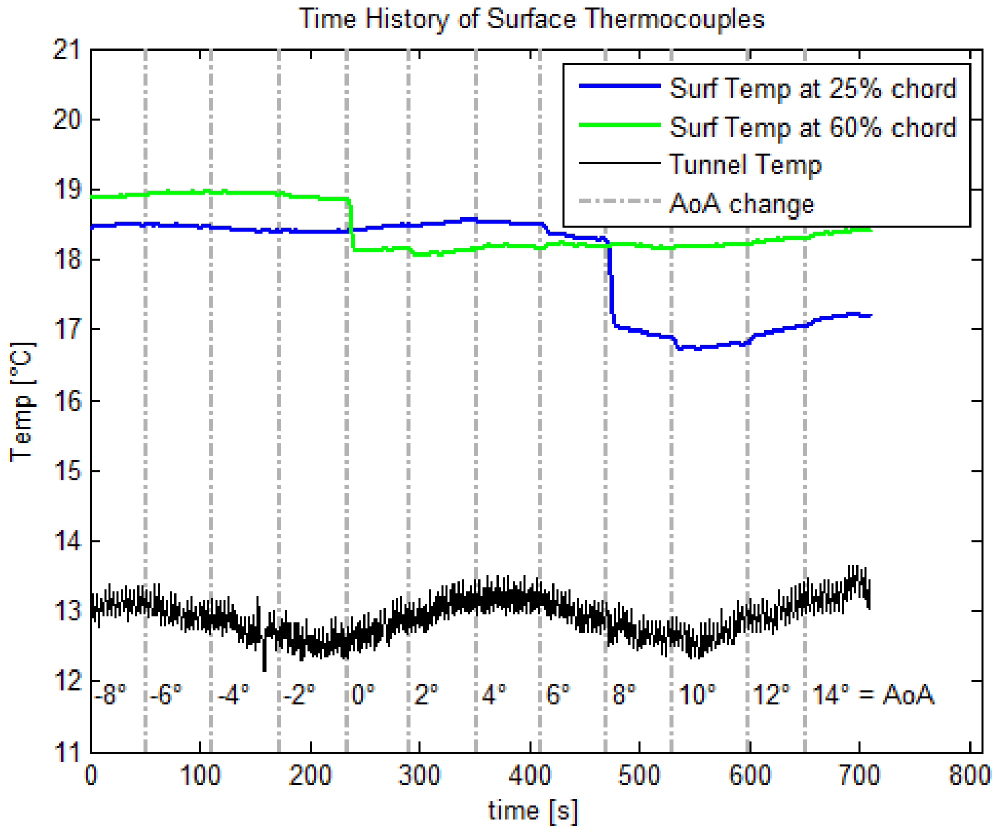

Figure 88 Time history of tunnel and surface temperatures for entire run corresponding to Figure 86

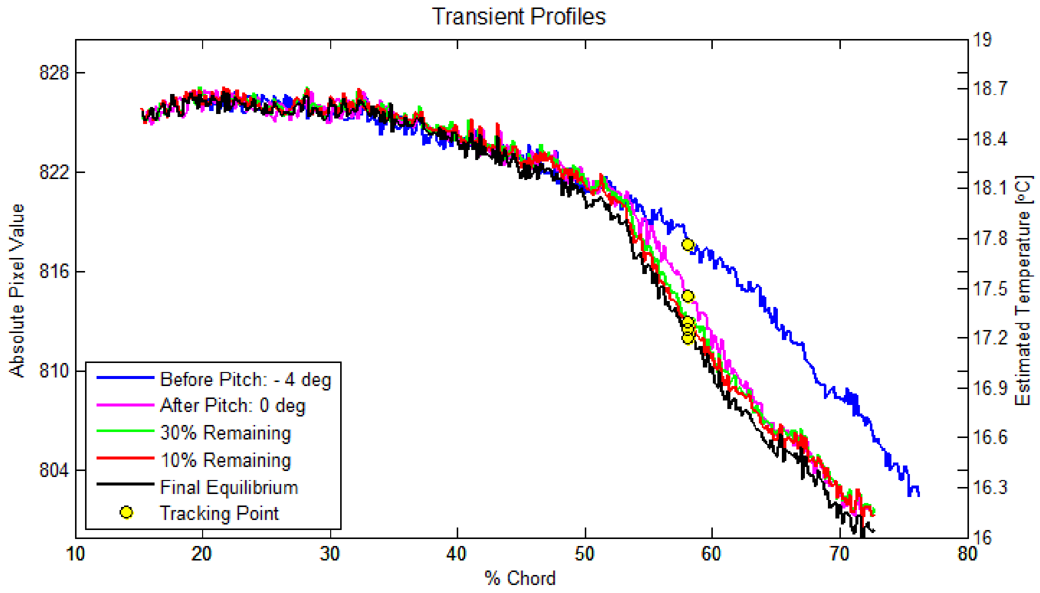

Figure 89 Temperature profiles throughout transient response as the model is pitched from AoA = -4° to 0°; configuration corresponds to Figure 86

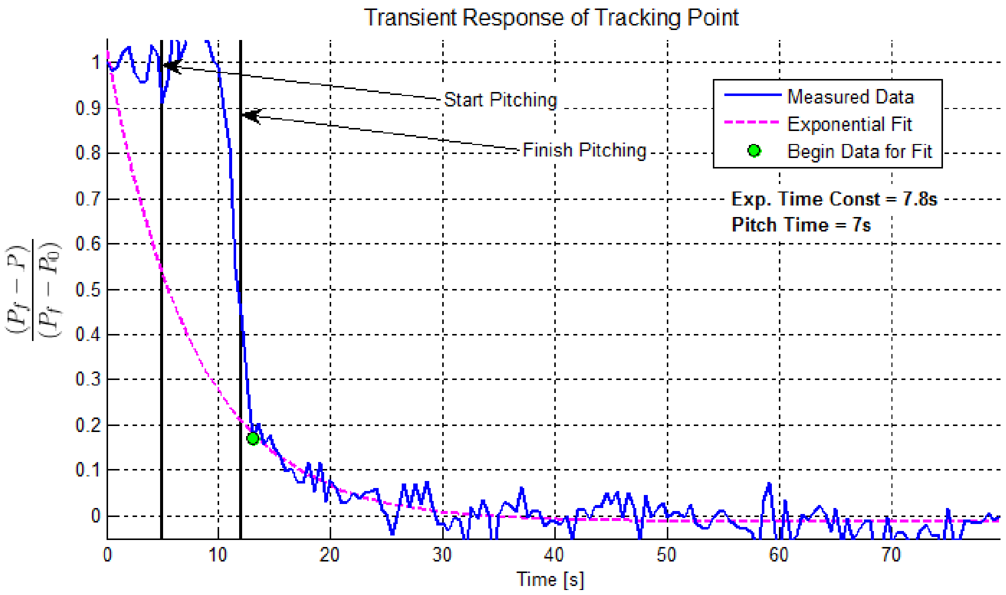

Figure 90 Response of tracking point shown in Figure 89 as a yellow circle Data is fit to an exponential decay function

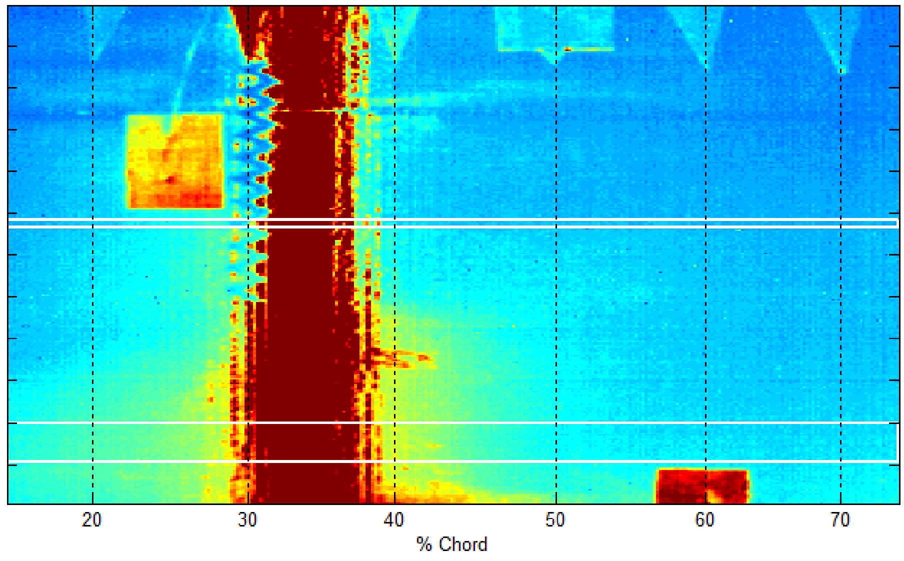

Figure 91 IR image of as-built RP plastic using the heat lamp
AoA = 0° and $Re_c = 6.6 \times 10^5$

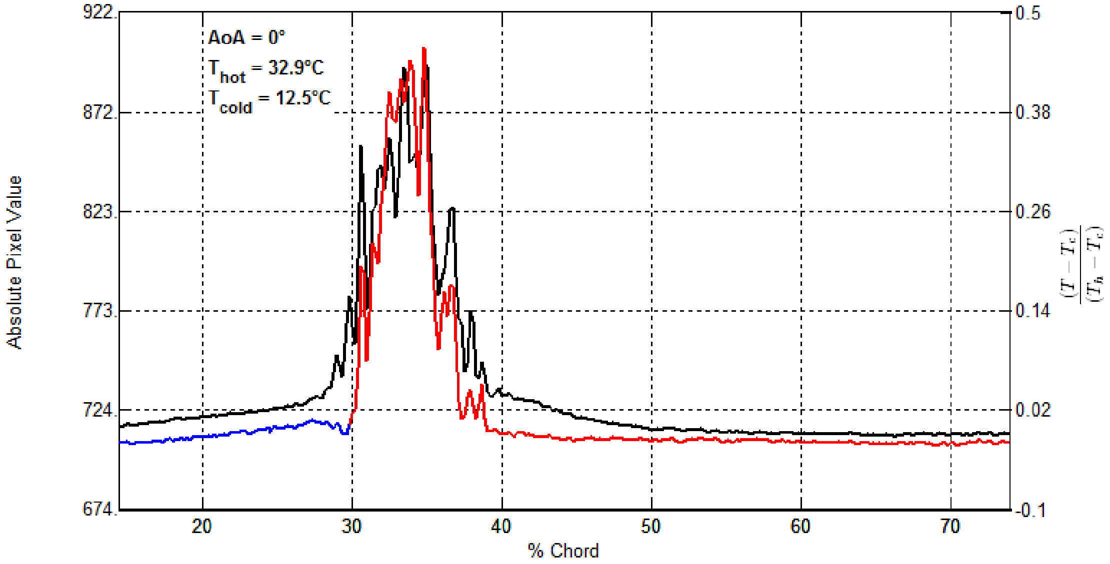

Figure 92 Surface temperature profile of Figure 91

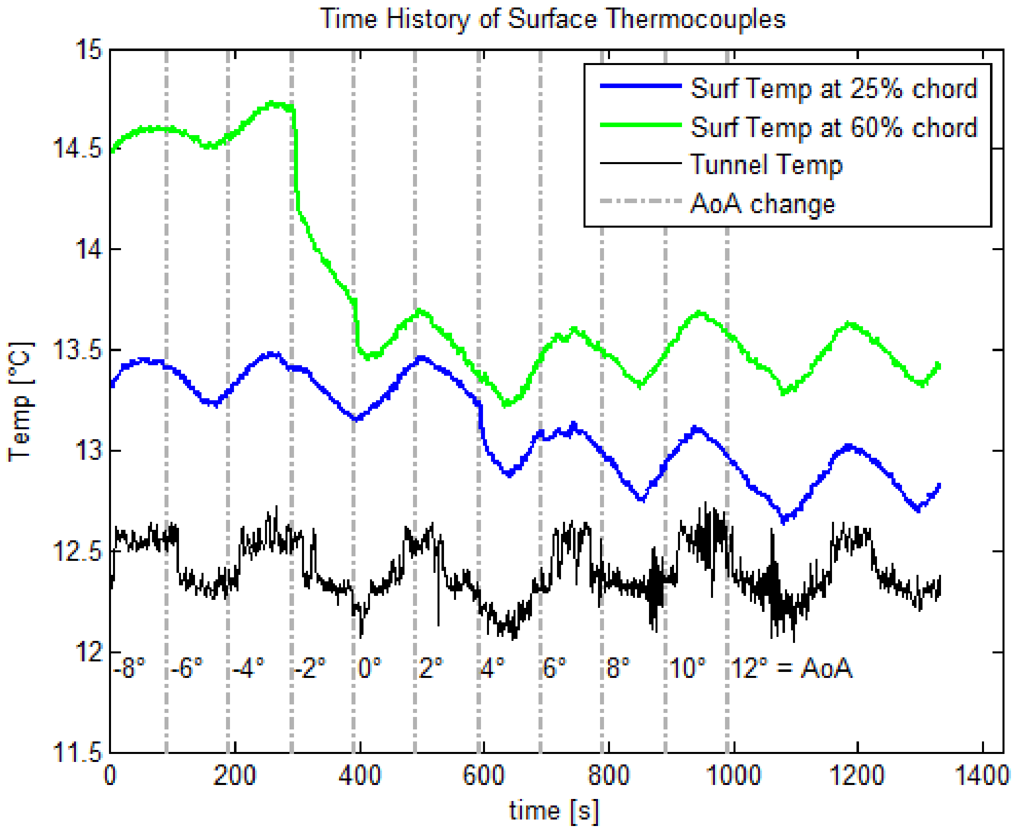

Figure 93 Time history of tunnel and surface temperatures for entire run corresponding to Figure 91

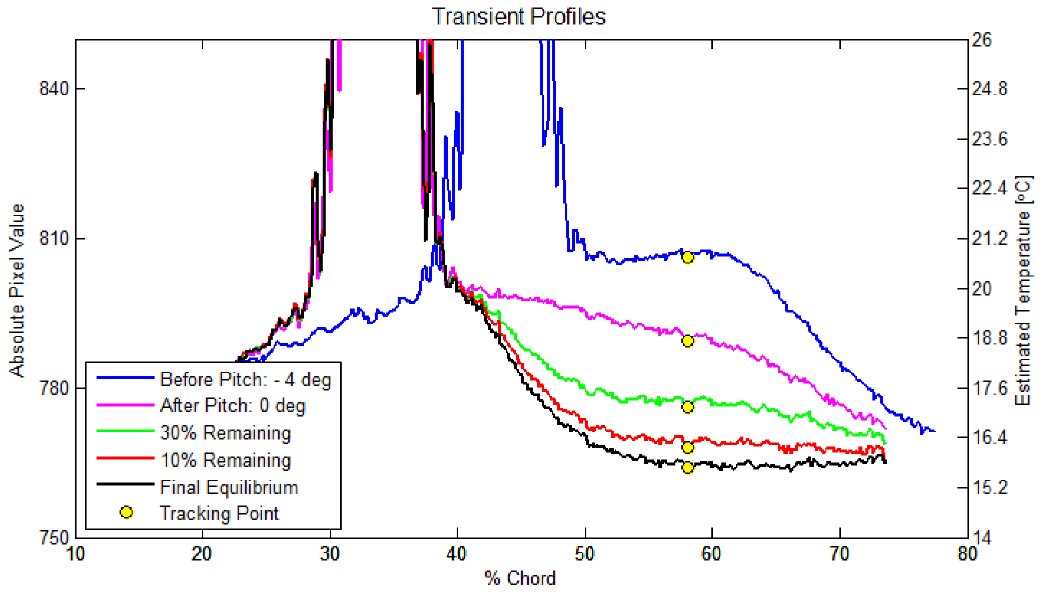

Figure 94 Temperature profiles throughout transient response as the model is pitched from AoA = -4° to 0°; configuration corresponds to Figure 91

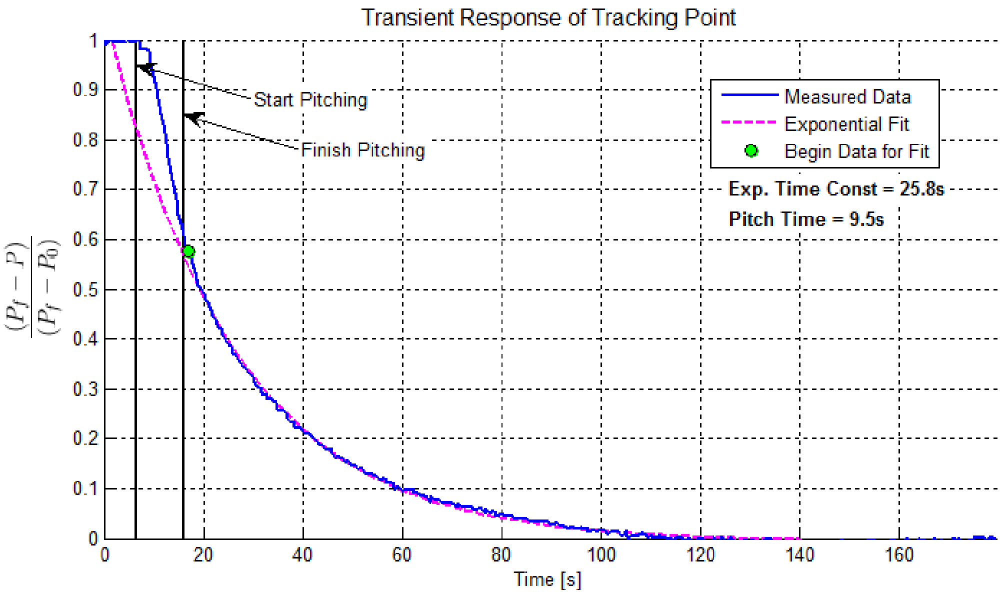

Figure 95 Response of tracking point shown in Figure 94 as a yellow circle Data is fit to an exponential decay function

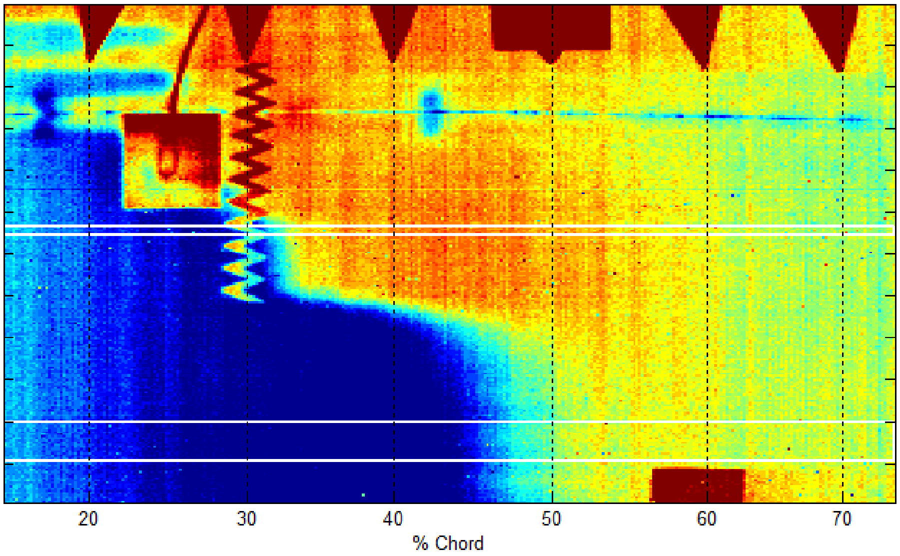

Figure 96 IR image of as-built RP plastic using ice water circulation, AoA = 0° and $Re_c = 6.6\times10^5$

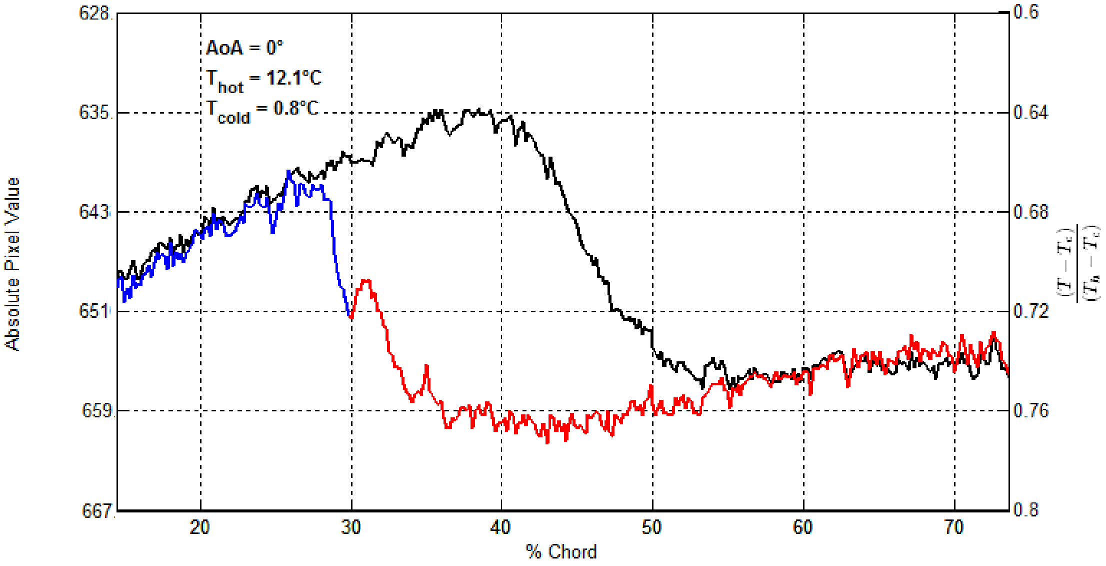

Figure 97 Surface temperature profile of Figure 96

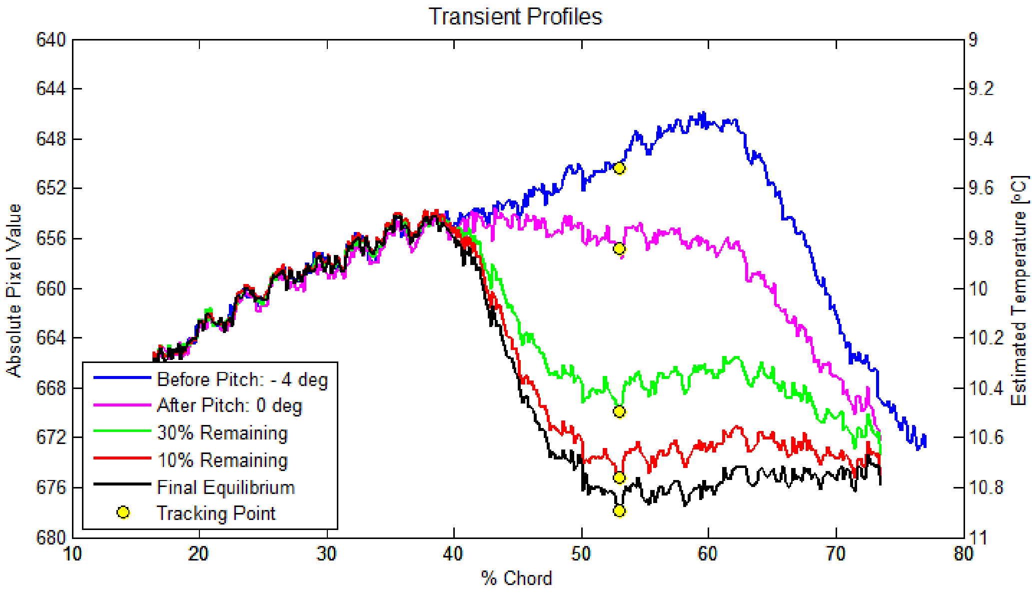

Figure 98 Temperature profiles throughout transient response as the model is pitched from AoA = -4° to 0°; configuration corresponds to Figure 96

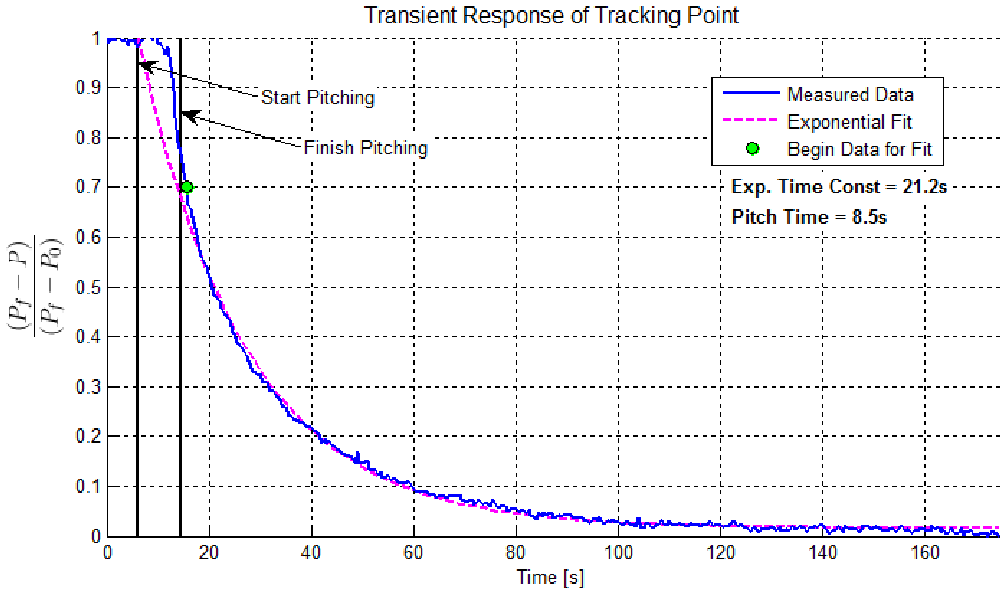

Figure 99 Response of tracking point shown in Figure 98 as a yellow circle Data is fit to an exponential decay function

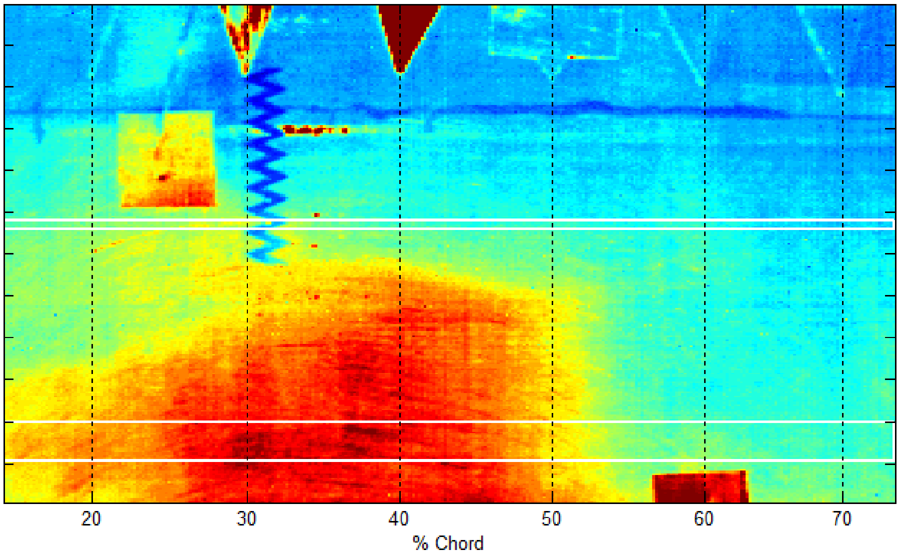

Figure 100 IR image of the sanded RP plastic using the heat lamp, AoA = 0° and $Re_c = 6.6\times10^5$

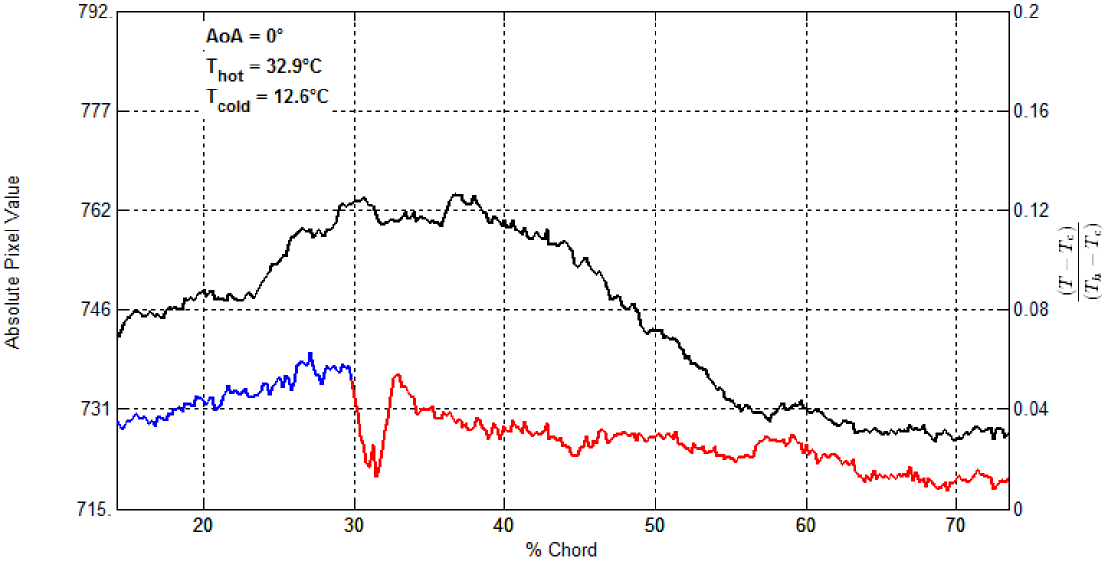

Figure 101 Surface temperature profile of Figure 100

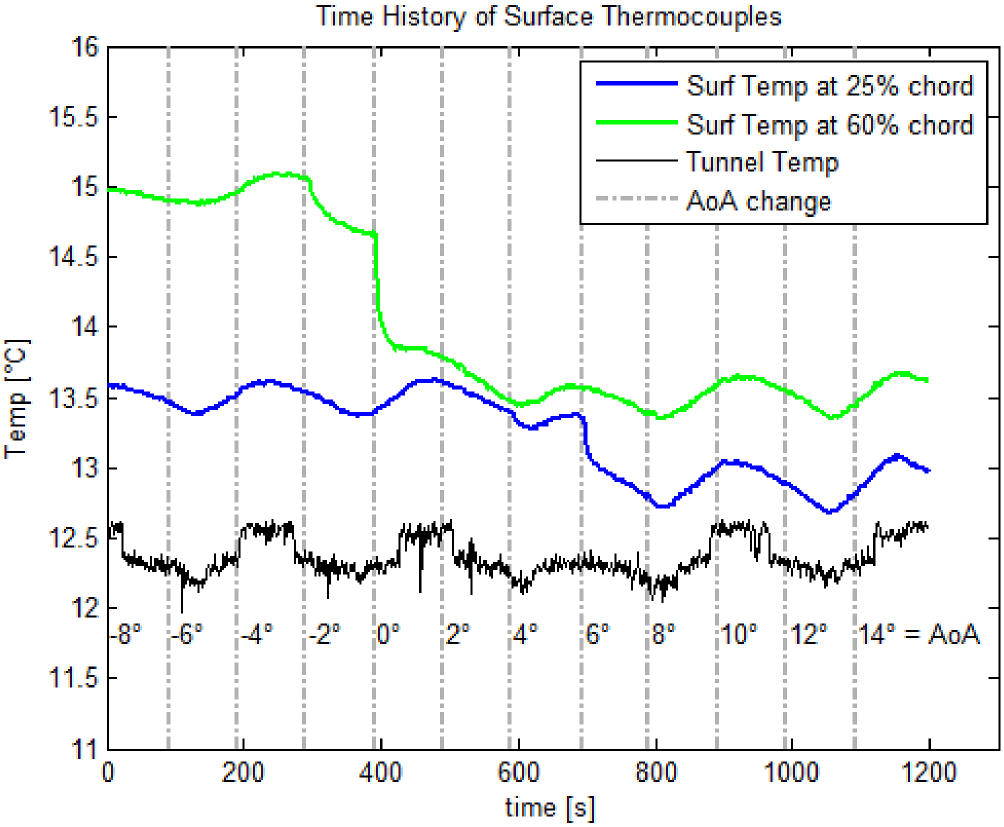

Figure 102 Time history of tunnel and surface temperatures for entire run corresponding to Figure 100

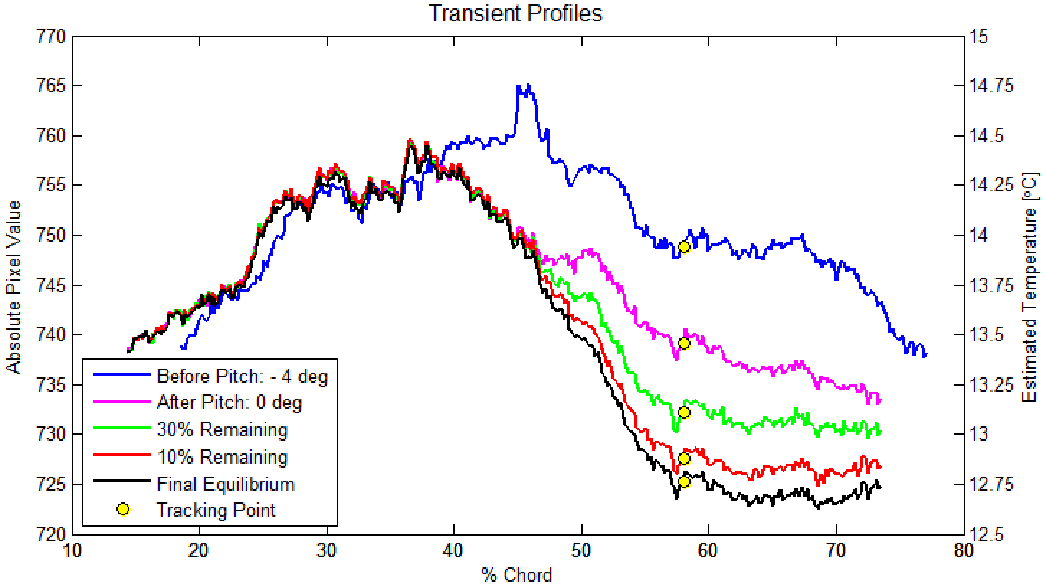

Figure 103 Temperature profiles throughout transient response as the model is pitched from AoA = -4° to 0°; configuration corresponds to Figure 100

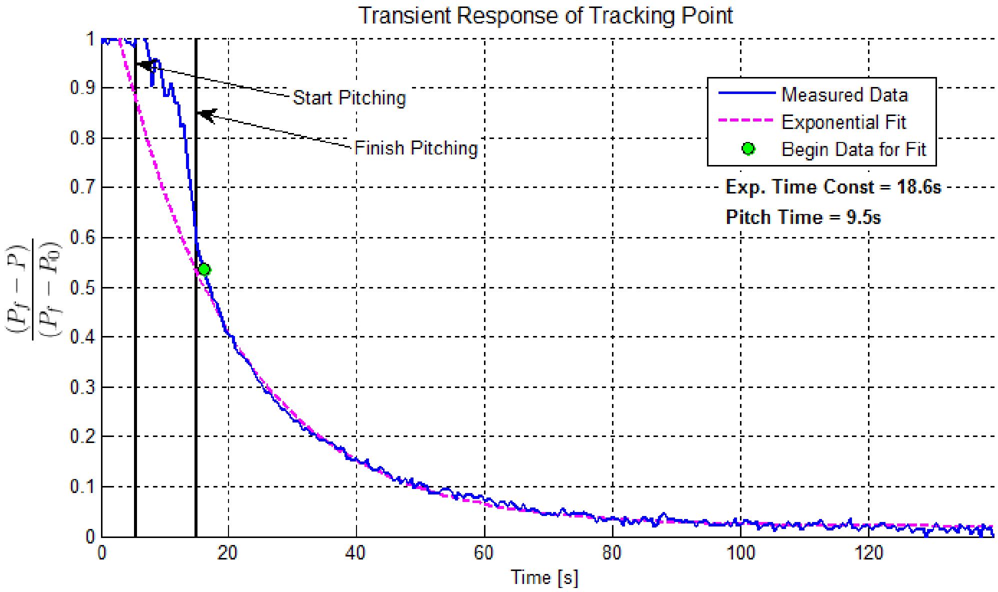

Figure 104 Response of tracking point shown in Figure 103 as a yellow circle Data is fit to an exponential decay function

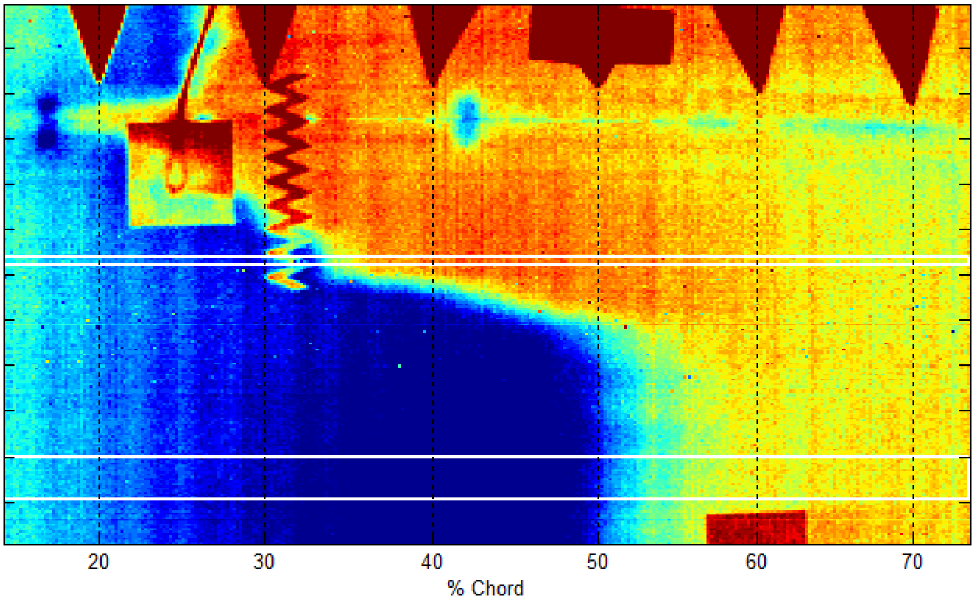

Figure 105 IR image of the sanded RP plastic using ice water circulation, AoA = 0° and $Re_c = 6.6\times10^5$

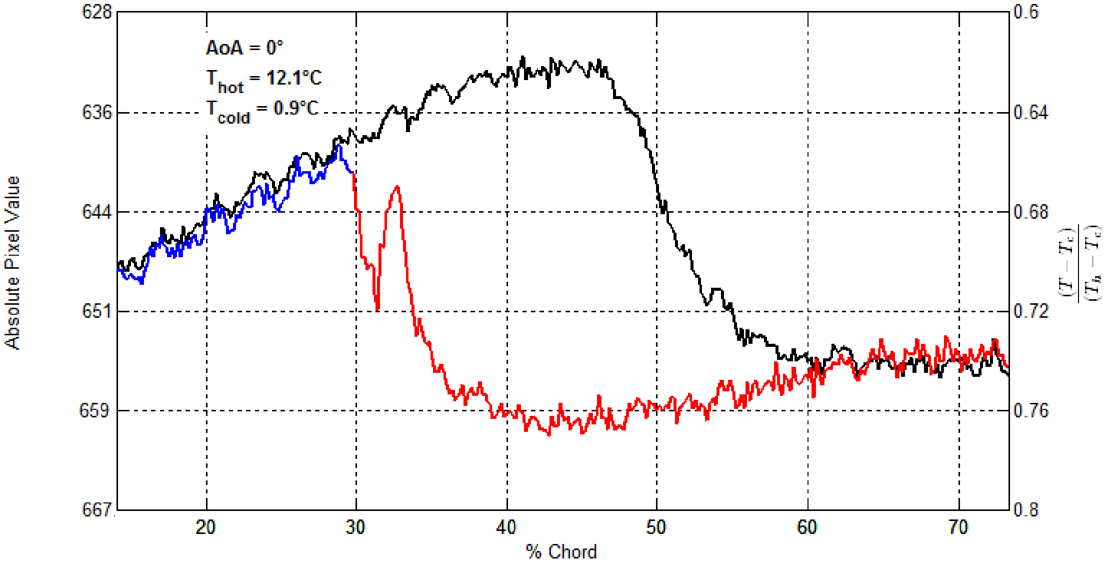

Figure 106 Surface temperature profile of Figure 105

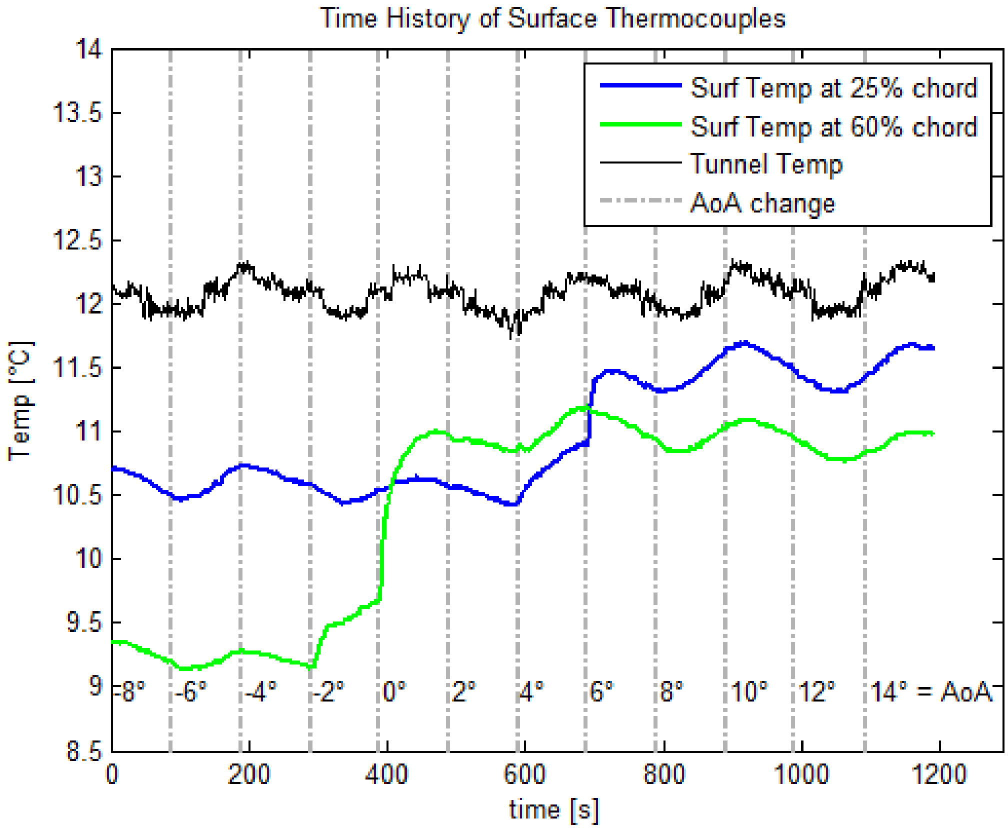

Figure 107 Time history of tunnel and surface temperatures for entire run corresponding to Figure 105

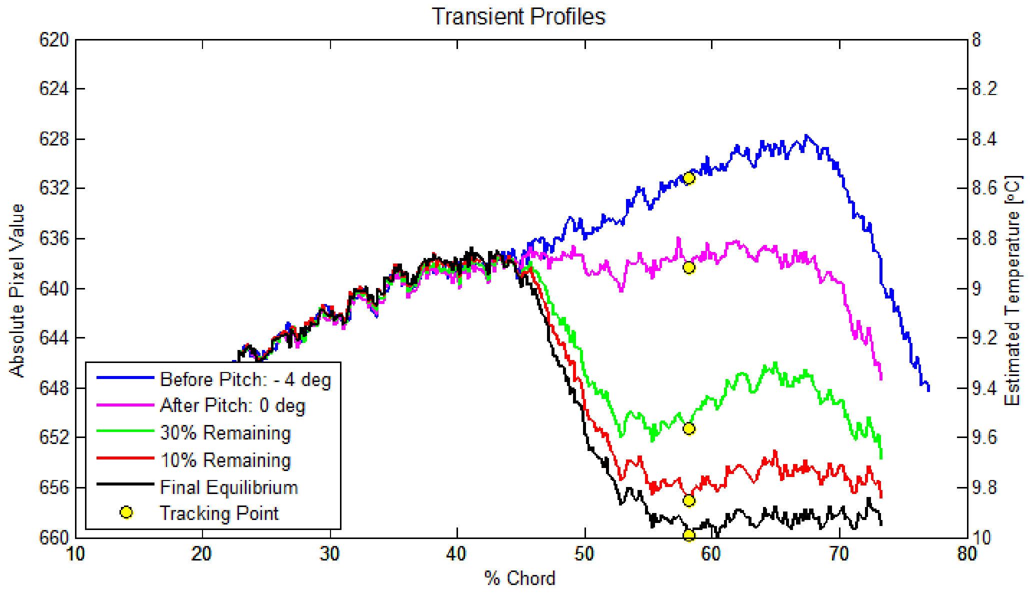

Figure 108 Temperature profiles throughout transient response as the model is pitched from AoA = -4° to 0°; configuration corresponds to Figure 105

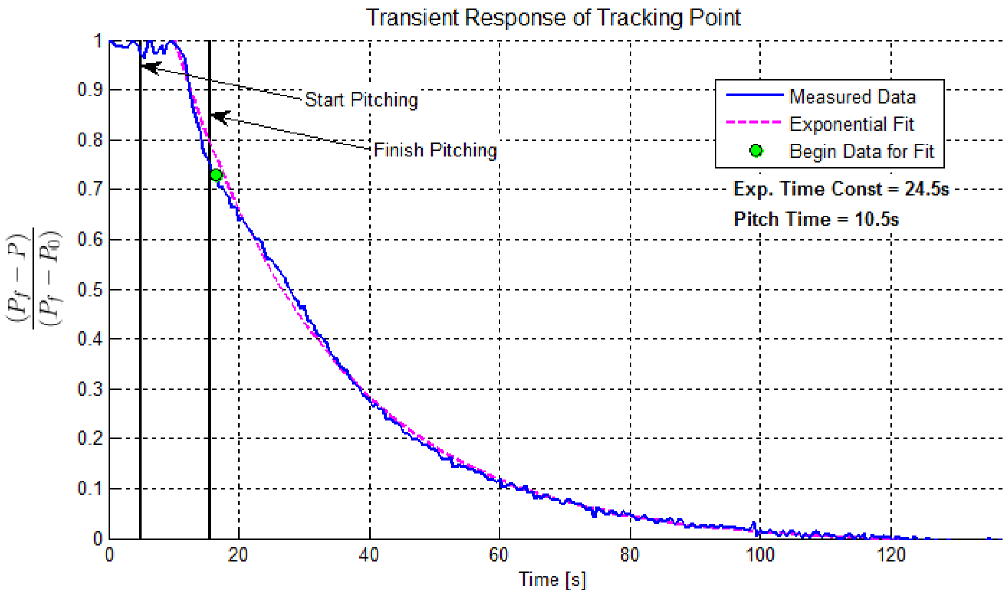

Figure 109 Response of tracking point shown in Figure 108 as a yellow circle Data is fit to an exponential decay function

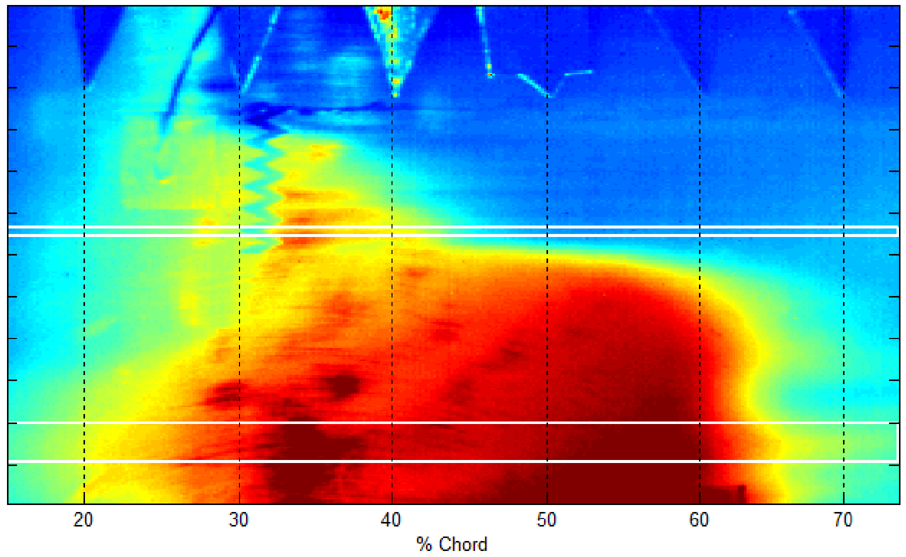

Figure 110 IR image of Painted RP plastic using the heat lamp, AoA = 0, $Re_c = 2.2\times10^5$

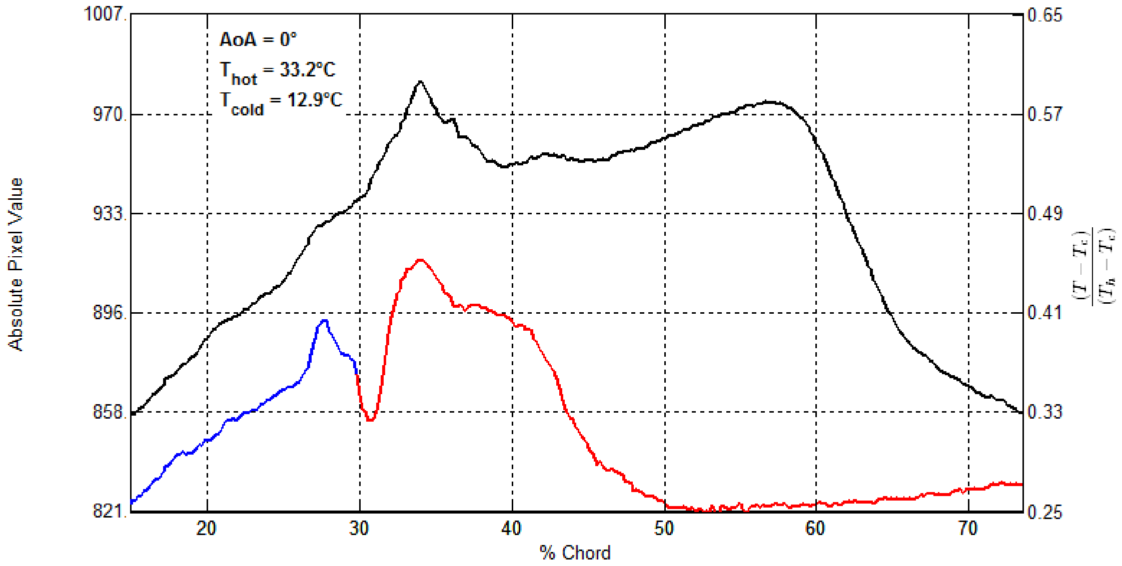

Figure 111 Surface Temp Profile of Painted RP in Figure 110

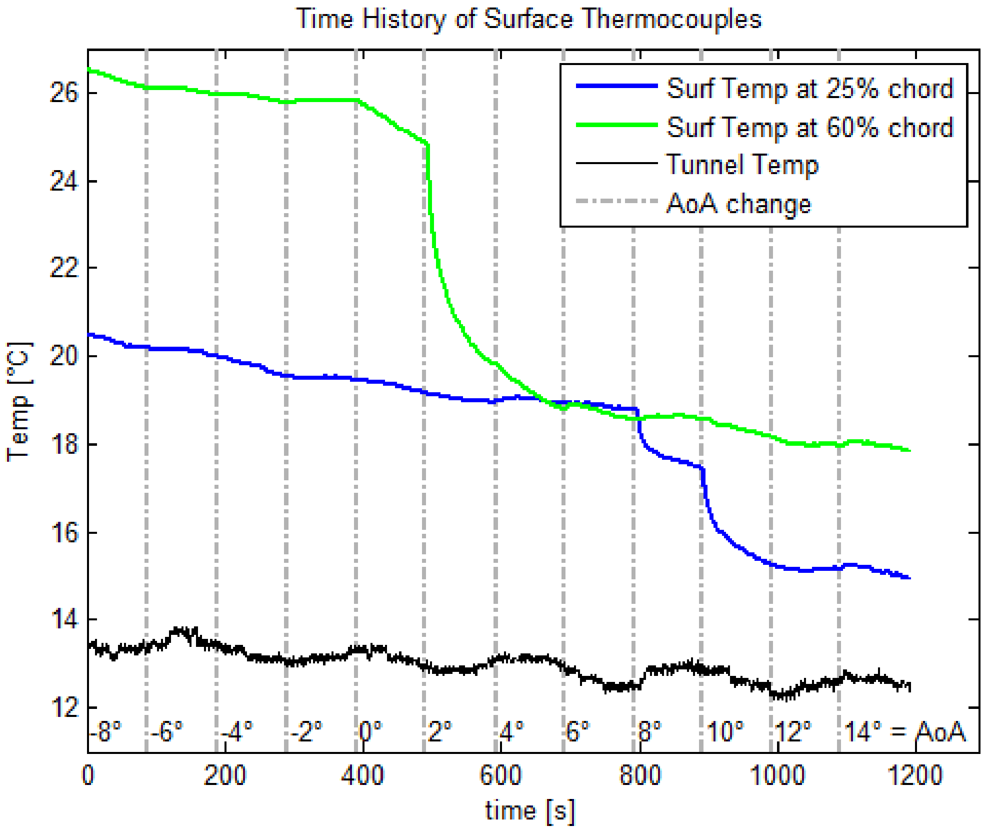

Figure 112 Time history of tunnel and surface temperatures for entire run corresponding to Figure 110

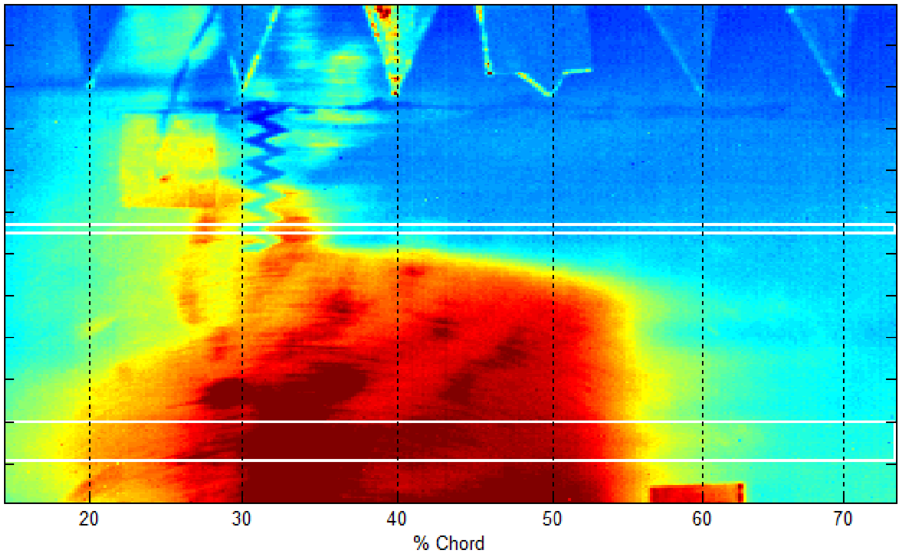

Figure 113 IR image of Painted RP plastic using the heat lamp, AoA = 0, $Re_c = 4.4 \times 10^5$

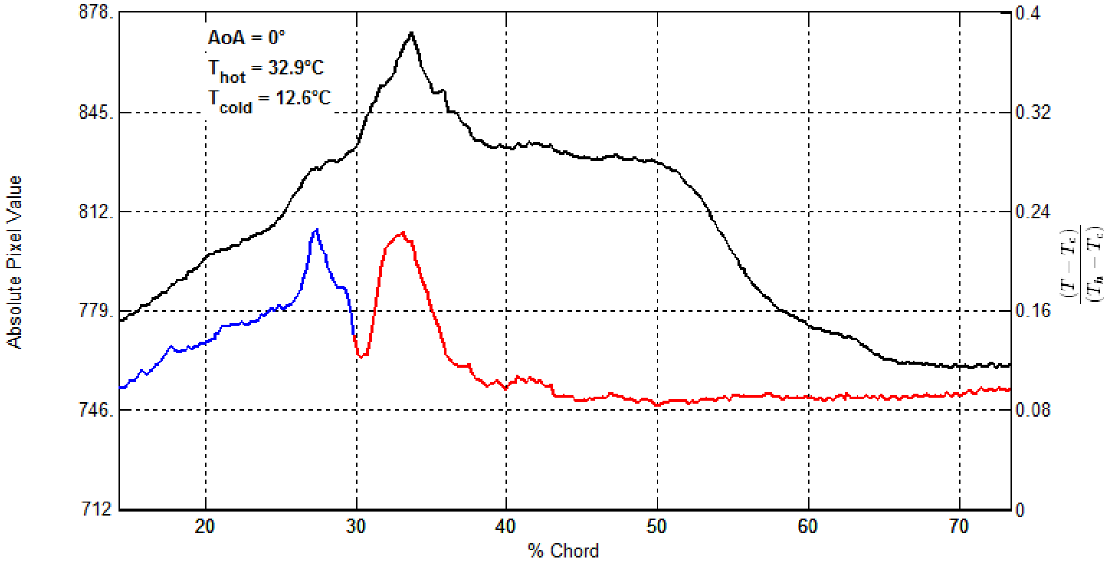

Figure 114 Surface Temperature Profile of Painted RP in Figure **113**

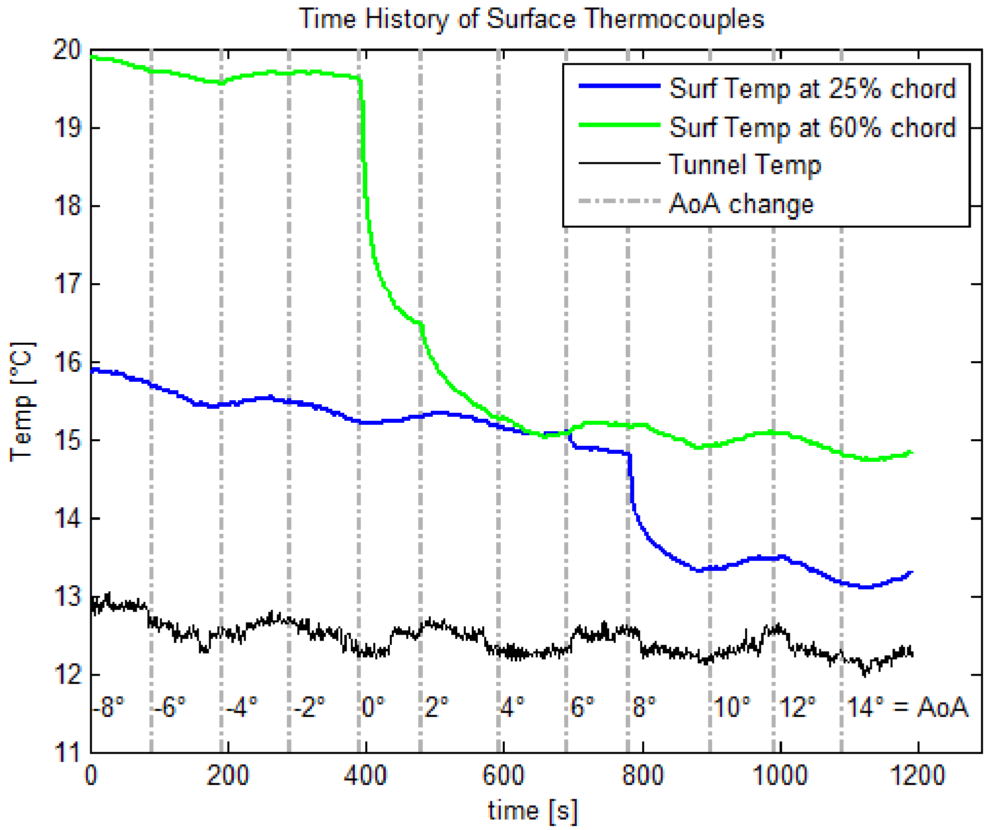

Figure 115 Time history of tunnel and surface temperatures for entire run corresponding to Figure **113**

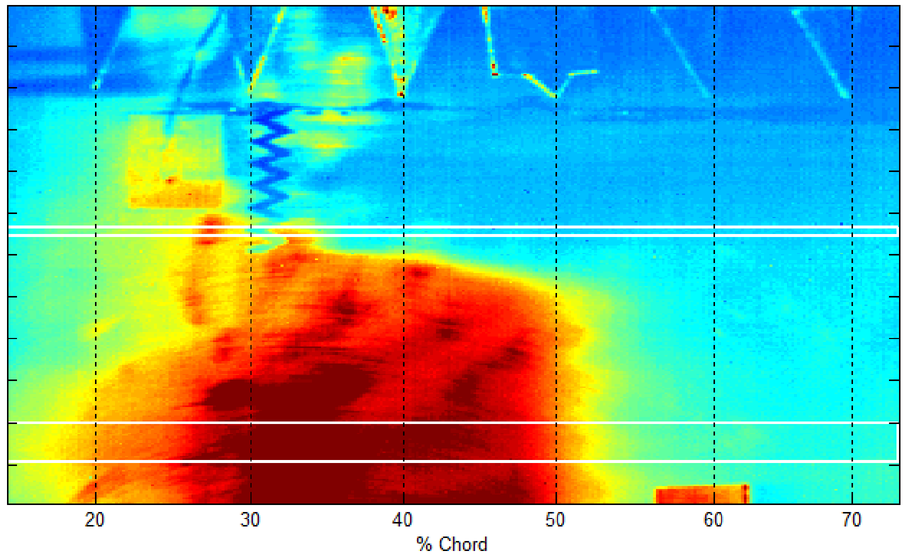

Figure 116 IR image of the painted RP plastic using the heat lamp, AoA = 0° and $Re_c = 6.6 \times 10^5$

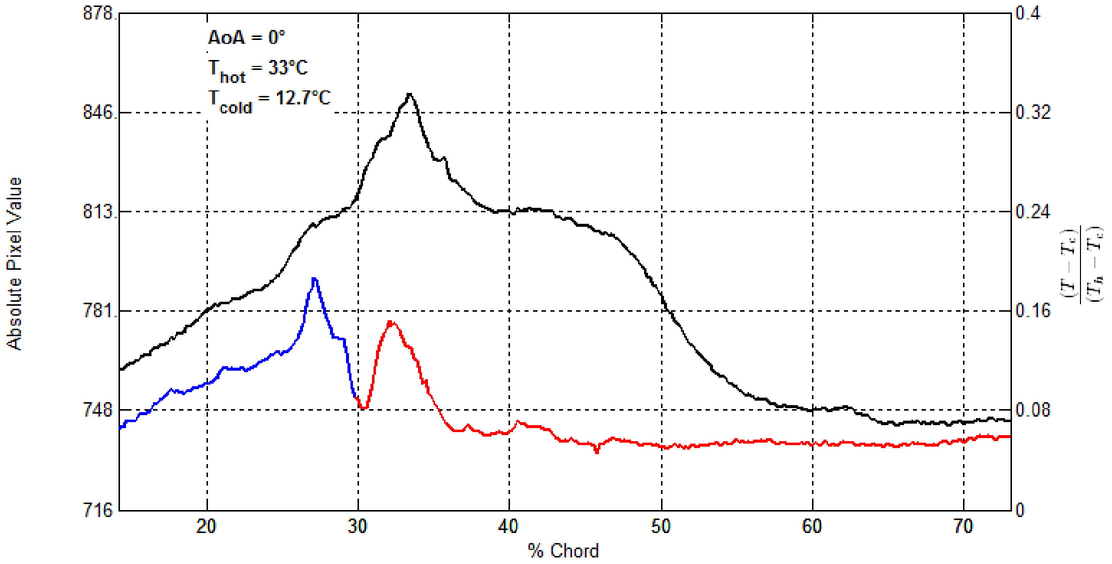

Figure 117 Surface temperature profile of Figure 116

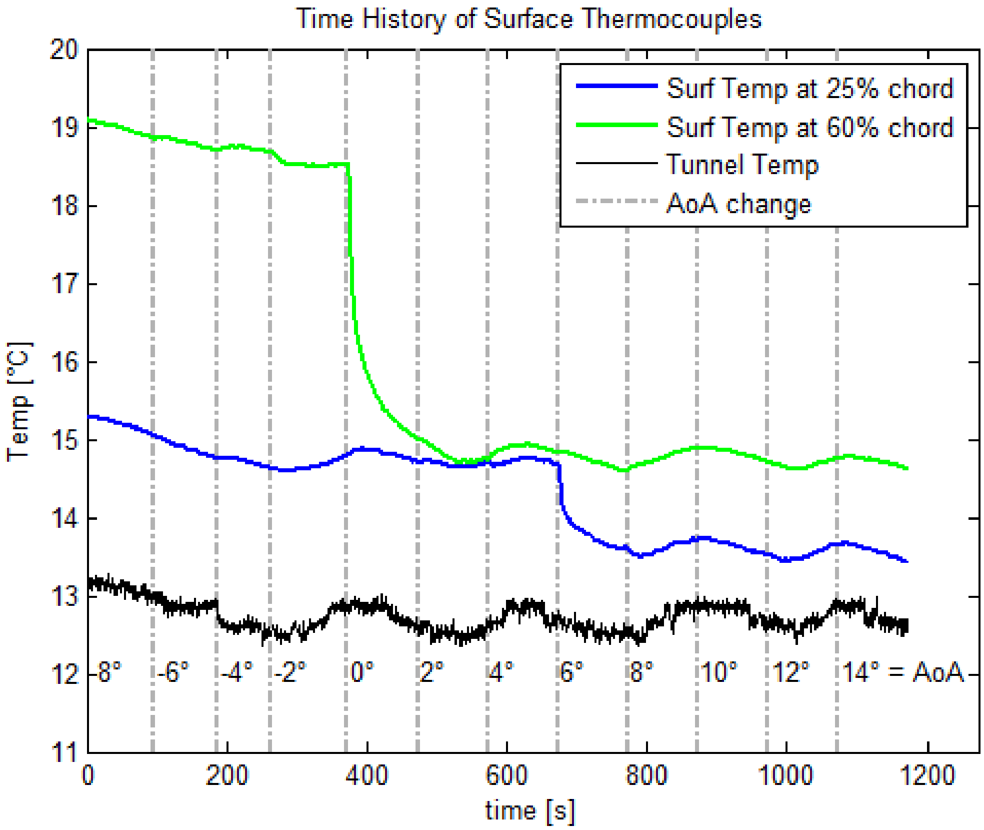

Figure 118 Time history of tunnel and surface temperatures for entire run corresponding to Figure 116

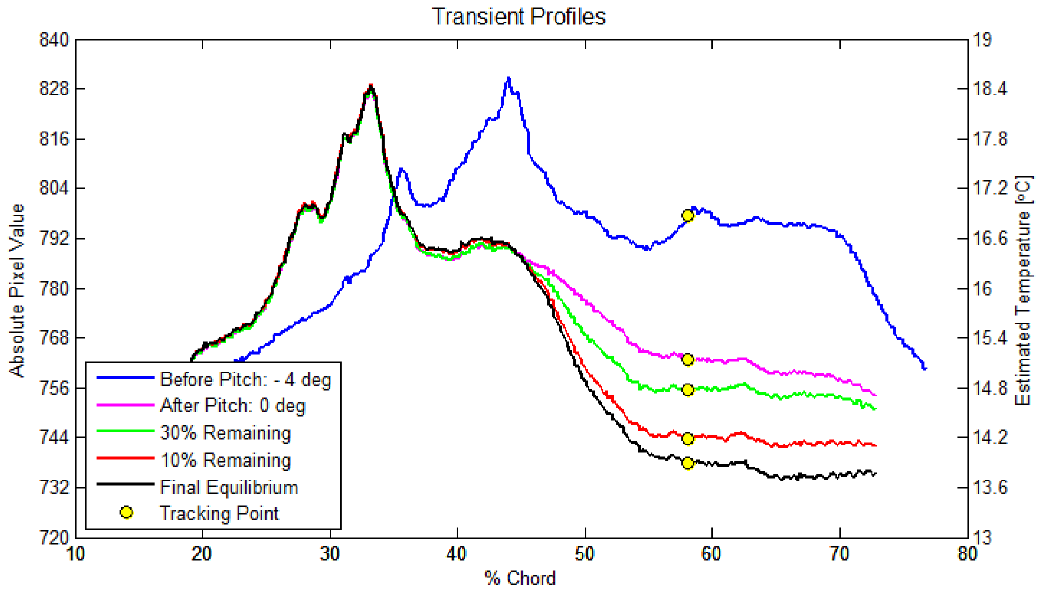

Figure 119 Temperature profiles throughout transient response as the model is pitched from AoA = -4° to 0°; configuration corresponds to Figure 116

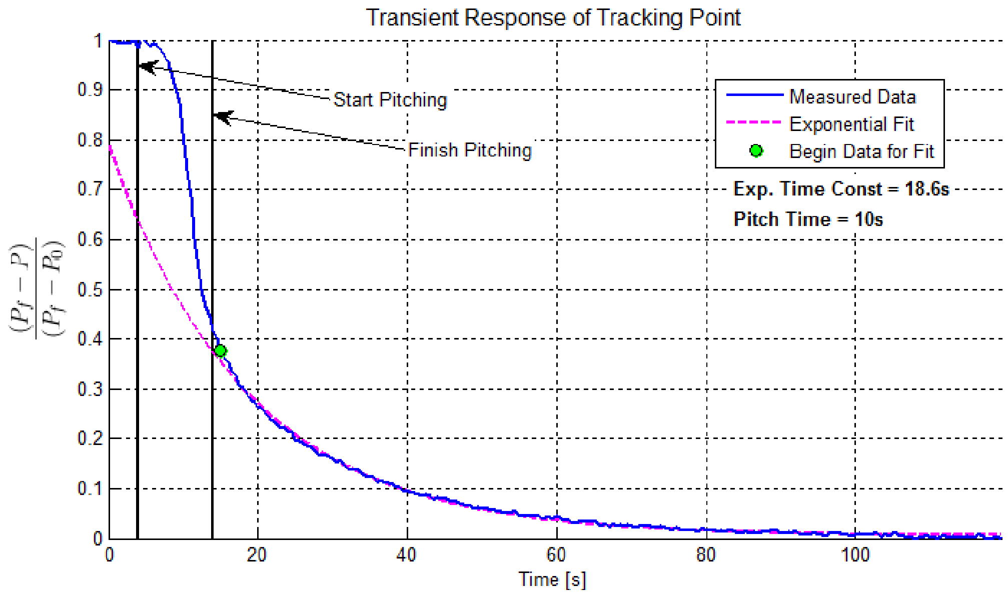

Figure 120 Response of tracking point shown in Figure 119 as a yellow circle Data is fit to an exponential decay function

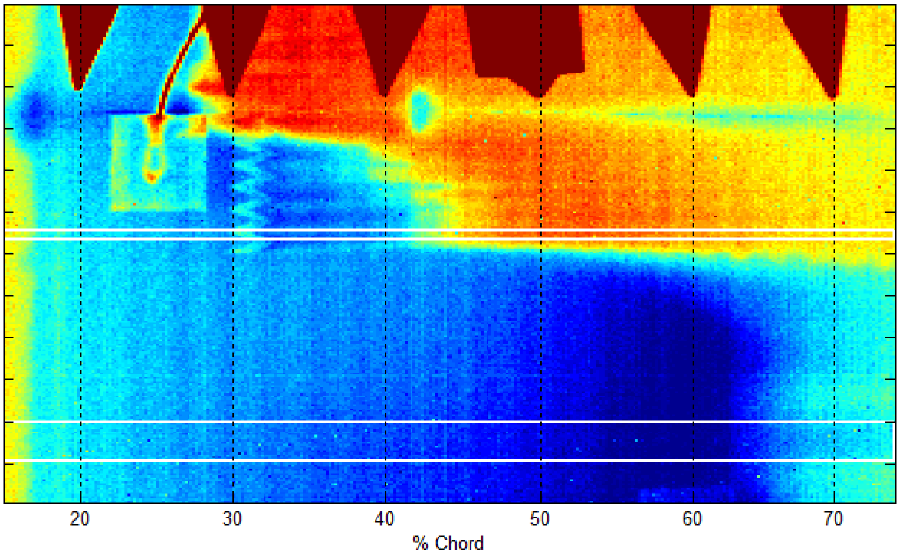

Figure 121 IR image of Painted RP with ice water, AoA = 0, $Re_c = 2.2\times10^5$

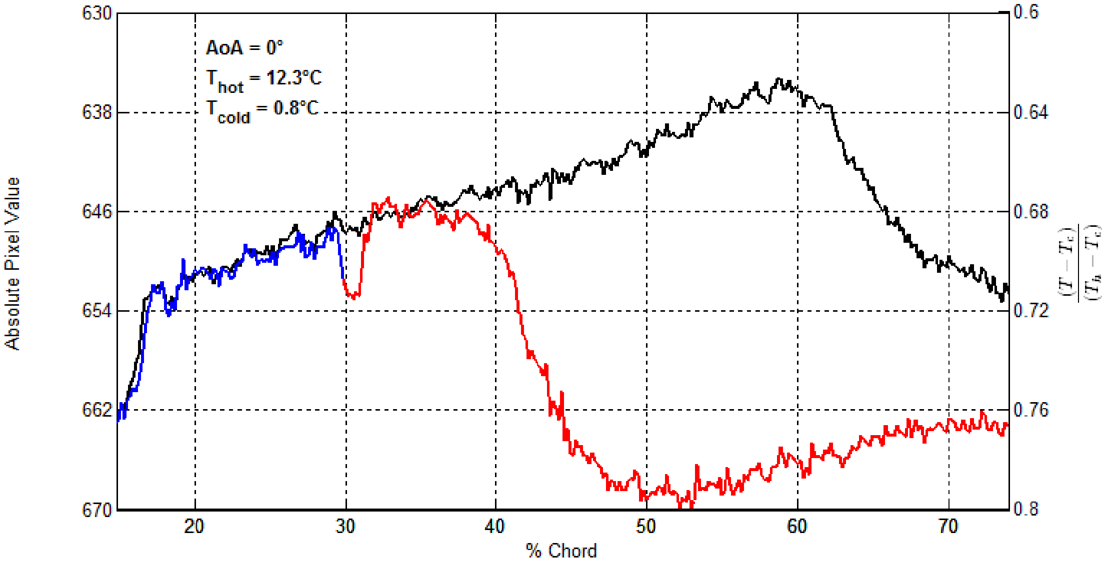

Figure 122 Surface temperature profile of painted RP with ice water in Figure 121

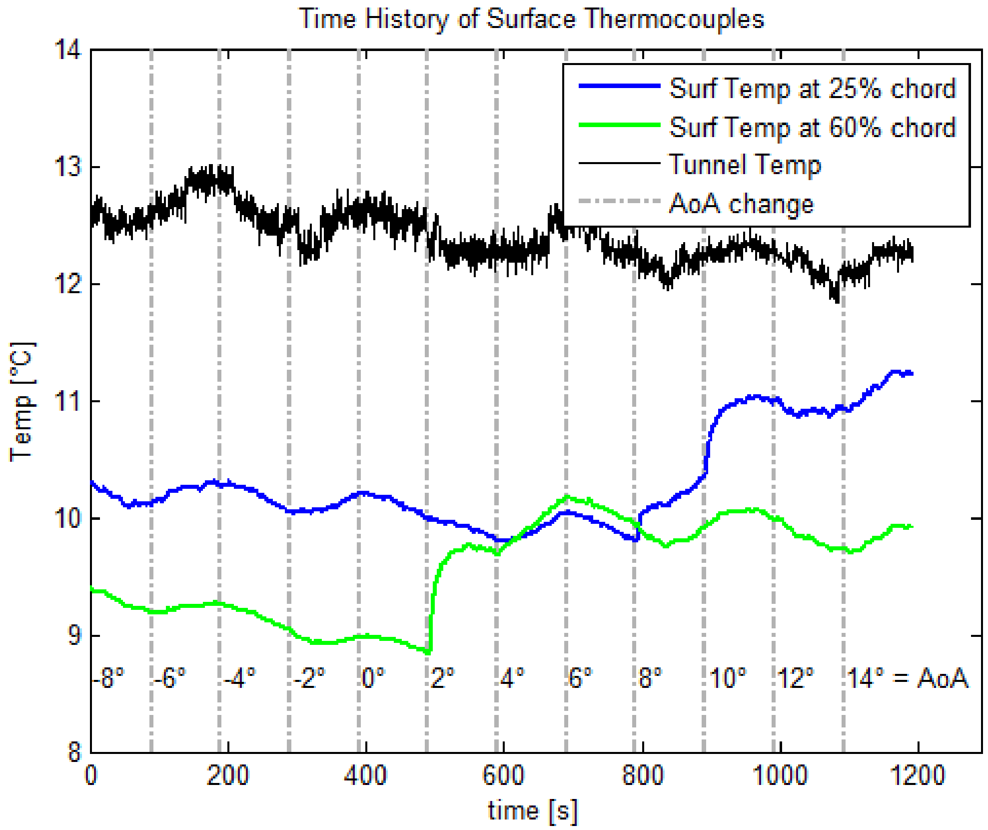

Figure 123 Time history of tunnel and surface temperatures for entire run corresponding to Figure 121

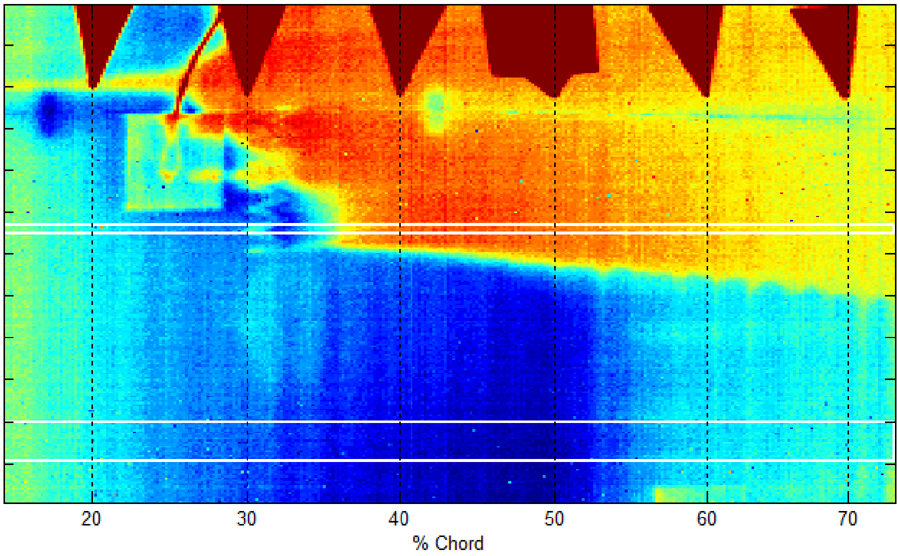

Figure 124 IR image of painted RP plastic using ice water circulation, AoA = 0, $Re_c = 4.4\times10^5$

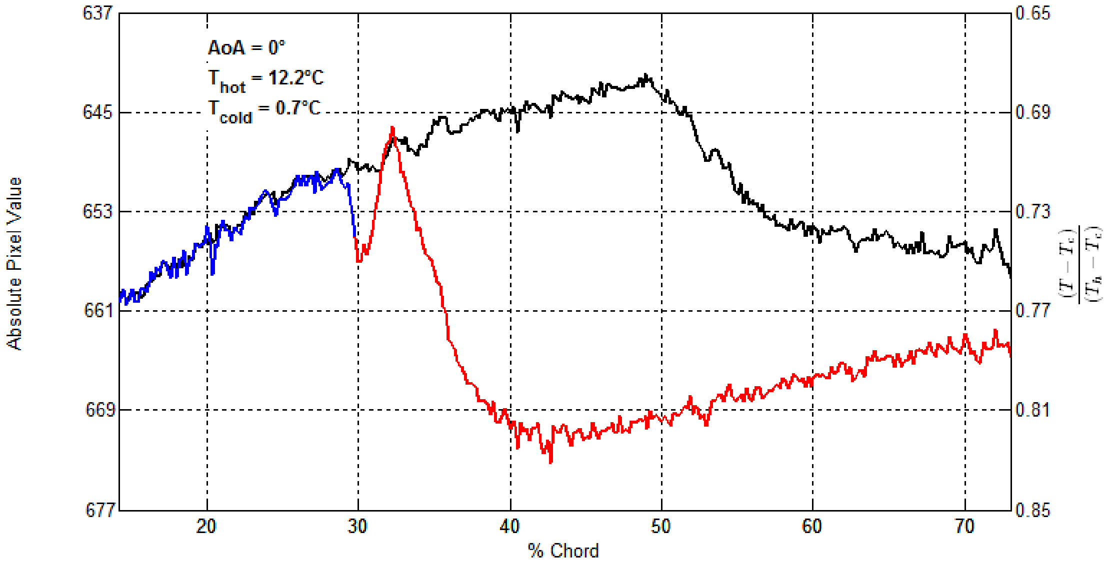

Figure 125 Surface temperature profile of painted RP with ice water in Figure **124**

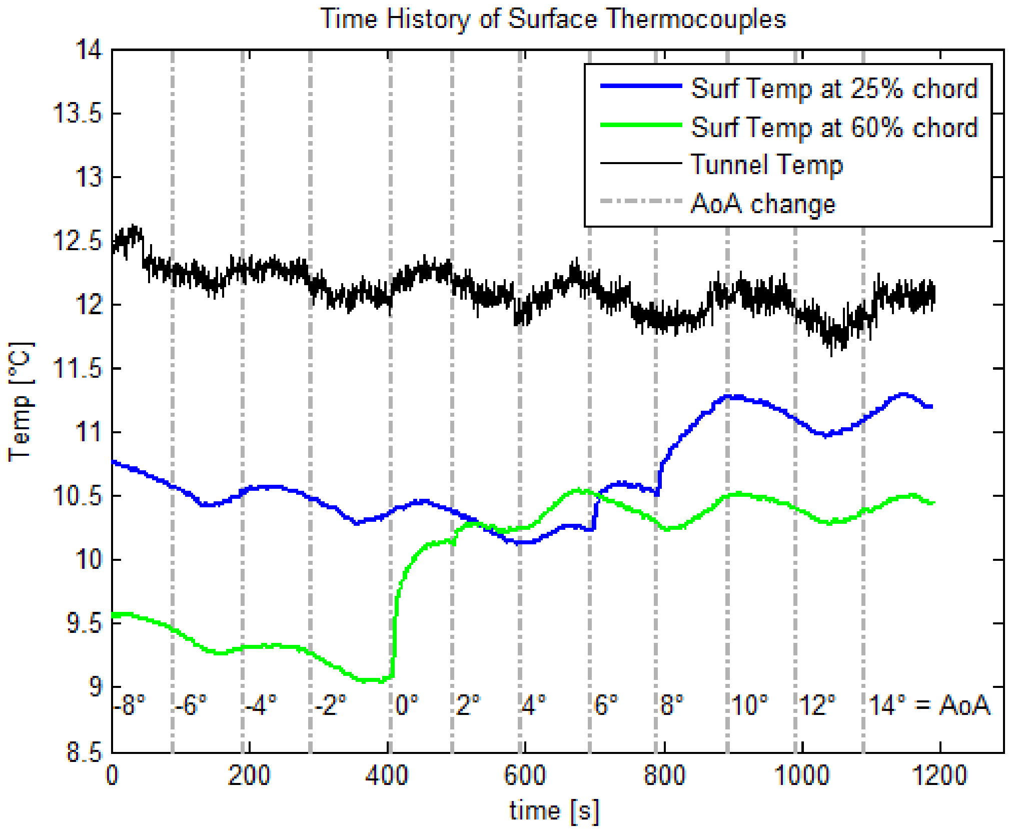

Figure 126 Time history of tunnel and surface temperatures for entire run corresponding to Figure **124**

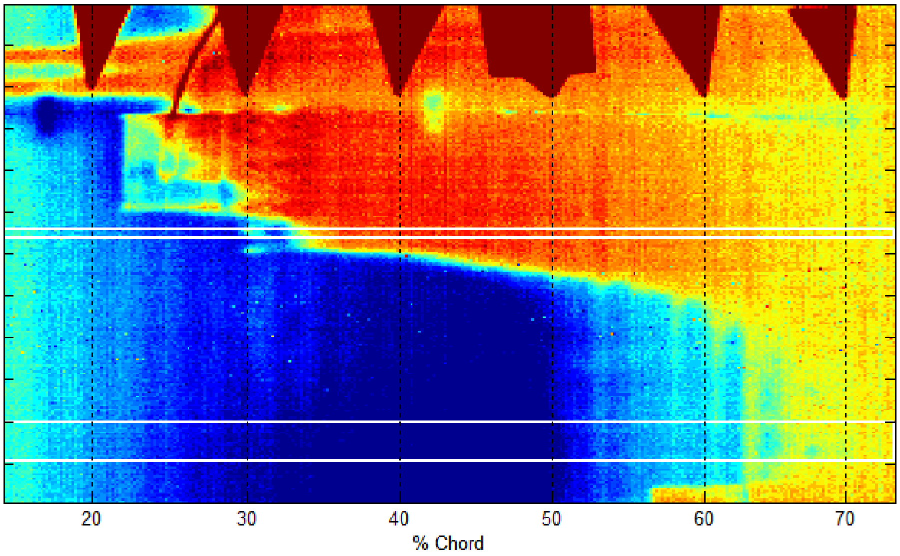

Figure 127 IR image of painted RP plastic using ice water circulation, AoA = 0° and $Re_c = 6.6\times10^5$

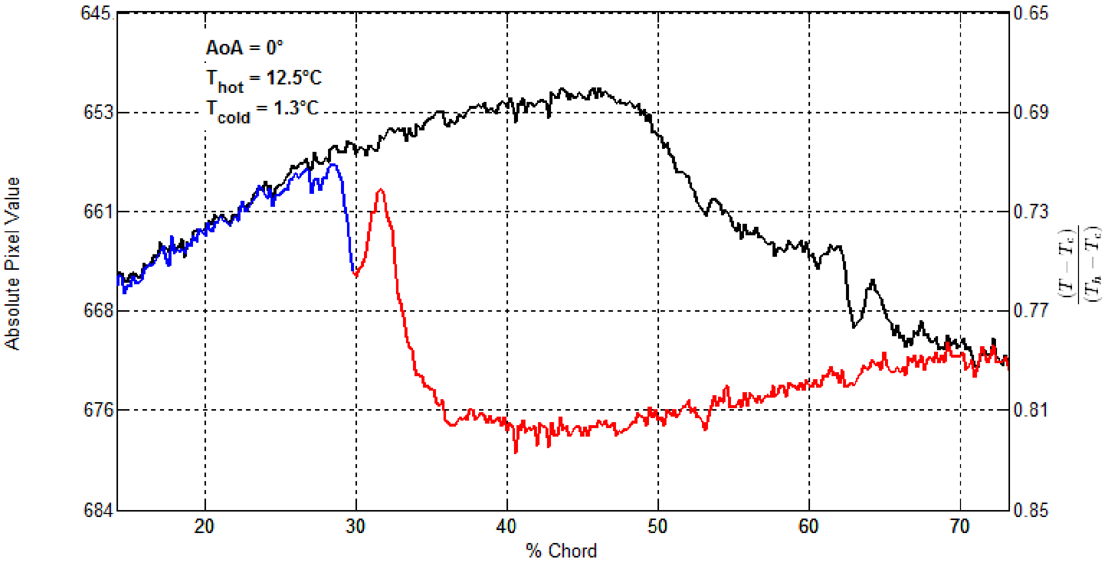

Figure 128 Surface temperature profile of Figure 127

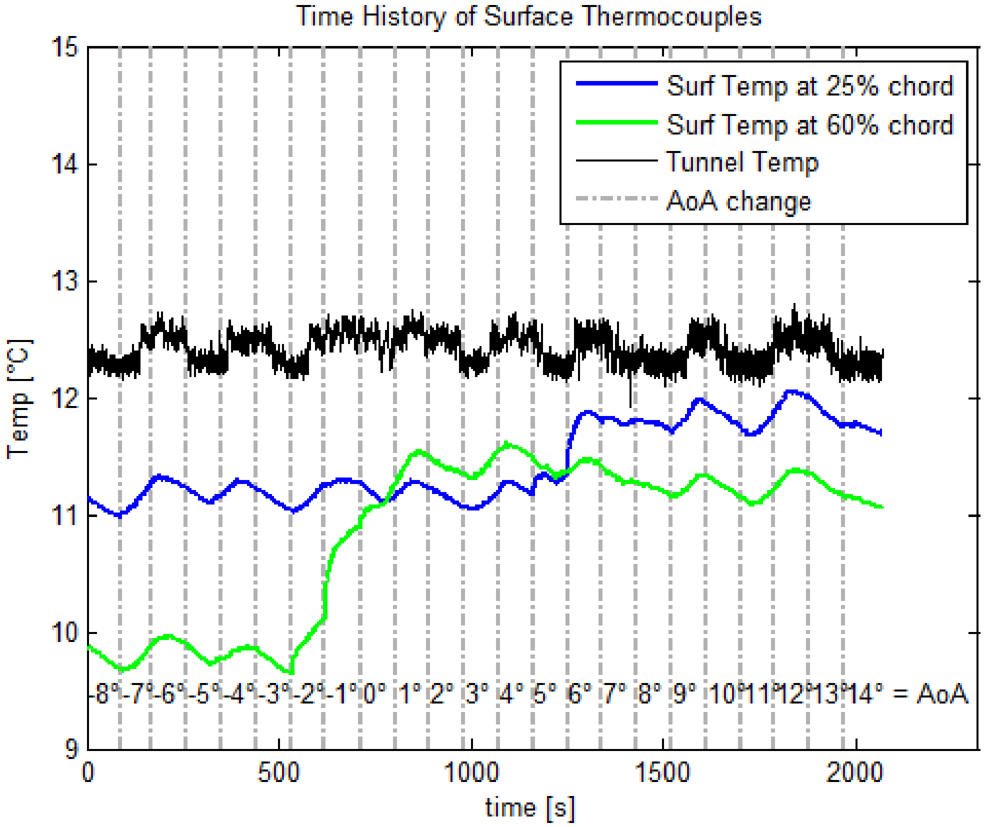

Figure 129 Time history of tunnel and surface temperatures for entire run corresponding to Figure 127

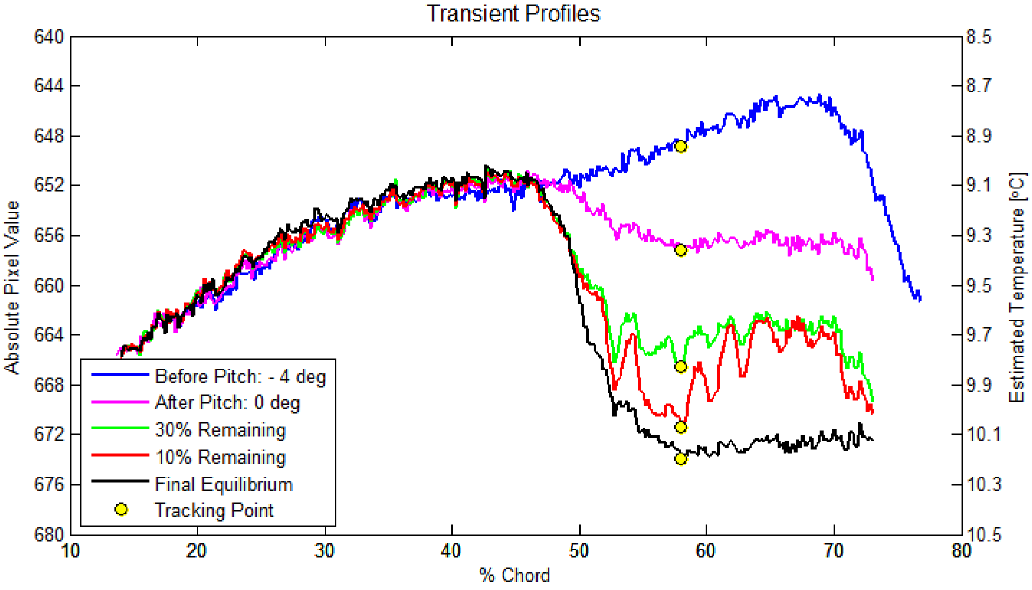

Figure 130 Temperature profiles throughout transient response as the model is pitched from AoA = -4° to 0°; configuration corresponds to Figure 127

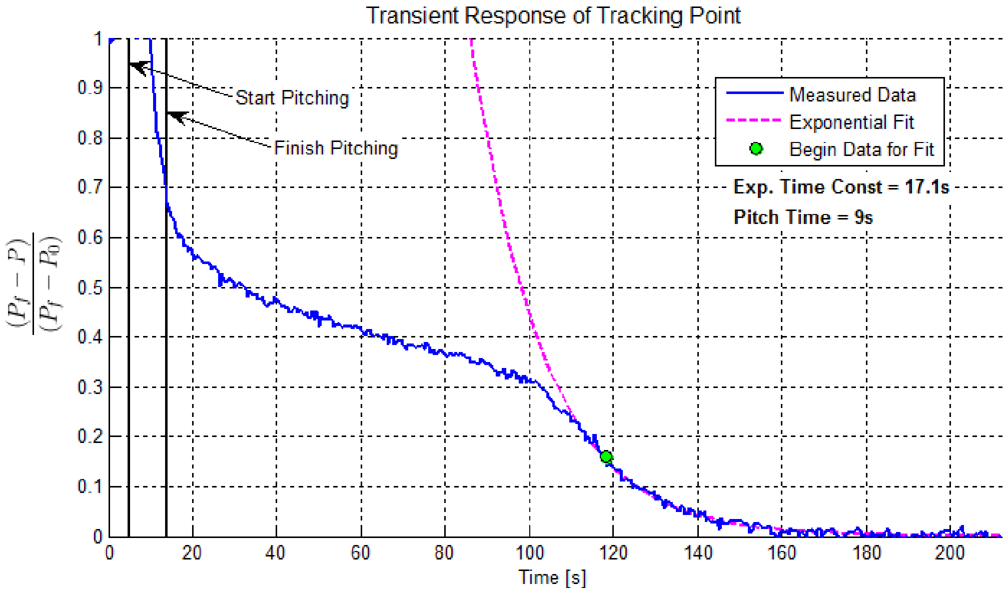

Figure 131 Response of tracking point shown in Figure 130 as a yellow circle Data is fit to an exponential decay function

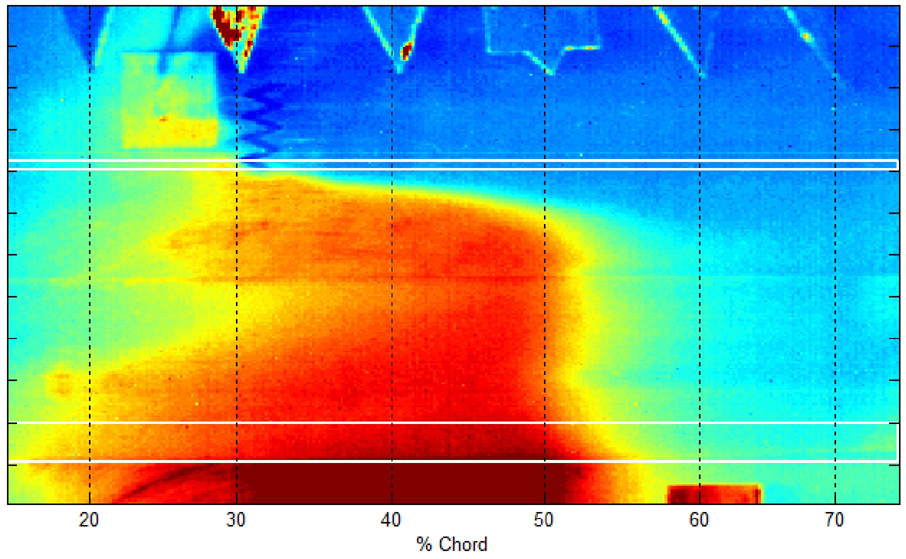

Figure 132 IR image of painted RP plastic with a layer of Bondo that is painted except for a strip across the middle. It is tested using the heat lamp.
AoA = 0° and $Re_c = 6.6\times10^5$

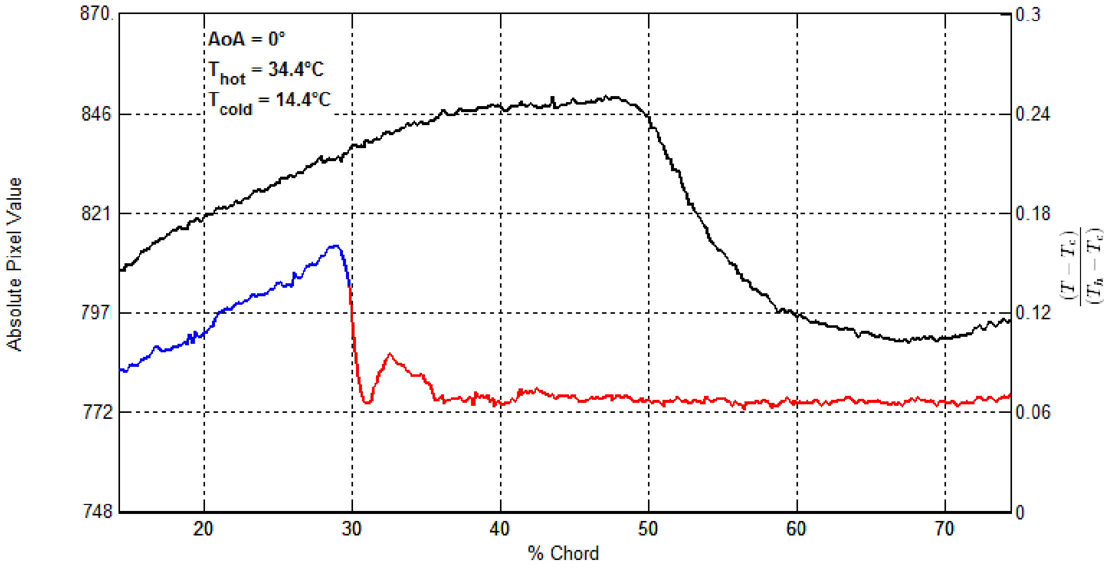

Figure 133 Surface temperature profile of Figure 132

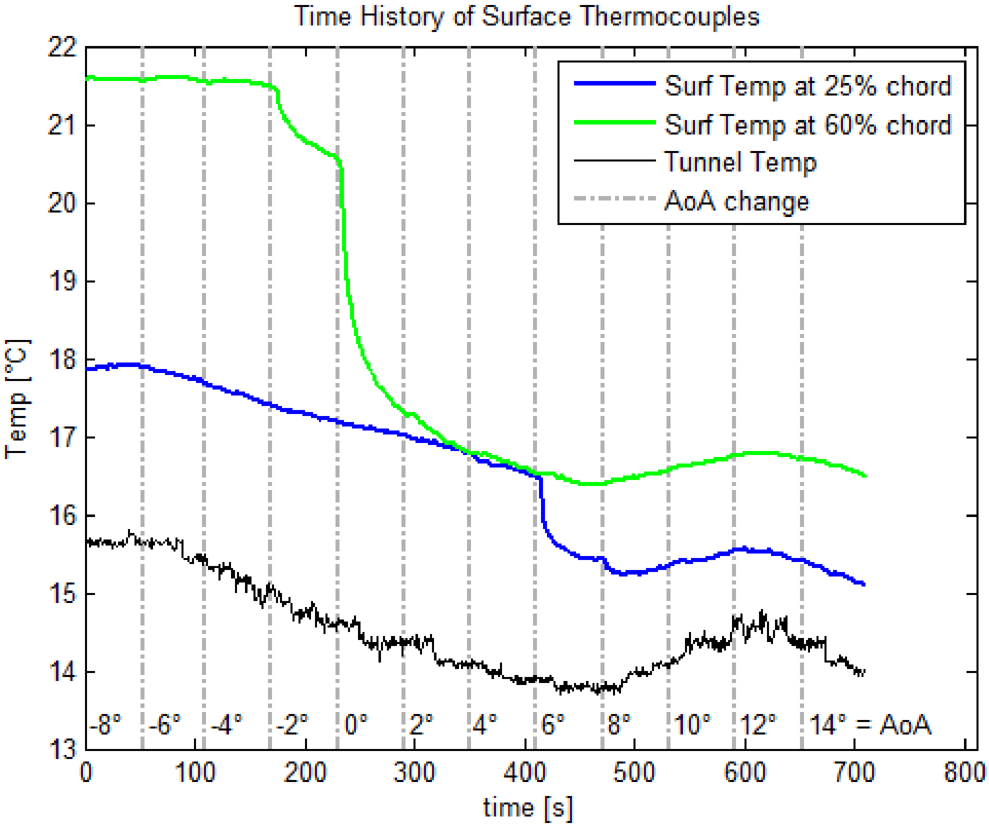

Figure 134 Time history of tunnel and surface temperatures for entire run corresponding to Figure 132

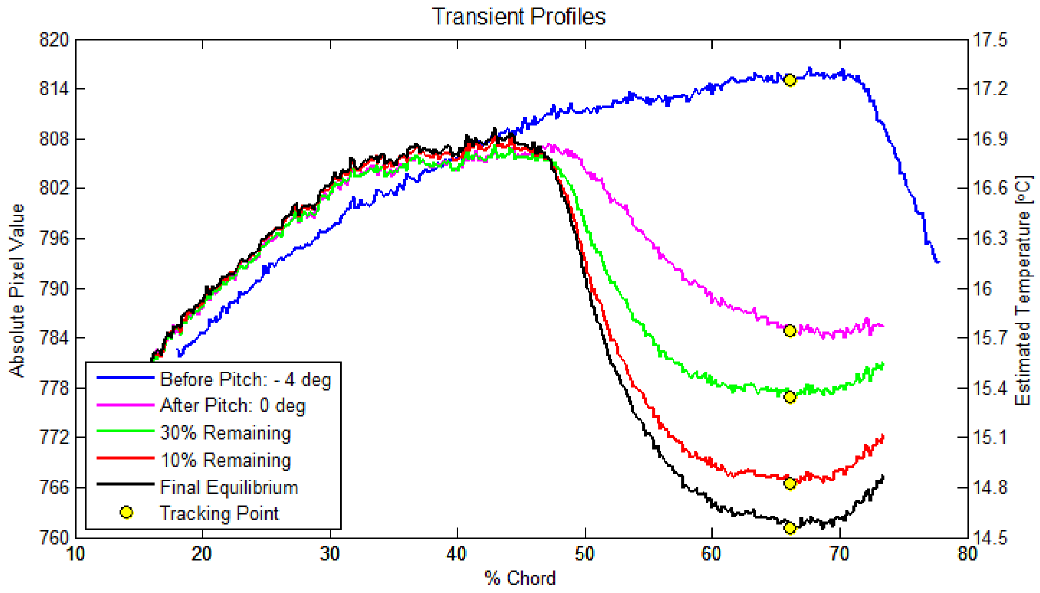

Figure 135 Temperature profiles throughout transient response as the model is pitched from AoA = -4° to 0°; configuration corresponds to Figure 132

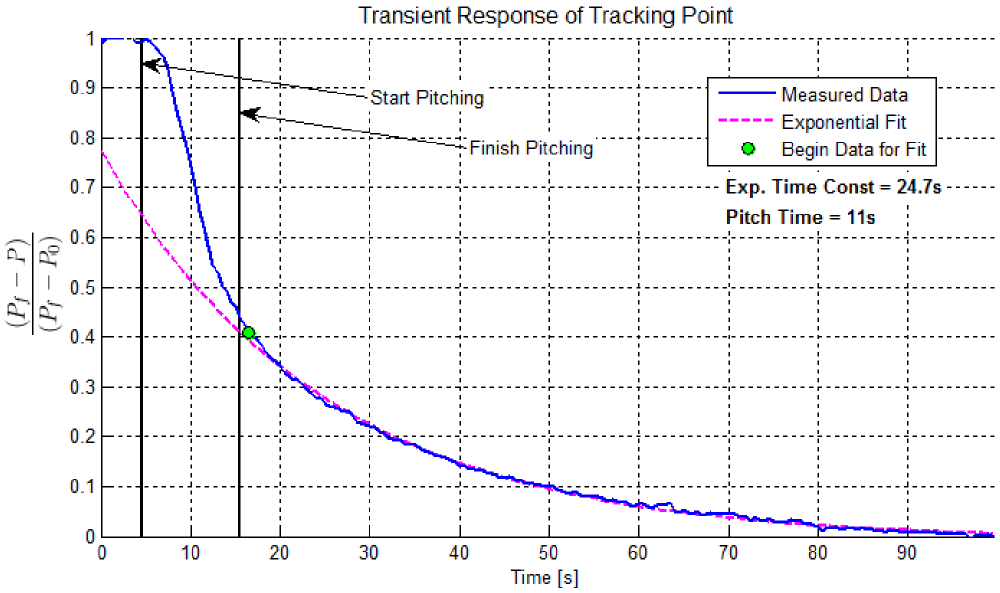

Figure 136 Response of tracking point shown in Figure 135 as a yellow circle Data is fit to an exponential decay function

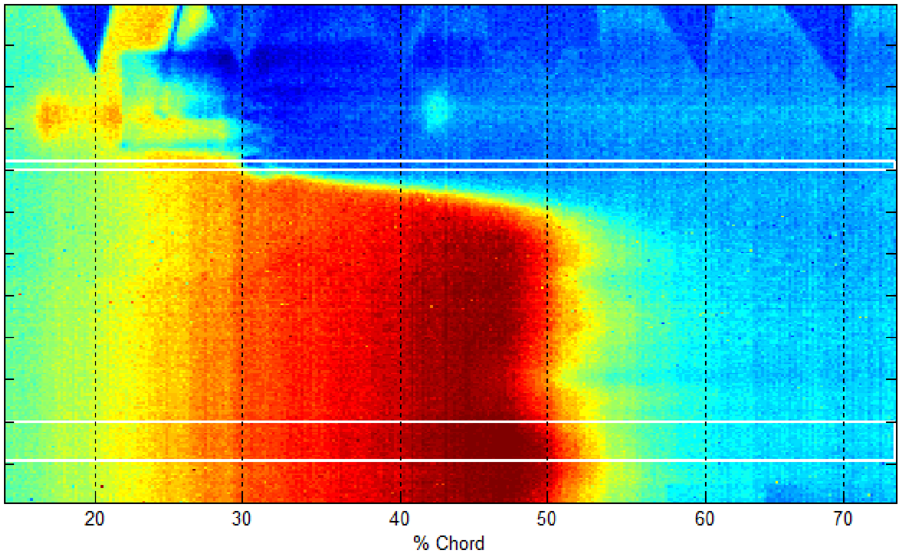

Figure 137 IR image of painted RP plastic with a layer of Bondo that is painted except for a strip across the middle. It is tested using tap water circulation.
AoA = 0° and $Re_c = 6.6 \times 10^5$

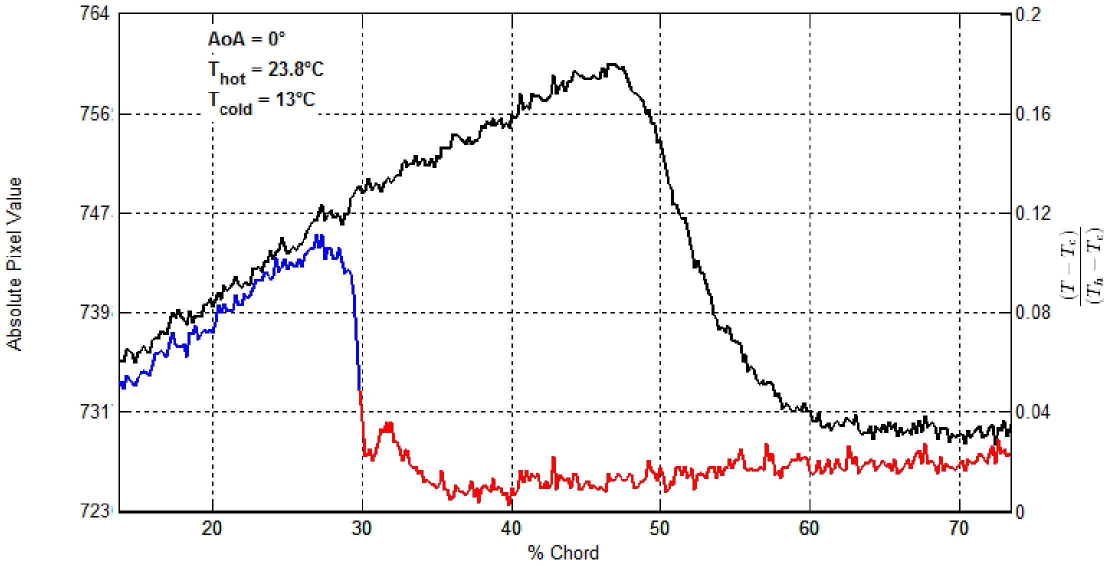

Figure 138 Surface temperature profile of Figure 137

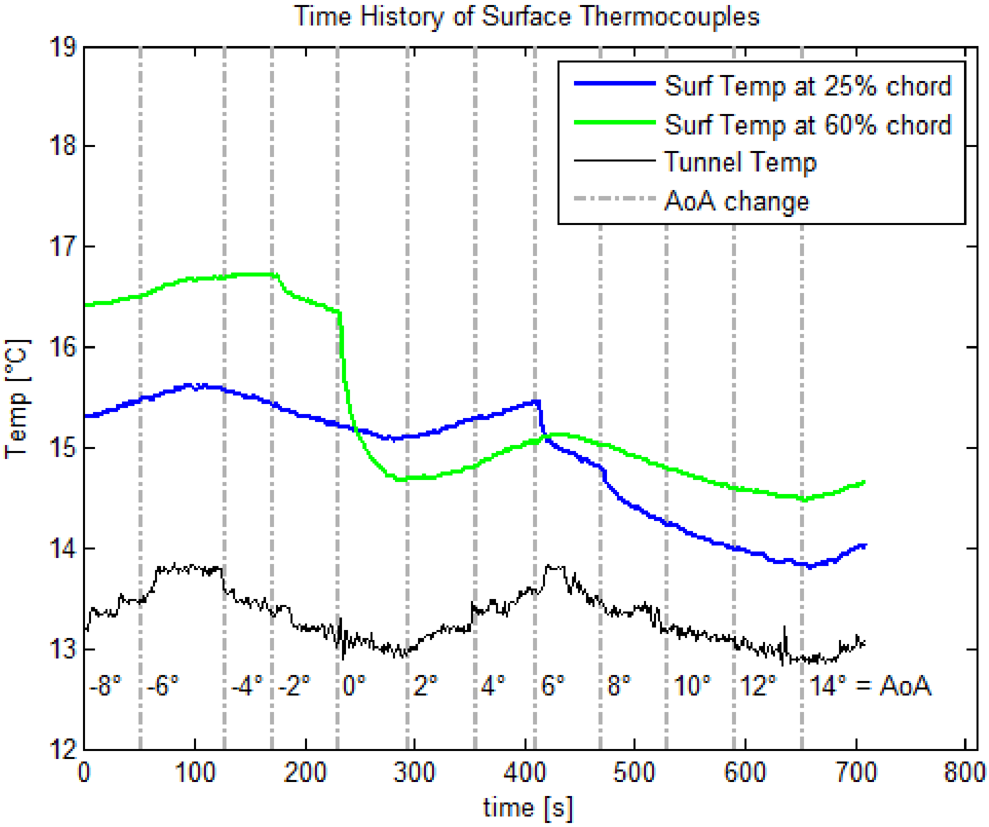

Figure 139 Time history of tunnel and surface temperatures for entire run corresponding to Figure 137

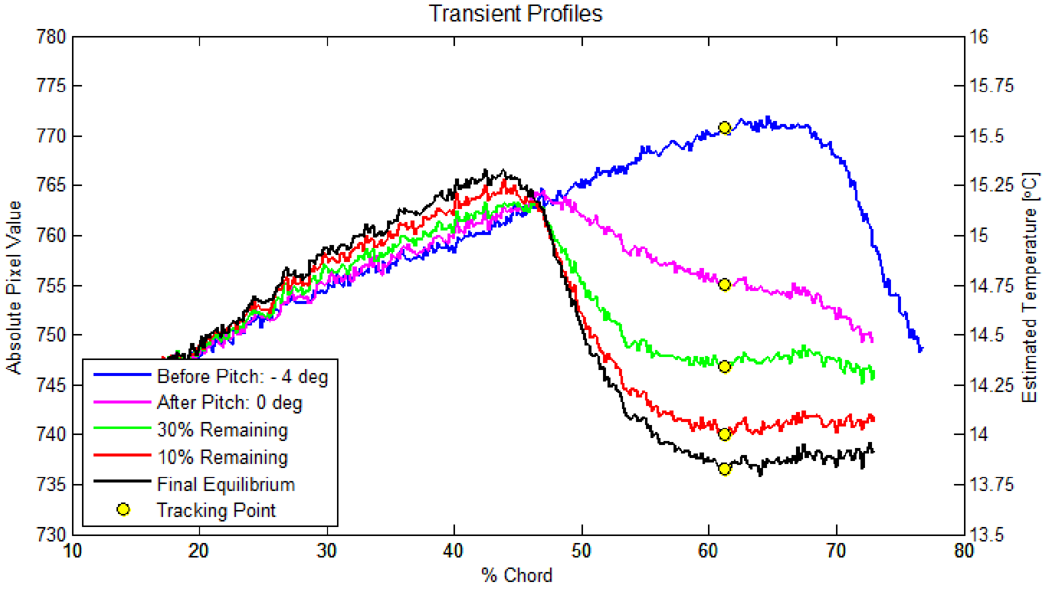

Figure 140 Temperature profiles throughout transient response as the model is pitched from AoA = -4° to 0°; configuration corresponds to Figure 137

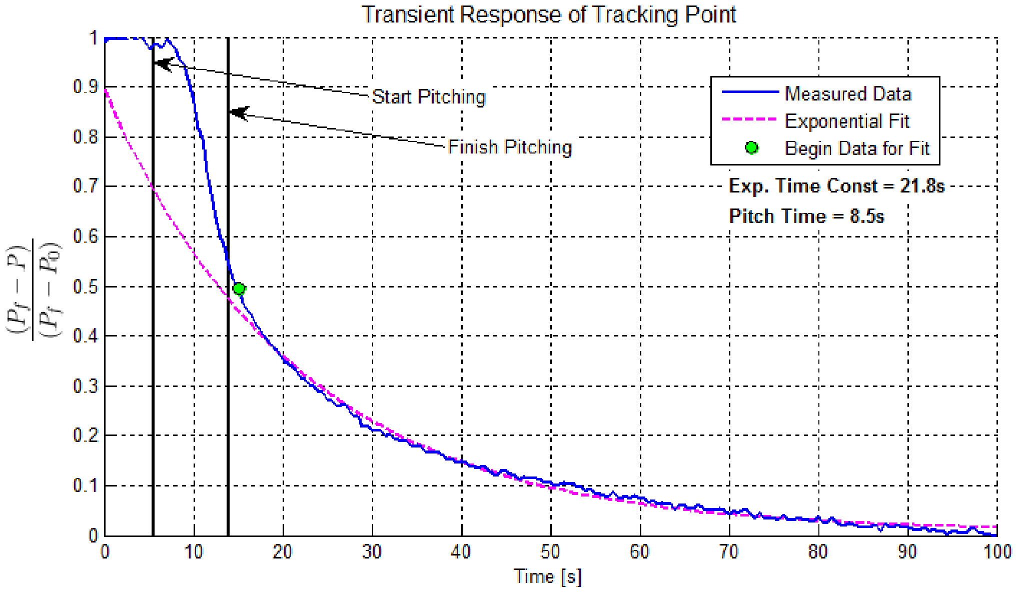

Figure 141 Response of tracking point shown in Figure 140 as a yellow circle Data is fit to an exponential decay function

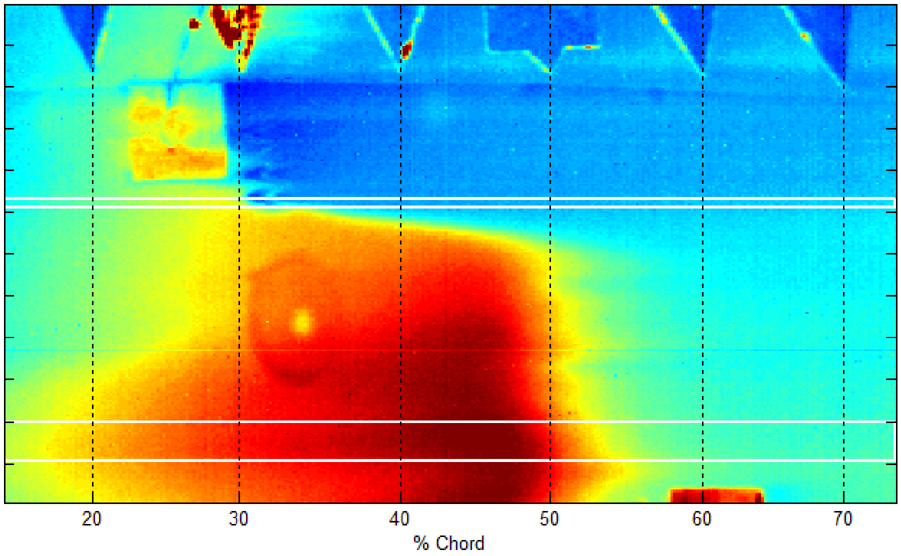

Figure 142 IR image of the painted RP plastic wrapped with Monokote over the painted and unpainted regions of Bondo. It is tested using the heat lamp.
AoA = 0° and $Re_c = 6.6\times10^5$

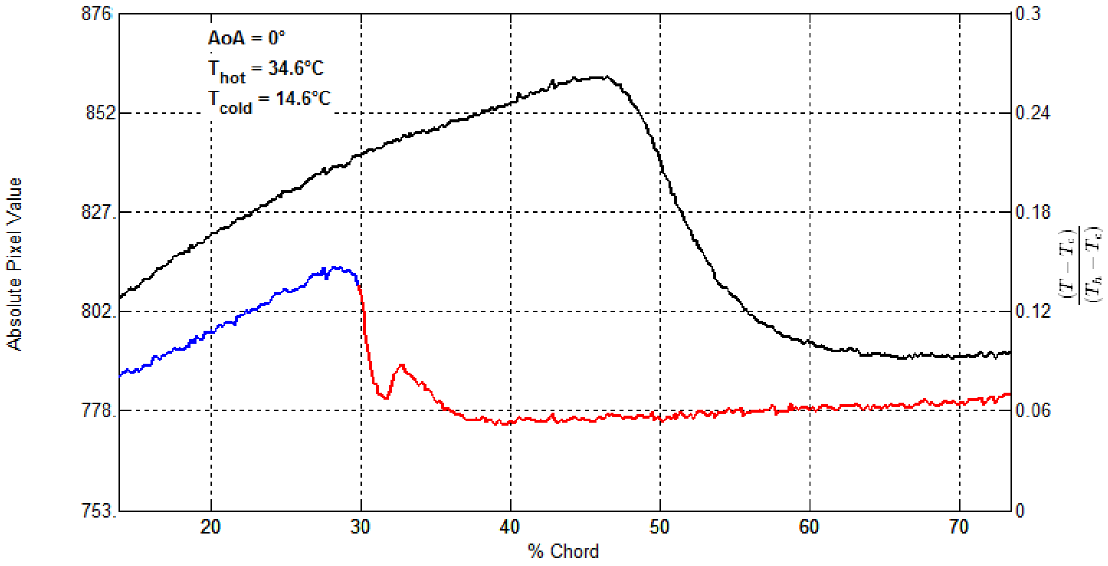

Figure 143 Surface temperature profile of Figure 142

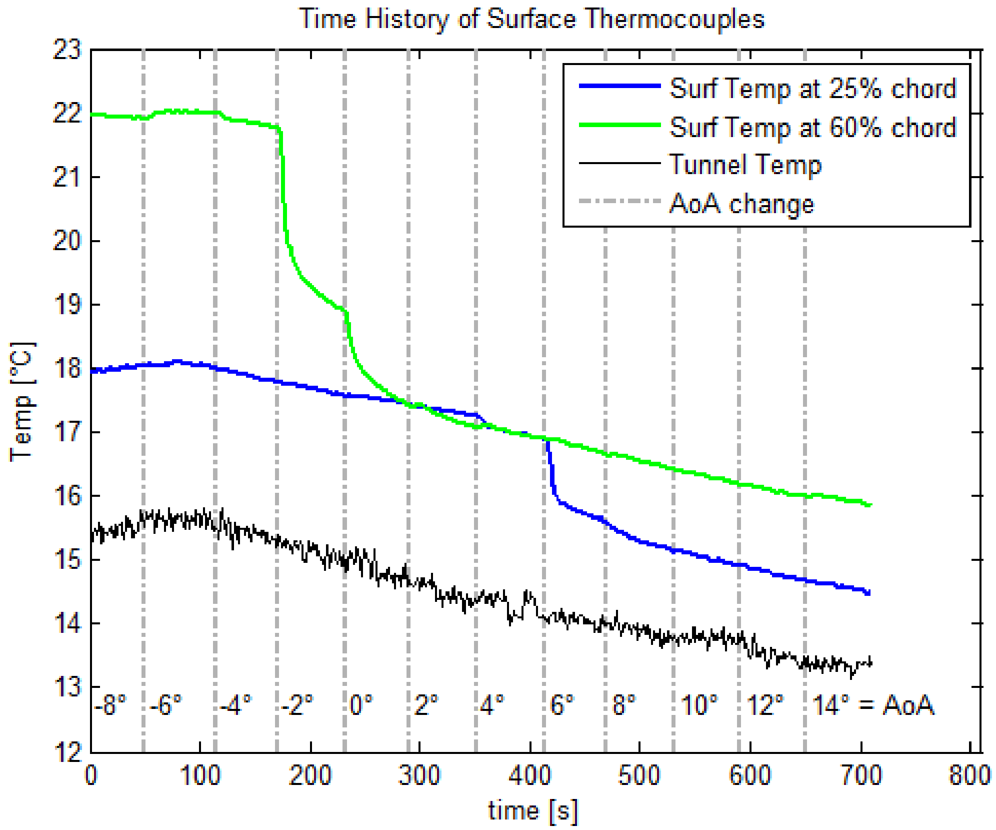

Figure 144 Time history of tunnel and surface temperatures for entire run corresponding to Figure 142

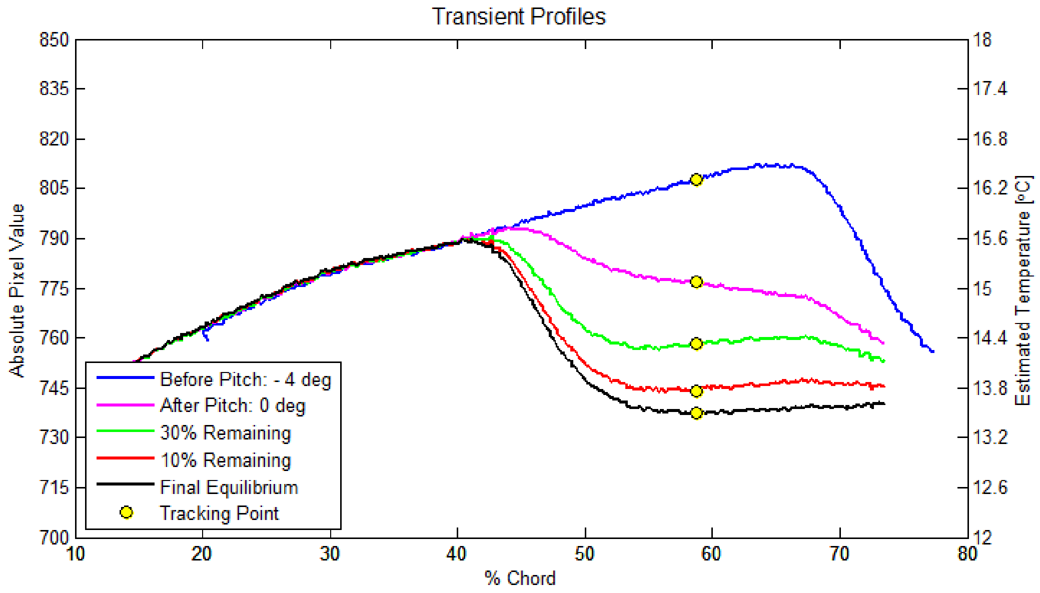

Figure 145 Temperature profiles throughout transient response as the model is pitched from AoA = -4° to 0°; configuration corresponds to Figure 142

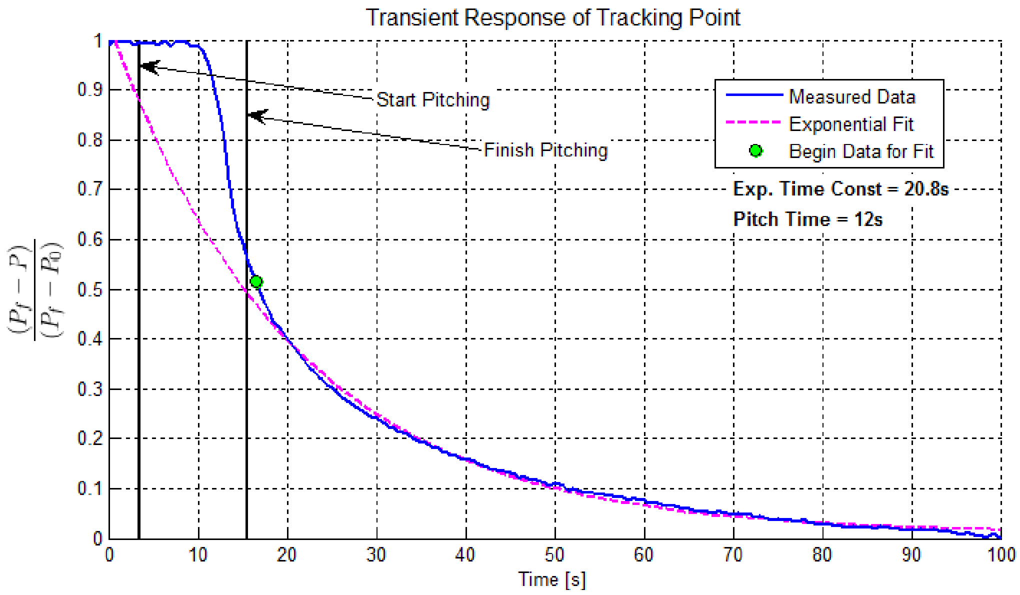

Figure 146 Response of tracking point shown in Figure 145 as a yellow circle Data is fit to an exponential decay function

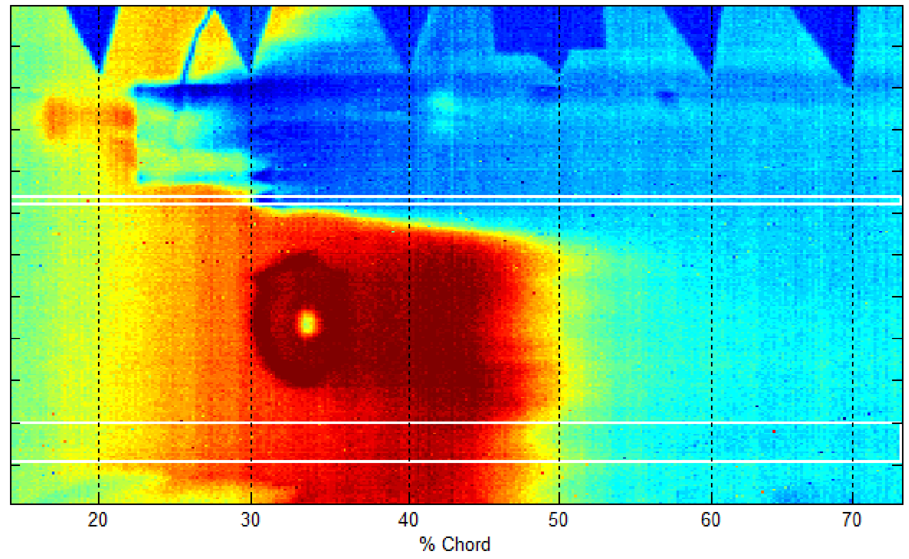

Figure 147 IR image of the painted RP plastic wrapped with Monokote over the painted and unpainted regions of Bondo. It is tested using tap water circulation.
AoA = 0° and $Re_c = 6.6\times10^5$

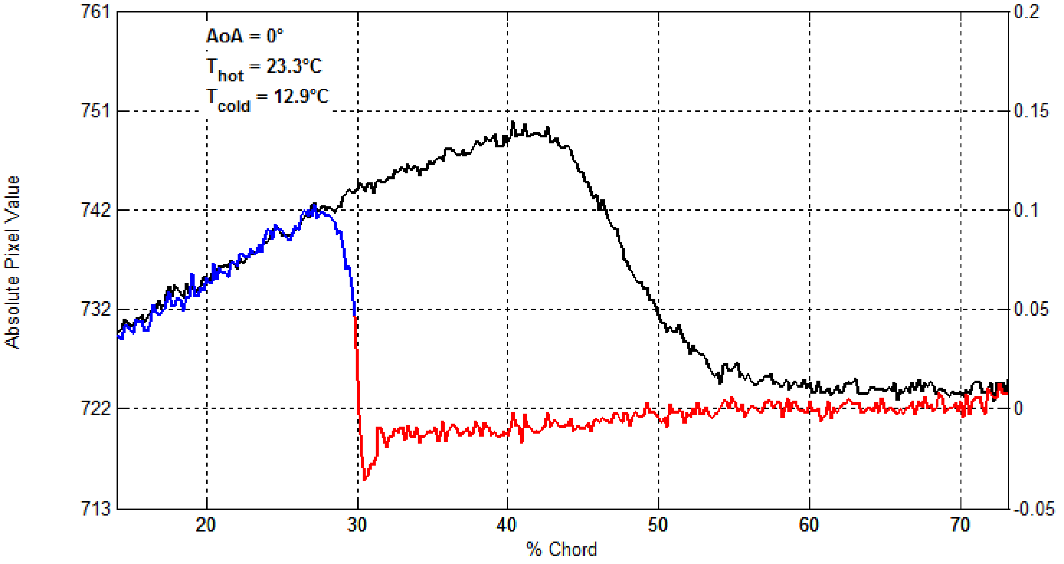

Figure 148 Surface temperature profile of Figure 147

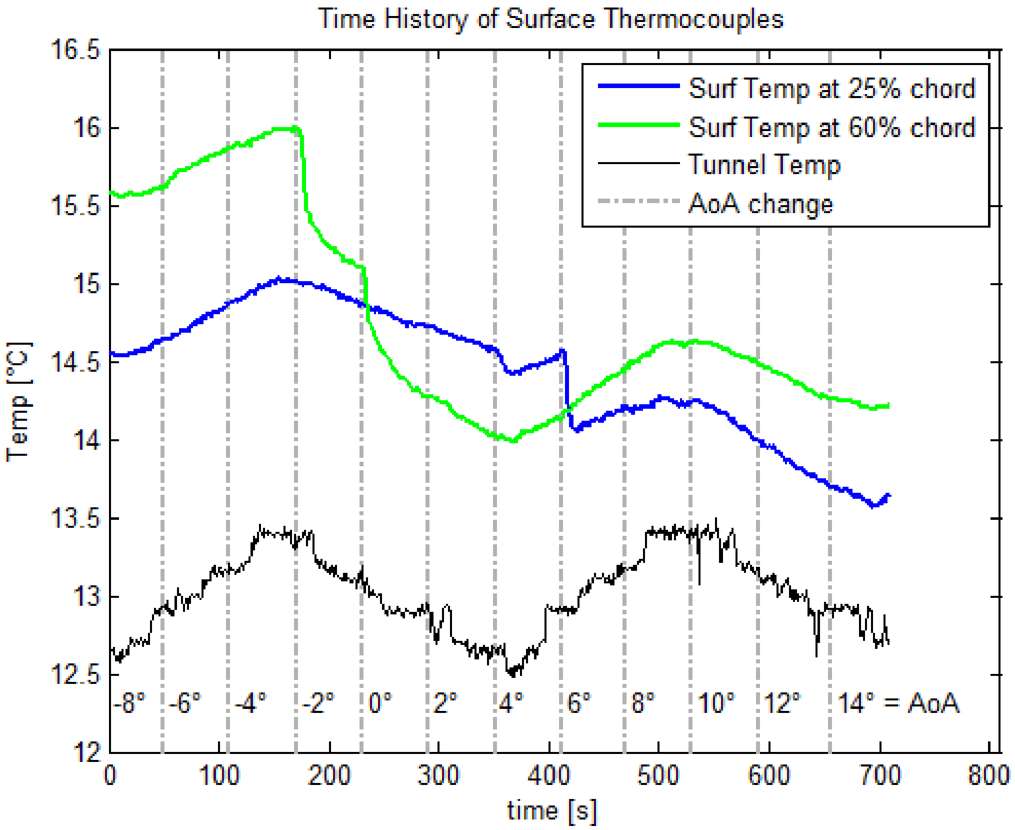

Figure 149 Time history of tunnel and surface temperatures for entire run corresponding to Figure 147

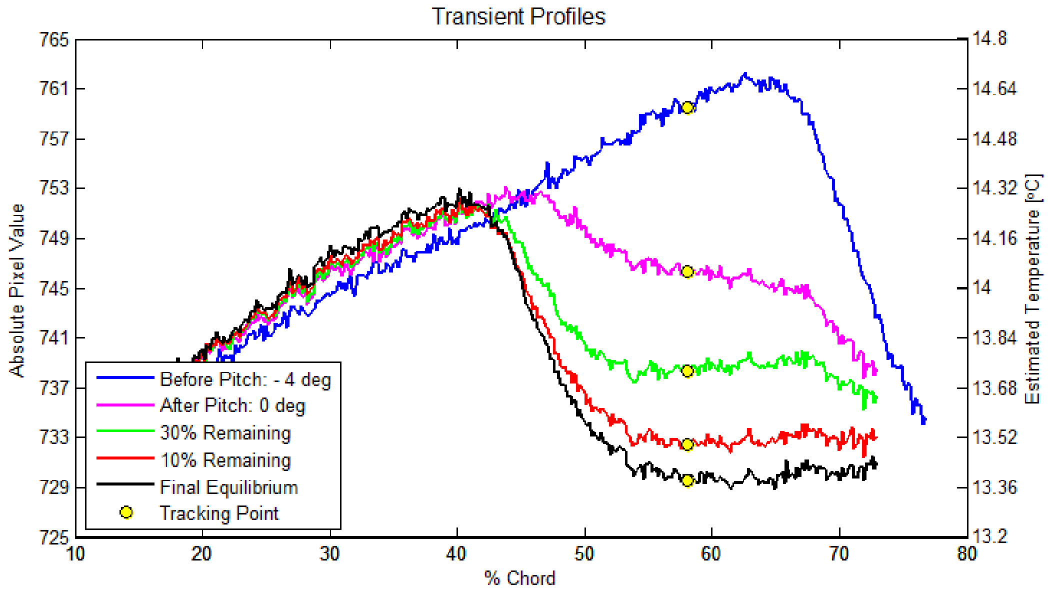

Figure 150 Temperature profiles throughout transient response as the model is pitched from AoA = -4° to 0°; configuration corresponds to Figure 147

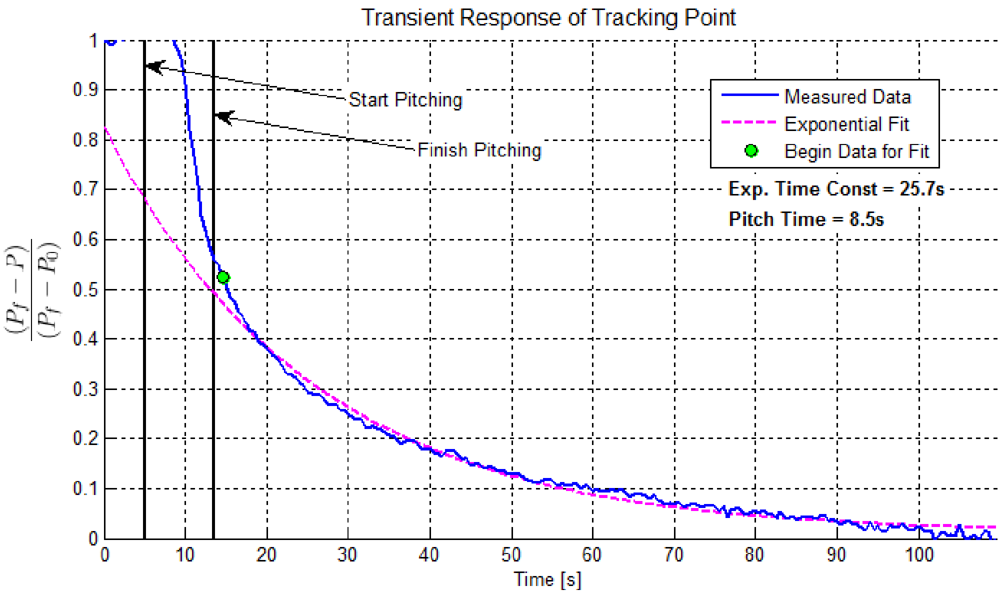

Figure 151 Response of tracking point shown in Figure 150 as a yellow circle Data is fit to an exponential decay function

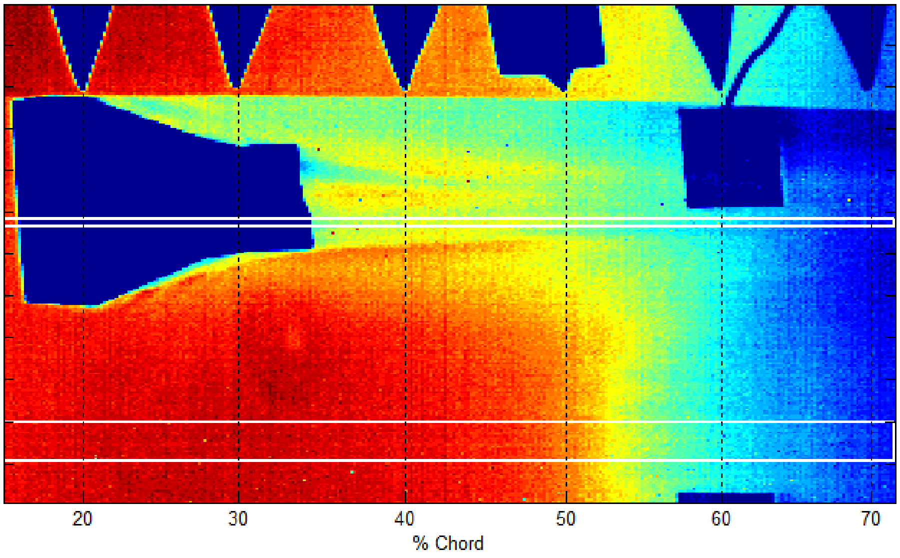

Figure 152 Aluminum with painted adhesive wrap and large VG
Tested using tap water circulation
AoA = 0° and $Re_c = 6.6 \times 10^5$

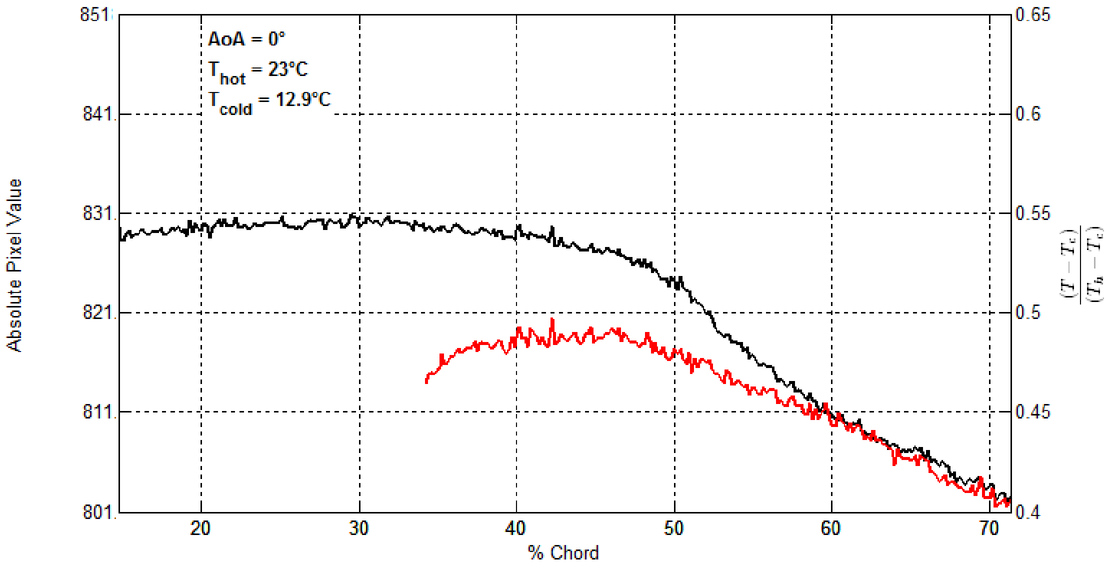

Figure 153 Surface temperature profile of Figure 152

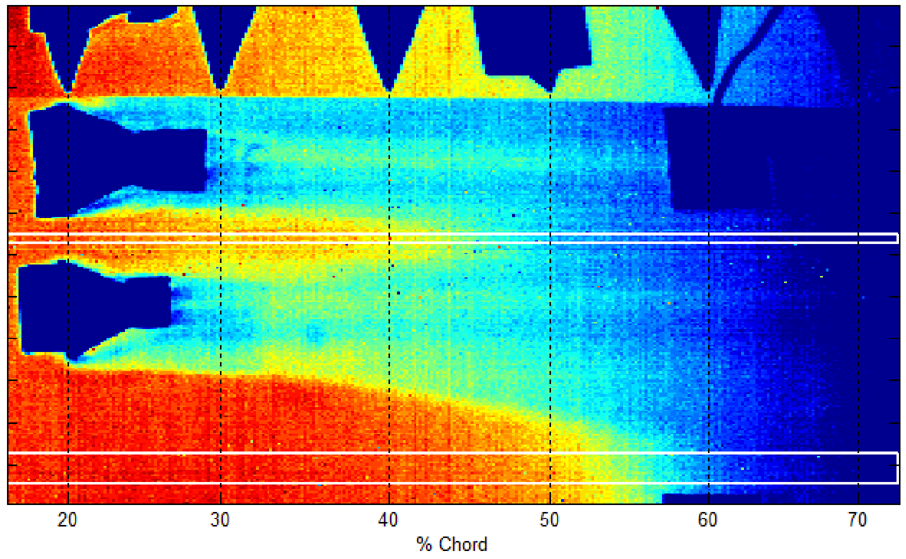

Figure 154 Aluminum with painted adhesive wrap and small VGs
Tested using tap water circulation
AoA = 0° and $Re_c = 6.6\times10^5$

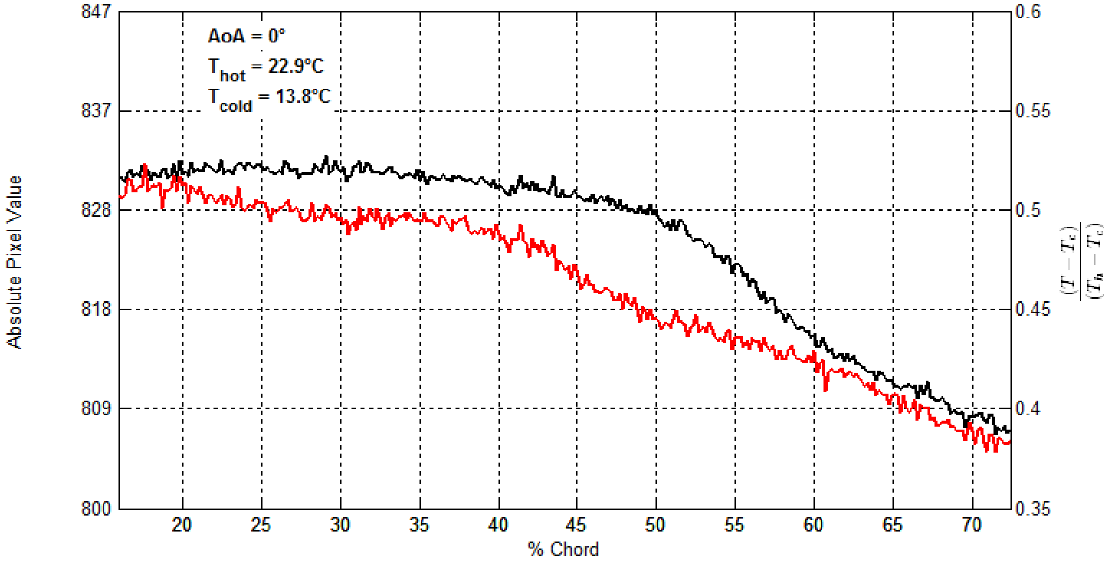

Figure 155 Surface temperature profile of Figure 154

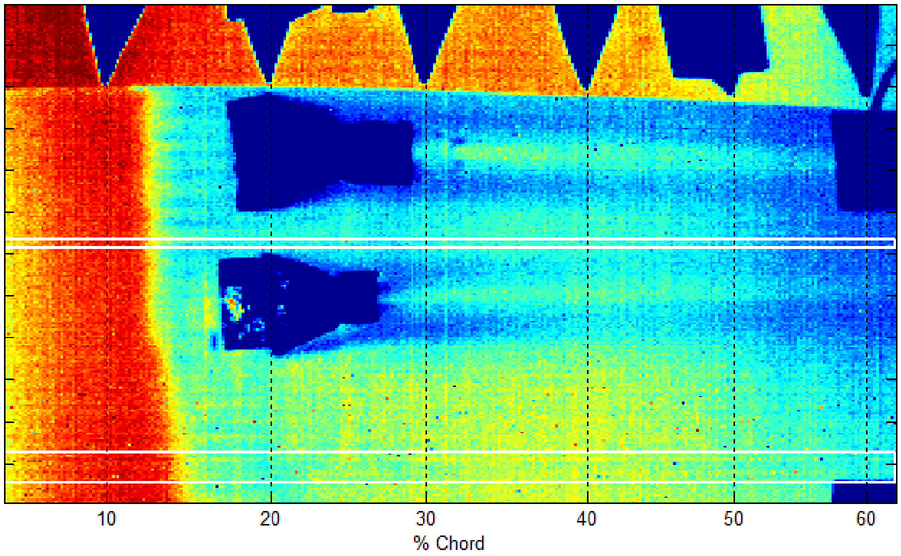

Figure 156 Aluminum with painted adhesive wrap and small VGs
Tested using tap water circulation
AoA = 12° and $Re_c = 6.6\times10^5$

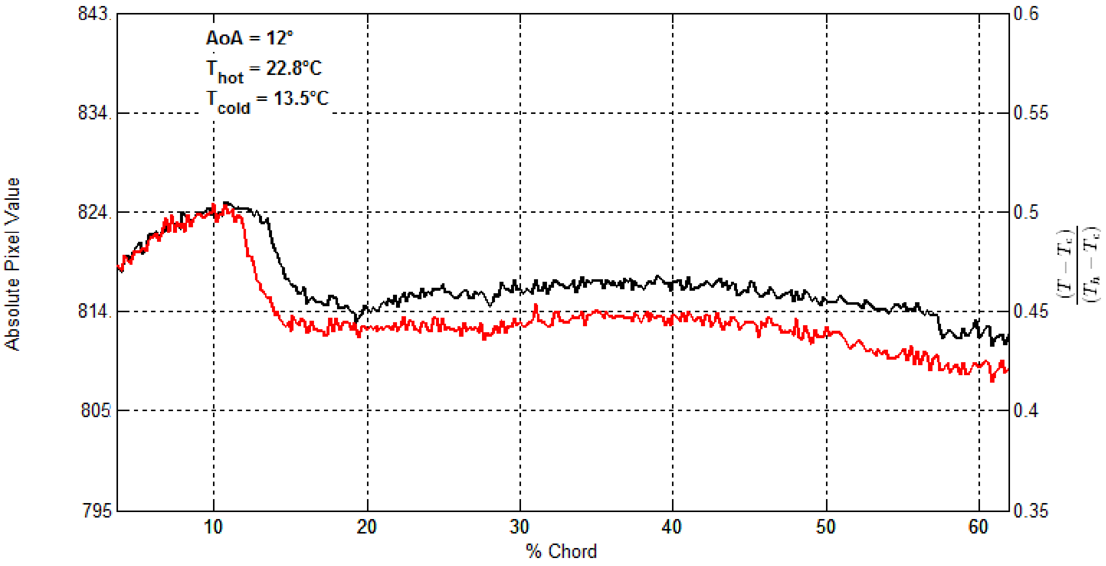

Figure 157 Surface temperature profile of Figure 156

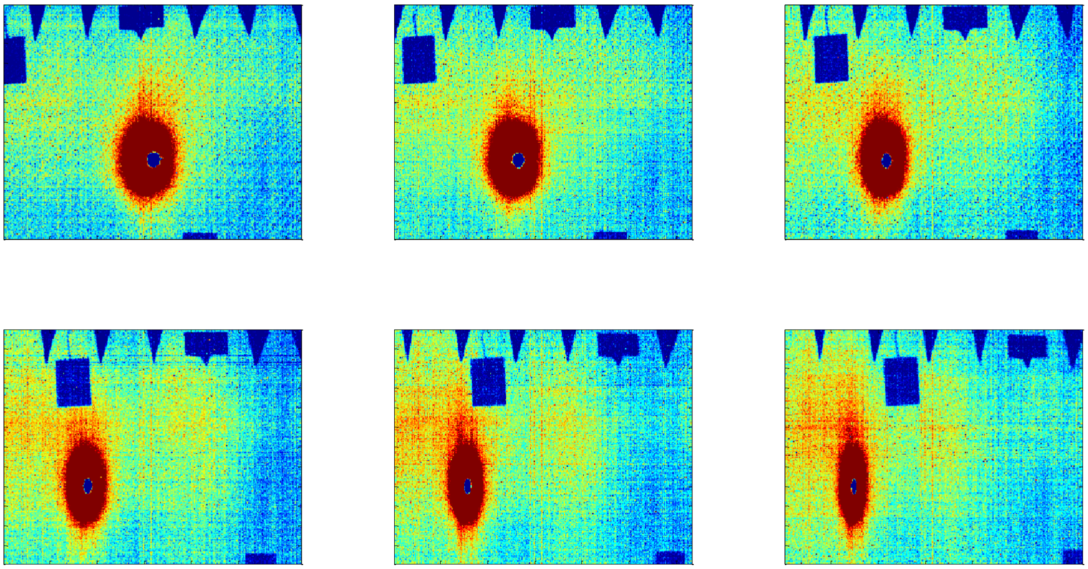

Figure 158 Sequence of IR images for polished aluminum model during AoA sweep with no airflow and no model heating. Angles of the images are, from left to right on top row: -8°, -4°, and 0°. From left to right on bottom row: 4°, 8°, and 12°

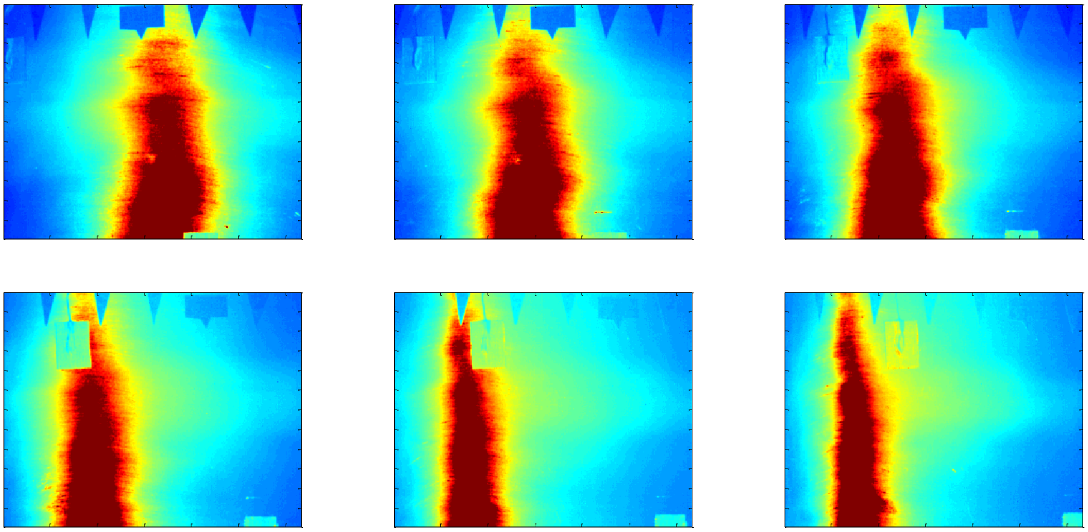

Figure 159 Sequence of IR images for polished aluminum model during AoA sweep with the heat lamp and no airflow. Angles of the images are, from left to right on top row: -8°, -4°, and 0°. From left to right on bottom row: 4°, 8°, and 12°

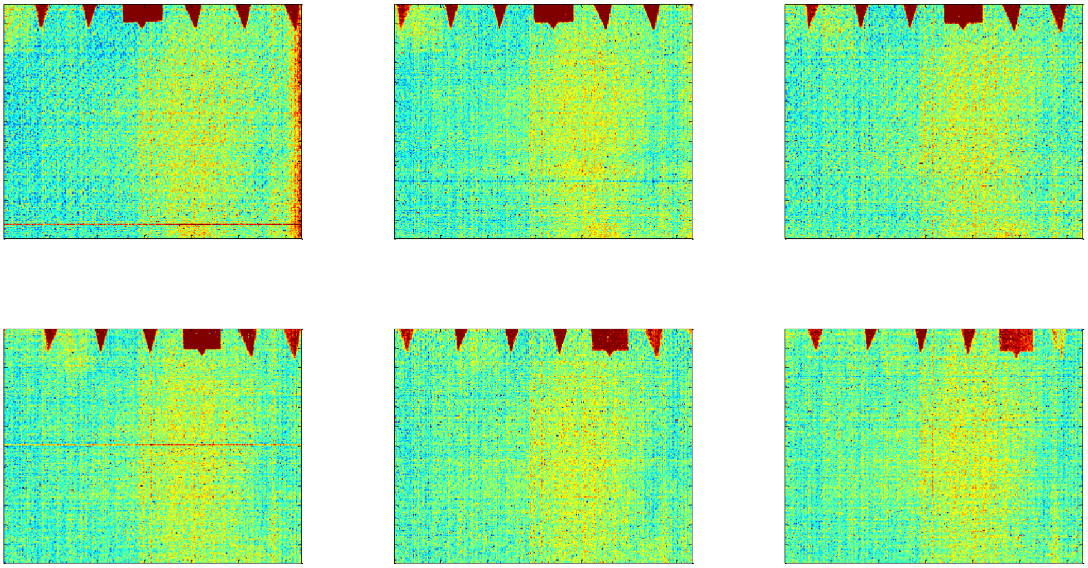

Figure 160 Sequence of IR images for as-built RP model during AoA sweep with no airflow and no model heating. Angles of the images are, from left to right on top row: -8°, -4°, and 0°. From left to right on bottom row: 4°, 8°, and 12°

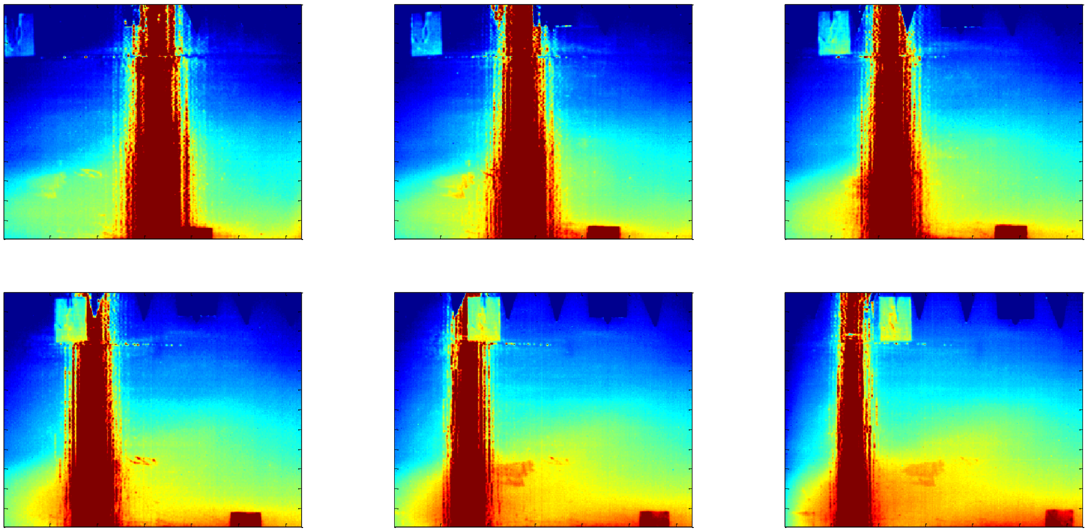

Figure 161 Sequence of IR images for as-built model during AoA sweep with the heat lamp and no airflow. Angles of the images are, from left to right on top row: -8°, -4°, and 0°. From left to right on bottom row: 4°, 8°, and 12°